Effect of Inlet Bubble Size on Flow Regime Development in Air-water Upward Two-phase Flow

A Thesis

Submitted to the Faculty

Of

The Ohio State University

By

Benjamin Doup

In Partial Fulfillment of the

Requirements for the Completion

of

Graduation with Distinction

November 2010

ABSTRACT

It is essential to determine the flow regime for gas-liquid two-phase flows since many constitutive models are flow regime dependent. In this study, an instrumentation system together with an air-water two-phase flow test facility was tested to determine if such a system can detect different flow regimes mechanistically. This instrumentation system will be used in the future to determine the effect of the inlet bubble size on downstream flow regime and interfacial structure development. Some modifications were made to the test facility including installing a larger air-water separator and changing the inlet water lines to allow for independent control and measurement of the flow rate of the auxiliary water line. The instruments that were installed are; 1. a high-speed video camera that is placed at the inlet of the test section to record a video representation of the inlet flow conditions; 2. a pressure transducer installed to measure the inlet pressure and a differential pressure transducer to measure the pressure drop across the test section, which can be used to estimate the void fraction when it is small; and 3. impedance void meters and four-sensor conductivity probe supports were built and installed at the inlet, middle, and outlet of the test section. The impedance void meters were used to measure the area averaged (or small volume-averaged) void fraction and the normalized impedance signals from these meters were investigated to study if different flow regimes could be observed. The four-sensor conductivity probe will be used to determine two-phase flow local parameters for both small (group I) and large (group II) bubbles. These parameters include bubble velocity, time-averaged local void fraction, and interfacial area concentration. The local void fraction and interfacial area concentration will be used to calculate the Sauter mean bubble diameter. The data from

these instruments are acquired using a National Instruments PCIe-6353 device. Test were performed and analyzed, and it was determined that the installed instrumentation system, is capable of identifying flow regime transitions.

ACKNOWLEDGMENTS

I would like to thank all the people who have helped and supported me during the course of this project. I would like to thank my advisor, Professor Xiaodong Sun for his help and guidance for the project. I also thank Professor Richard Christensen for serving on my thesis exam committee. I would also like to thank the graduate students in the Thermal Hydraulics Laboratory, particularly Sai Mylavarapu, for their help. I would also like to thank the machinists in the Physics Department machine shop for all of their help.

Table of Contents

LIST OF FIGURES

LIST OF TABLES

NOMENCLATURE

A	Total cross sectional area of the test section
A_g	Cross sectional area occupied by the air
a_i	Interfacial area concentration
C_D	Drag coefficient
d_b	Diameter of inlet bubbles
DP_r	Differential pressure reading of the differential pressure transducer
$D_{d\max}$	Maximum distorted bubble limit
D_{ds}	Maximum spherical bubble limit
D_{smd}	Sauter mean diameter
g	Gravitational constant
G	Impedance
$G*$	Normalized impedance
G_g	Impedance signal when the test section is filled with gas/air
G_f	Impedance signal when the test section is filled with liquid/water
h	Height of the test section
I	Electrical current
j	Superficial velocity
∂j	Uncertainty in the measured value of the superficial velocity
N_{μ_f}	Liquid viscosity number
L/D	Axial position divided by the diameter of the test section

P	Pressure
P_{back}	Pressure between the rotameters and the inlet to the test section
δP_{back}	Uncertainty in the measured value of the pressure between the rotameters and the inlet to the test section
ΔP_m	Actual differential pressure
$\partial \Delta P_m$	Uncertainty in the measured value of the actual differential pressure
Q	Flow rate
∂Q	Uncertainty in the measured value of flow rate
r/R	Normalized radius
R	Electrical resistance
r_o	Average pore size of the sparger
T	Temperature
V	Voltage
v	Velocity
Greek symbols	
α	Void fraction
μ_f	Viscosity of the liquid/water
ρ_f	Density of liquid/water
$\Delta\rho$	Difference in density between liquid/water and gas/air
σ	Surface tension
Units of measurement	

“	Inches
‘	Feet
^{o}C	Degrees Celsius
atm	Atmospheric pressure
ft^3	Cubic feet
gpm	Gallons per minute
hr	Hour
kHz	Kilohertz
m	Meter
mA	Milliamps
mm	Millimeter
MPa	Mega pascals
MS	Mega sample
psi	Pounds per square inch
psig	Gauge pounds per square inch
Subscripts	
1	Conditions at the inlet of the test section
2	Conditions at the outlet of the test section
actual	Conditions between the rotameters and inlet to the test section
f	Fluid/water
g	Gas/air
standard	Standard conditions (14.7 psia and 20 ^{o}C)

Chapter 1: Introduction

1.1 Background

Gas-liquid two-phase flow is a very important phenomenon that appears in many industrial processes, including nuclear reactors, chemical reactors, boilers, condensers, etc. In general, two-phase flow can be solid and gas flow or solid and liquid flow, but typically two-phase flow in nuclear power applications is referred to as liquid and gas flow. The reason that makes two phase flow hard to model is that not only is the flow normally turbulent but the flow field is not continuous. For instance, when single-phase flow occurs, the physical properties such as the heat and mass transfer coefficients and density are continuous. When two-phase flow occurs, these same properties that were continuous in single phase flow are now discontinuous due to the differences between gas and liquid properties. Another difficulty to model two phase flow arises when the flow rate of air increases relative to the liquid flow rate. The gas bubbles begin to coalesce to form larger bubbles which change the hydrodynamic and kinematic mechanisms of the flow (Mi et al., 2001). To help model these flows, flow regimes maps were developed by Mishima and Ishii and Taitel et al. (Mishima et al., 1983; Taitel et al., 1980). Flow regimes provide a macroscopic description about the flow in terms of the bubble size, bubble shape, and the interfacial structure, as schematically shown in Figure 1 for vertical two-phase flow (Sun, 2010).

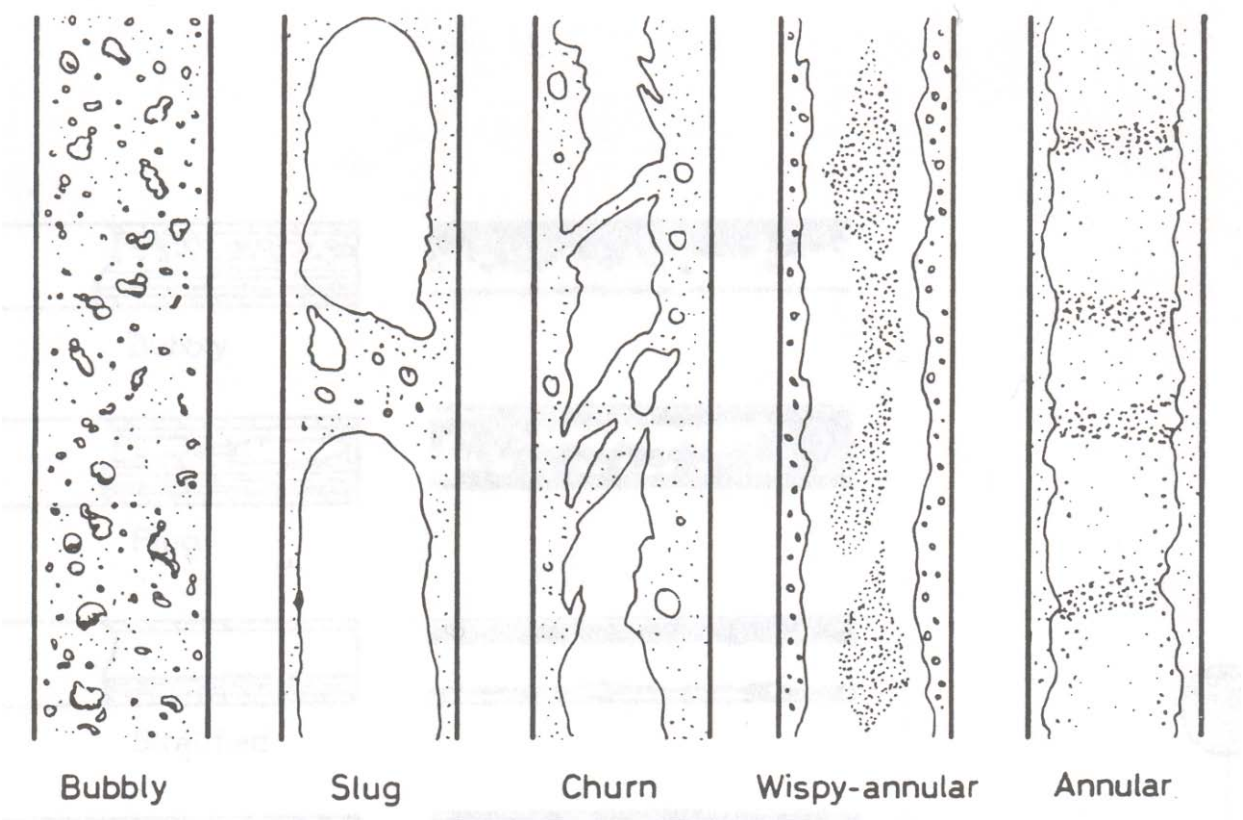

Figure 1: Schematic of flow regimes.

The flow regimes outlined above are, bubbly flow, slug flow, churn flow, wispy-annular flow, and annular flow. The main factor defining the transition for the flow regimes is the void fraction which is defined in Equation (1) (Todreas et al., 1993).

$$\alpha = \frac{A_g}{A} \qquad (1)$$

Where A_g is the area occupied by the gas phase and A is the total flow area. When the void fraction is small, bubbly flow exists. In bubbly flow, the bubbles are usually group I bubbles or spherical/distorted bubbles that are dispersed fairly evenly throughout a

continuous liquid. The maximum spherical and distorted bubble limits are given below in Equations (2) and (3), respectively (Ishii, 1977; Ishii et al., 1979).

$$D_{ds} = 4\sqrt{\frac{2\sigma}{g\Delta\rho}}N_{\mu_f}^{\frac{1}{3}} \qquad (2)$$

$$D_{d\max} = 4\sqrt{\frac{\sigma}{g\Delta\rho}} \qquad (3)$$

Where,

$$N_{\mu_f} = \frac{\mu_f}{\sqrt{\rho_f \sigma \sqrt{\frac{\sigma}{g\Delta\rho}}}} \qquad (4)$$

As the void fraction increases, the small bubbles begin to interact by coalescing and forming larger bubbles or cap bubbles. These cap bubbles keep absorbing smaller bubbles until they reach a diameter which is slightly less than the pipe diameter. At which point they are classified as slug bubbles. The cap bubbles and slug bubbles are referred to as group II bubbles. When slug bubbles are formed, this marks the beginning of the slug flow regime. The slug flow regime can be geometrically viewed as an oscillatory motion between annular flow and bubbly flow (Mi, 1999). The annular flow occurs when a slug bubble passes through an axial cross section of the pipe and the bubbly flow occurs in a continuous liquid that forms between the slug bubbles. At the tail region of the slug bubble the spherical/distorted bubbles continuously coalesce into the slug bubble and the edges of the slug bubble are sheared off to form spherical/distorted bubbles, resulting in continuous group I bubble generation and absorption. The void

fraction can continue to increase in this slug flow regime until the slug bubbles reach a critical length where the surface tension can no longer maintain shape of the long slug bubble and the bubble breaks apart forming the churn flow regime. This flow regime is similar to slug flow in that there is an oscillatory motion between mostly gas and mostly liquid, however for churn flow these oscillations are much more chaotic. As the void fraction continues to increase, the gas begins to form a continuous stream in the center of test section, with small liquid droplets entrained in the flow. This flow regime is called wispy annular, when the void fraction increases further there becomes fewer liquid droplets in the gas stream forming annular flow. This research will focus on the effects of initial bubble size on the downstream development of flow regimes in the two-phase flow. This will be done using an air-water two phase flow loop. The reason for using air-water instead of steam-water is that the experiments can be performed at the ambient temperature and atmospheric pressure. Another reason for doing this is that air-water flow regime maps developed in a pipe with 31.2 mm diameter and at a pressure range of 0.14 to 0.54 MPa have been found suitable for steam-water data in a pipe with 12.7 mm diameter at a pressure range of 3.45 to 6.90 MPa (Todreas et al., 1993).

1.2 Literature Review

This section will give an overview of how impedance void meters or impedance probes and four-sensor conductivity probes were developed.

Impedance void meters were developed by Dr. Ye Mi at Purdue University. These meters use the large difference in conductivity between air and water to determine the impedance of the air-water mixture. Impedance is defined by Equation (5).

$$G = \frac{I}{V} \qquad (5)$$

Where I is the total current passing through each of the electrodes and V is the potential difference between the electrodes. This impedance is then normalized and it can be used to determine the flow regime by passing the mean and standard deviation of the normalized impedance signal for certain test cases to a neural network. This neural network will then group the test cases, at this point subjective judgment can be used to classify the groups into the specific flow regimes. Correlations have also been developed that will be further discussed in Section 2.2.4 to relate the normalized impedance signal to the void fraction (Mi, 1999).

Miniaturized four-sensor conductivity probes were designed by Dr. S. Kim at Purdue University. These probes are used to obtain the time-averaged local two-phase flow parameters of various types of bubbles (Kim et al., 2000). A four-sensor conductivity probe will be used, because it can detect information for both group I bubbles and group II. Conductivity probes take advantage of the difference in conductivity between the air and the water. When the tips of the needles are in contact with water, a current is able to pass through the water to the stainless steel casing of the probe, which acts as the electrical ground. When the tips of the needles are in contact with air the resistance is too high for an electrical current to pass through. Using this difference in conductivity, a conductivity probe is able to measure three main two phase flow parameters for both group I and group II bubbles, the time average bubble velocity, the time averaged local void fraction, and the time averaged interfacial area concentration. The time average bubble velocity can be determined by the time it takes the bubble pass between the

known distance between the upstream sensor and downstream sensor. The time averaged local void fraction is calculated by dividing the sum of the time fraction occupied by air by the total measurement time and the time averaged interfacial area concentration is a function of the velocities found between the upstream sensor and each of the three downstream sensors. The time average void fraction and the time averaged interfacial area concentration can then be related to the Sauter mean diameter by Equation (6).

$$D_{smd} = \frac{6\alpha}{a_i} \qquad (6)$$

Where D_{smd} is the Sauter mean diameter, α is the time averaged local void fraction, and a_i is the time averaged interfacial area concentration (Kim et al., 2000).

1.3 Motivation

The motivation for this research is to determine how the inlet bubble size correlates to the downstream flow regime. This is important data to record because this will allow a mathematical model to be developed that hopefully be integrated into new next generation reactor safety codes. One of the reasons that this is important is that for the current reactor safety codes that are used, the codes have large jumps in flow parameters between flow regimes, which can sometimes cause the safety code to oscillate. With the current safety codes, to account for these oscillations the reactor has to be operated at a lower power. The purpose for this is to provide a “buffer region” to make sure the reactor is operated safety. This research will focus on the transitions between the flow regime boundaries to provide a smoother transition between the flow

regimes. This will allow the reactors to have power up rates, which will allow the reactor to generate more electricity without a large capital investment.

1.4 Project Objective

The objective for this research is to find a relationship between the inlet bubble size and the downstream flow regime development near the transition. To accomplish this objective, the air-water test facility will need to be modified to allow for a greater range of inlet bubble sizes that can be produced and so that larger flow rates could be achieved. The modifications that need to be completed are to fix the leaks that exist in the current test facility, install a larger air-water separator, and modify the water supply lines to the bubble injector. Instrumentation will also need to be built and integrated into the test facility to measure important two-phase flow parameters. The instrumentation that needs to be build and/or installed are pressure and differential pressure transducers, a turbine flow meter, impedance probes, and miniaturized four-sensor probes. The instrumentation will then need to be verified to make sure that it works correctly and the different flow regimes can be observed and then at a later time the data that will look at the inlet bubble size to the downstream flow regime transition will need to be collected.

Chapter 2: Experimental Description

2.1 Experimental Setup

Modification of the old test facility was needed so that a greater range of inlet bubble sizes can be produced and so larger flow rates can be achieved in the test facility. The old test loop shown below in Figure 2.

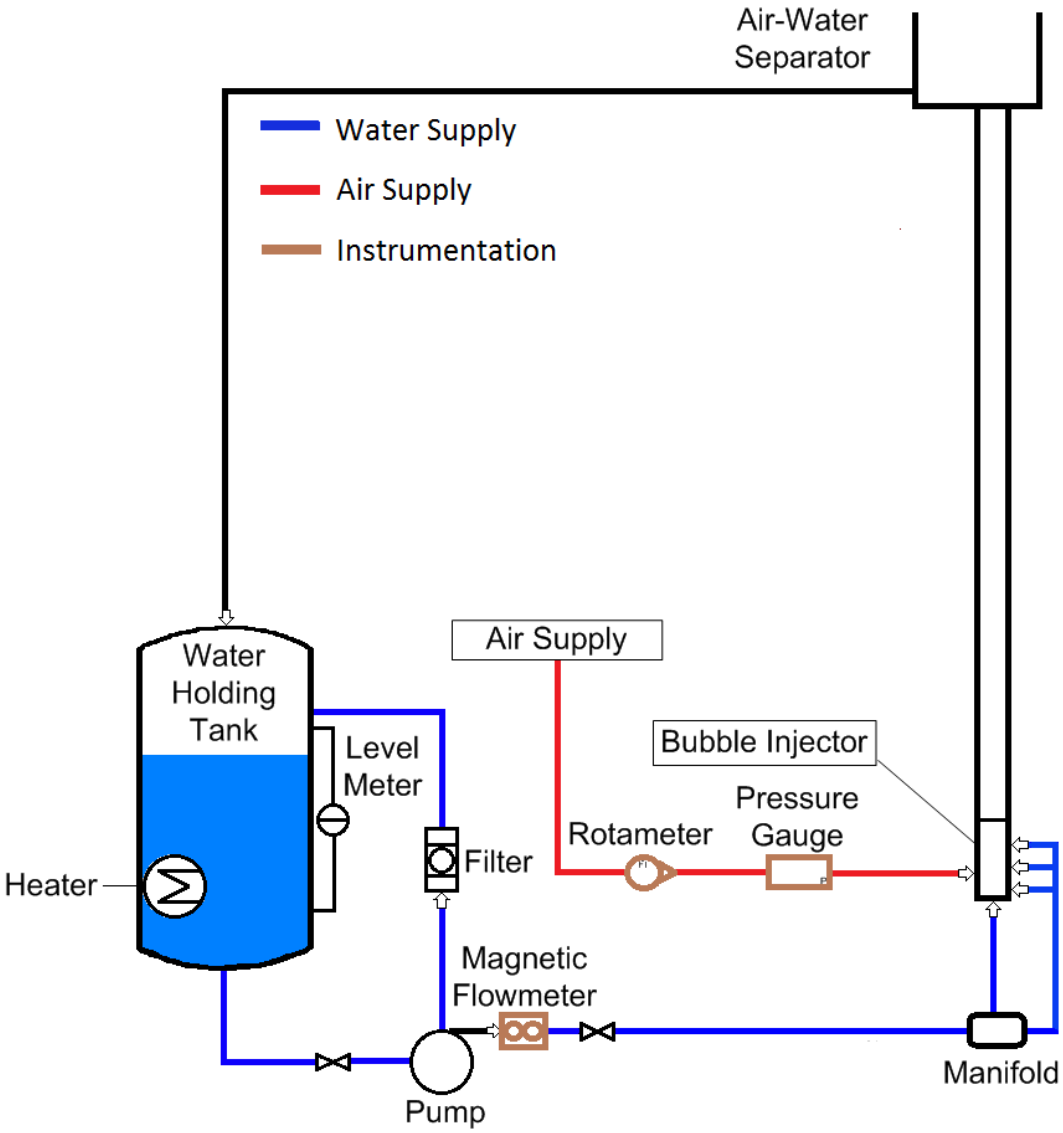

Figure 2: Schematic of the old test facility.

The old test facility consisted of a heated water storage tank, a filter, pump, a magnetic flow meter, a 2” acrylic vertical circular pipe that is 8’ in height that acts as the test section, and a bubble generator. The minimum temperature of the water in the test facility is fixed by room temperature, and the maximum temperature is fixed by the melting point of acrylic, these limits give an operate range of 20-90 °C. The pressure that the tests section can operate at is 1 atm because the air-water separator is open to the atmosphere. The maximum air flow rate is 1465 ft^3/hr when the pressure at the inlet to the test section is approximately equal to 14.7 psi and the maximum water flow rate is 53 gpm when the test section is filled with water. To make the flow loop operable the first thing that needed to be done was the air-water separator needed to be replaced with a larger tank, because the previous separator did not have sufficient room for the air-water mixture to completely separate, so the air that was released to the room still contained entrained water droplets. The larger tank that is currently installed is twice the size of the old water tank, and has dimensions of the tank are 24”x12”x24”. Another modification to the old facility was to have two independent water flows enter the bubble injector. The reason for this can be explained by taking a closer look at the bubble injector which is shown below in Figure 3.

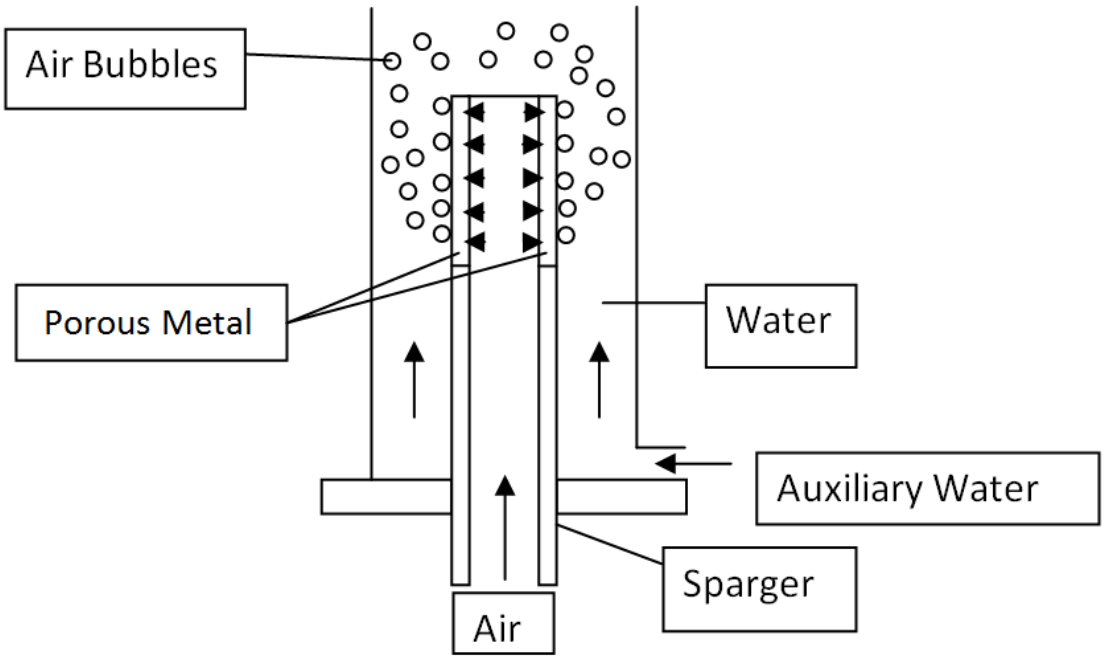

Figure 3: Schematic of the bubble injector.

The most important part of the bubble injector is the sparger. The sparger is a stainless steel tube that is closed at one end and has a 7" porous metal section. The porous section is made of sintered metal and has an average pore size of 10 microns. To generate bubbles, air is passed into the sparger, and it permeates through the porous metal and collects on the outside of the sparger. The auxiliary water then rushes through the annulus that is formed by the sparger and the larger encompassing tubing, shearing the bubbles from the sparger. The size of the bubbles entrained in the water are estimated by a balance on the drag force, buoyancy force and surface tension force, this is equations is given below in Equation (7).

$$C_D \frac{\rho_f v_f^2}{2}\left(\pi\left(\frac{d_b}{2}\right)^2\right)+g\Delta\rho\left(\frac{4}{3}\pi\left(\frac{d_b}{2}\right)^3\right)=2\pi r_o\sigma \qquad (7)$$

Where C_D is the coefficient of drag, ρ_f and ν_f is the density and velocity of water, d_b is the bubble diameter, g is the gravitational constant, $\Delta\rho$ is the difference in density between air and water, r_o is the average pore size of the sparger, and σ is the surface tension between the air and the sintered metal. In order to control in size of the inlet bubbles it is necessary to change either the average pore size of the sparger or the velocity of the liquid. For this reason it was determined that the auxiliary water needed to be independently controlled from the main water supply. To do this the flow was split before the manifold and a turbine flow meter was added to this new auxiliary water line. Preliminary testing was performed using this new auxiliary water line to vary the inlet size of the bubble it was determined that by changing the water velocity, the range of inlet bubble sizes was not large enough for the current average pore size of the sparger. Using Equation (7) and the maximum velocity range that the auxiliary water line can achieve it was found that a larger average pore size of the sparger gave a larger range of inlet bubble sizes. A sparger with a larger average pore size has been ordered and will be used in a later stage of the project.

To monitor the flow, instrumentation had to be added to the system. The instrumentation that was added and will be discussed further in Section 2.2 are a pressure transducer, a differential pressure transducer, a high-speed video camera, impedance void meters, and four-sensor conductivity probes. A schematic of the new test facility with the modifications included is shown below in Figure 4.

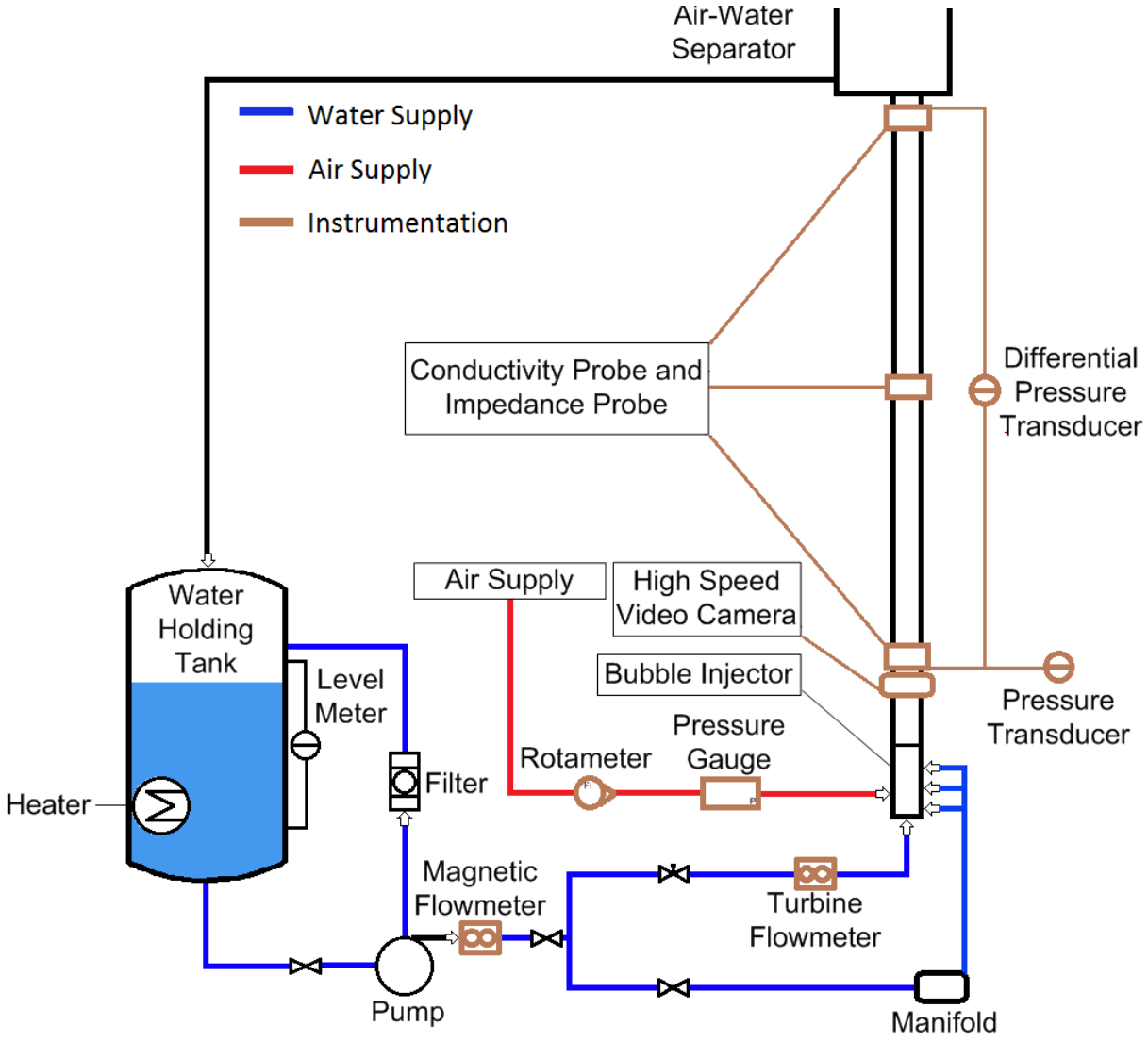

Figure 4: Schematic of the test facility.

The pressure transducer measures the pressure at the inlet of the test section. The differential pressure transducer measures the pressure drop across the test section. The high-speed video camera gives a representative view of the inlet flow conditions. The impedance void meters and conductivity probes are placed at the inlet, middle and outlet of the test section. The impedance void meters measure the impedance across the test section, which can be related to the void fraction and flow regime. The four-sensor conductivity probes measures the conductivity at local radial positions along the

test section and gives information about the bubble velocity, local void fraction, and the interfacial area concentration.

2.2 Instrumentation

This section describes the instrumentation that will be built and installed to measure important two-phase flow parameters. The instruments that will be used are flow meters, pressure transducers, a high-speed video camera, impedance void meters, and conductivity probes.

2.2.1 Flow Meters and Rotameters

Two flow meters will be used measure the water flow rate. The first flow meter is a magnetic flow meter and it measures the total water flow rate. The magnetic flow meter is a Yamatake magnew two wire plus flow meter that has a maximum range of 0-140 gpm ±0.5% the maximum flow. The range of the used for this research is 0-60 gpm with an uncertainty of ±0.3 gpm. The other flow meter is a turbine flow meter that measures the flow of the auxiliary water that passes through the bubble injector, using this flow rate the water velocity that passes through the annulus of the bubble injector can be determined. This flowmeter is an Omega FTB-1316 with a range of 0-32 gpm with an uncertainty of 0.32 gpm. The magnetic flow meter is used to record the water superficial velocity by using Equation (8) where *i* equals *f*.

$$j_i = \frac{Q_i}{A} \qquad (8)$$

The error associated with the total flow rate measurement needs to be propagated through to the water superficial velocity. This can be done by using Equation (9) below.

$$\delta j_f = \sqrt{\left(\left(\frac{\partial j_f}{\partial Q_f}\right)^2 \delta {Q_f}^2\right)} = \frac{\delta Q_f}{A} \qquad (9)$$

The uncertainty associated with the water superficial velocity is ±0.012 m/s for all values of j_f.

To measure the air flow rate, a series of rotameters are placed in parallel ranging from 0-5 SCFH to 0-500 SCFH. The uncertainty in the measurement of the air flow rate for the rotameters used, is ±2% of the maximum range. The rotameters determine the flow rate of air in SCFH, and a Span pressure gauge with a range of 0-60 psig and uncertainty of ±1.2 psig is placed between the rotameters and the entrance to the test loop to measure the back pressure so that the relationship between the actual flow rate and the standard flow rate of air can be determined by using Equation 10.

$$Q_{g,actual} = Q_{g,standard} \sqrt{\frac{P_{standard} \times T_{actual}}{P_{actual} \times T_{standard}}} \qquad (10)$$

Where $Q_{g,actual}$ and $Q_{g,standard}$ are the actual flow rate of air between rotameters and inlet to the test section and the standard flow rate of air respectively, P_{actual} and $P_{standard}$ are the actual absolute pressure measured by the Span pressure gauge and standard pressure (atmospheric pressure, 14.7 psia) respectively, and T_{actual} and $T_{standard}$ are the actual absolute temperature and the standard absolute temperature (293 K) respectively. To find the flow rate of air at the inlet, middle, and outlet of the test section, the air was assumed to act as an ideal gas and using the ideal gas law, Equation 11 was derived.

$$Q_{g,i} = Q_{g,j} \frac{P_j}{P_i} \frac{T_i}{T_j} \qquad (11)$$

Here it is important to note that the temperature terms are defined for an absolute temperature scale. The rotameters are used to measure the air superficial velocity by using Equation (8) where *i* equals *g*. The error associated with the air flow rate and the pressure gauges need to be propagated to the gas superficial velocity. This is done by combining Equations (8), (10), and (11). Using a similar approach as used to propagate the water superficial velocity, Equation (12) was derived to find the uncertainty in the inlet air superficial velocity assuming that the temperature throughout the system is equivalent.

$$\delta j_g = \sqrt{\left(\frac{\partial j_g}{\partial Q_{g,standard}}\right)^2 \left(\delta Q_{g,standard}\right)^2 + \left(\frac{\partial j_g}{\partial P_1}\right)^2 \left(\delta P_1\right)^2 + \left(\frac{\partial j_g}{\partial P_{back}}\right)^2 \left(\delta P_{back}\right)^2} \qquad (12)$$

$$\delta j_g = \sqrt{\left(P_{standard} P_{back}\right)\left(\frac{\delta Q_{g,standard}}{A P_1}\right)^2 + \left(\frac{P_{standard}}{2 P_{back}}\right)\left(\frac{\delta P_1 Q_{g,standard}}{A P_1}\right)^2 + \left(P_{standard} P_{back}\right)\left(\frac{\delta P_{back} Q_{g,standard}}{A P_1^2}\right)^2}$$

(13)

It is important to note is that this that the uncertainty for j_g is dependent on the flow parameters as opposed to the uncertainty of j_f , where the uncertainty is constant.

2.2.2 Pressure Transducers

A Honeywell STG140 gauge pressure transducer records the pressure that enters the test section of the experimental loop. This pressure transducer has a rangeability of 0-5 to 0-500 psig with an uncertainty of ±0.075% of the full range. For the system being

studied the range for the pressure transducer is 0-10 psig with an uncertainty of ±0.008 psig. A Honeywell STD924 differential pressure transducer measures the pressure drop between inlet and outlet of the test section. This differential pressure transducer has a rangeability of 0-0.5 to 0-14.5 psi with an uncertainty of ±0.075% of the calibrated span or upper range value, whichever is greater. For the system being studied a range of 0-2.16 psi with an uncertainty of ±0.0016 psi was used. The reading that is acquired from the differential pressure transducer can be related to the pressure drop across the test section by Equations (14) and (15).

$$DP_r = P_2 - P_1 + \rho_f gh \qquad (14)$$

$$\Delta P_m = P_1 - P_2 \qquad (15)$$

Where DP_r is the reading from the differential pressure transducer, P_2 is the pressure at the outlet of the test section, P_1 is the pressure at the inlet of the test section, and ΔP_m is the actual differential pressure of the air-water mixture. The pressure drop across the test section can be related to the void fraction by assuming that the flow rate is very small and a constant flow area exists in the test section. These assumptions allow the differential pressure of the air-water mixture to be approximated as the change in pressure due to gravity. Then assuming that the density of water is much greater than the density of air, the void fraction is related to the differential pressure of the mixture, as defined in Equations (16) and (17) (Mi, 1999).

$$\Delta P_m = \Delta P_{gravity} = \rho_m gh \approx \rho_f \left(1-\alpha\right) gh \qquad (16)$$

$$\alpha = 1 - \frac{\Delta P_m}{\rho_f g h} = \frac{DP_r}{\rho_f g h} \qquad (17)$$

Where ρ_m is the mixture density, ρ_f is the liquid density, h is the distance between the inlet and outlet of the test section, g is the gravitational constant, and α is the void fraction. To find the uncertainty of the void fraction, the error from the differential pressure reading is propagated through by using Equation (18).

$$\delta\alpha = \sqrt{\left(\left(\frac{\partial\alpha}{\partial DP_r}\right)^2 \left(\delta DP_r\right)^2\right)} \qquad (18)$$

The uncertainty of the void fraction measurement is ±0.0005.

This linear relationship between the differential pressure reading and void fraction can be used to aid in determining the flow regime for low flow conditions. For these low flow conditions, assuming the mixture flow is below 2000 (kg/m2 s), the void fraction can be directly related to the flow regime using a vertical flow regime map used in RELAP-5. Table 1 below shows the flow regime and transitions for various flow regimes (Todreas et al., 1993).

Table 1: Vertical regime map of RELAP-5.

Area Averged Void Fraction	Flow Regime
0.0 - 0.1	Bubbly (BBY)
0.1 - 0.2	Transition (TBS)
0.2 - 0.65	Slug (SLG)
0.65 - 0.85	Transition (TSA)
0.85 - 0.90	Annular (ANN)
0.90 - 0.95	Transition (TAM)
0.95 - 1.0	Mist (MST)

2.2.3 High-speed Video Camera

The high-speed video camera that will be used is a Motion Engineering FASTCAM-512 PCI 32 K Monochrome Camera which has a maximum frame rate of 32,000 frames per second and a picture resolution of 512x32 pixels. The maximum velocity of the flow mixture is small enough that a lower frame rate and higher resolution can be employed to accurately capture the flow images. The frame rate and resolution that will be used for the experiments are 500 frames per second and 512x512 pixels respectively. The camera will be positioned at the inlet of the test section and will give a visual representation of the inlet flow structure.

2.2.4 Impedance Void Meters

The impedance void meters use the difference in conductivity between air and water. The circuit used for the impedance void meters, passes a sine wave with a frequency of 100 kHz through the electrodes of the void meter and the circuit detects the manipulated signal and gives an output voltage that is proportional to the impedance G. This impedance signal is then normalized, using Equation 19.

$$G^* = \frac{G - G_g}{G_f - G_g} \qquad (19)$$

Where G^* is the normalized impedance, G_f is defined as the impedance when the test section is filled with water and G_g is defined as the impedance when the test section is filled with air. The normalized impedance can be related to the void fraction for bubbly flow, by assuming the void fraction distribution is uniform by Equation 20.

$$G^* = 1 - \frac{3\alpha}{2+\alpha} \qquad (20)$$

For annular flow if the liquid droplets entrained in the gas stream are ignored then the normalized impedance can be related to area averaged void fraction by Equation 21.

$$G^* = 1 - \alpha \qquad (21)$$

For slug and churn flow the normalized impedance is related by fitting a seventh order polynomial to the numerical integration of the governing equation of the electrical field which can be found in Equation 22 (Mi, 1999).

$$G^* = -3.4794\alpha^7 + 13.8170\alpha^6 - 21.1873\alpha^5 + 15.1098\alpha^4 - 4.2297\alpha^3 - 0.1508\alpha^2 - 0.8799\alpha + 1.0000 \qquad (22)$$

Although knowing the void fraction is important and can be related to the flow regime using Table 1. A more important aspect is being able to determine the flow regime directly from the normalized impedance signal for different flow conditions. The procedure for determining the flow regime is to first find the mean and standard deviation of the normalized impedance, which gives the probability density function for the impedance. Once the mean and standard deviation are known the different test cases can then be classified subjectively by looking at the mean and standard deviations of definitive bubble, slug, and churn flow regimes and then finding similar means and standard deviations from the test cases and grouping them with these definitive cases. A more objective method of determining the flow regime is to pass the mean and standard deviation into a self organizing neural network along with the definitive flow regime cases and the neural network will classify the cases based similarities. A neural network attempts to model the functioning processes of the human

brain, which enables the neural network to learn non-linear mappings and to understand hidden relations. Using a neural network enables direct relationship to be established between the experimental data and flow regime models. This in turn eliminates human subjectivity interference, thereby greatly improving the objectivity of identifying different flow regimes.

The impedance void meter is constructed, by machining an acrylic block and placing two electrodes into the sides of the machined block. A drawing of this block is found below in Figure 5.

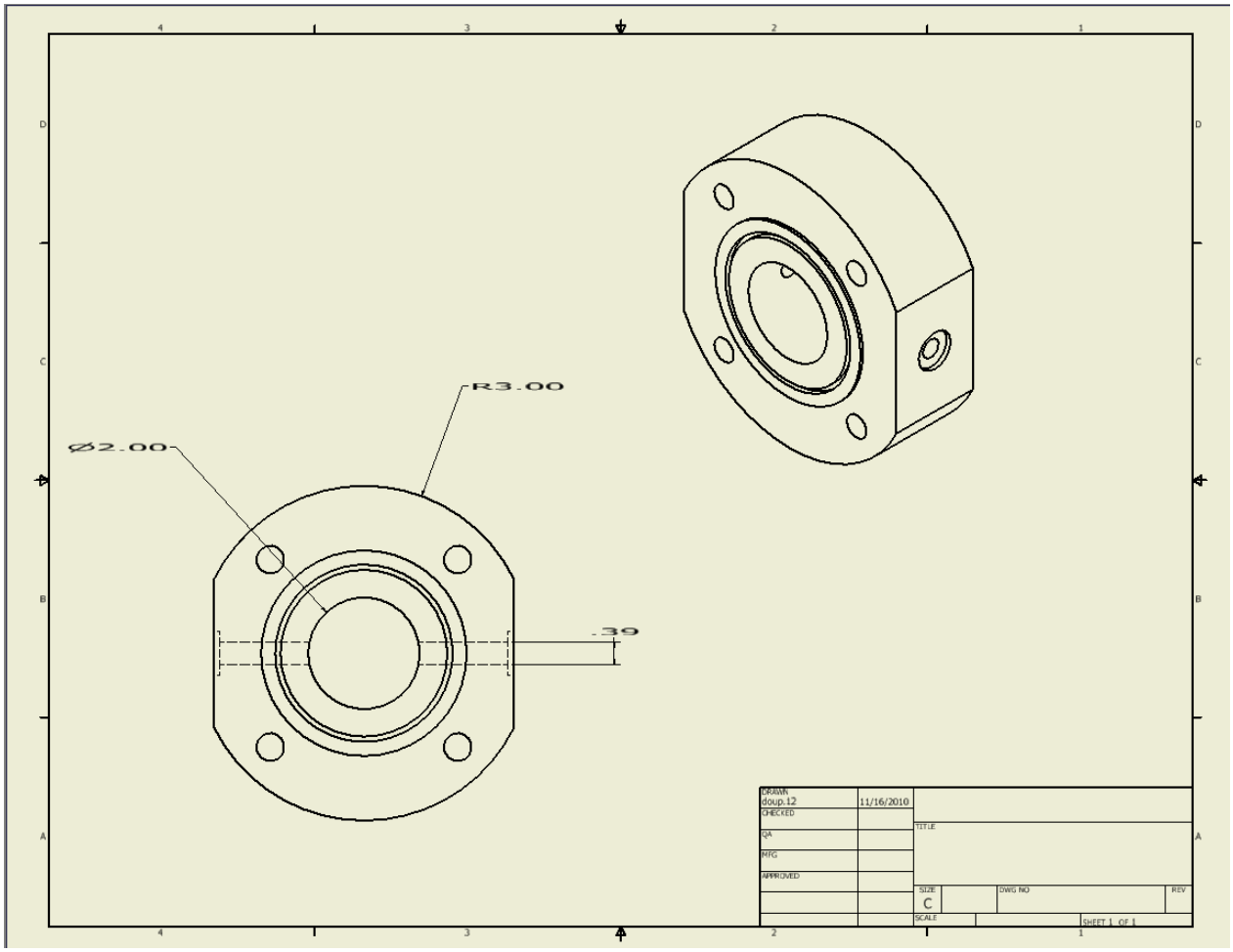

Figure 5: Drawing of the impedance probe.

2.2.5 Four-Sensor Conductivity Probes

The four-sensor conductivity probe uses the difference in conductivity between air and water to determine important two-phase flow parameters that have been outlined in Section 1.2. The process for building a four-sensor conductivity probe is to coat gold plated acupuncture needles that are approximately 0.15 mm in diameter with a thin Teflon coating. The approximate thickness of the Teflon coating is 0.08 mm thick and the reason for coating the needles is to make them electrically insulated. The coating at the very tip of the needle is ground off so that an electrical current can pass through the tip of the needle and to the ground casing when the tip of the needle is in contact with water. Below in Figure 6 is a microscopic image of an uncoated needle and coated needle.

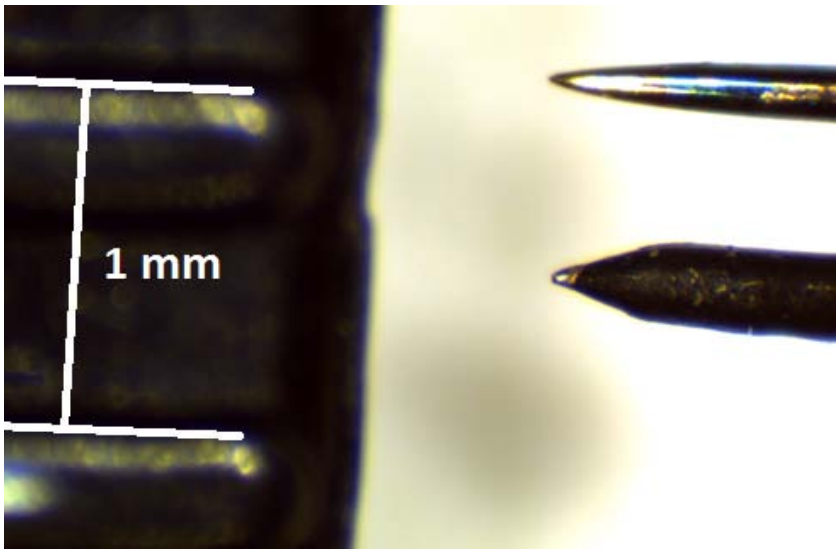

Figure 6: Microscopic image of coated versus uncoated needle.

The coated needles are then connected to 27 gauge thermocouple wires which act as the leads for the probe. The needles are arranged using a four-bore ceramic tube, into an ideal arrangement, which is shown in Figure 7(Fu et al., 1999).

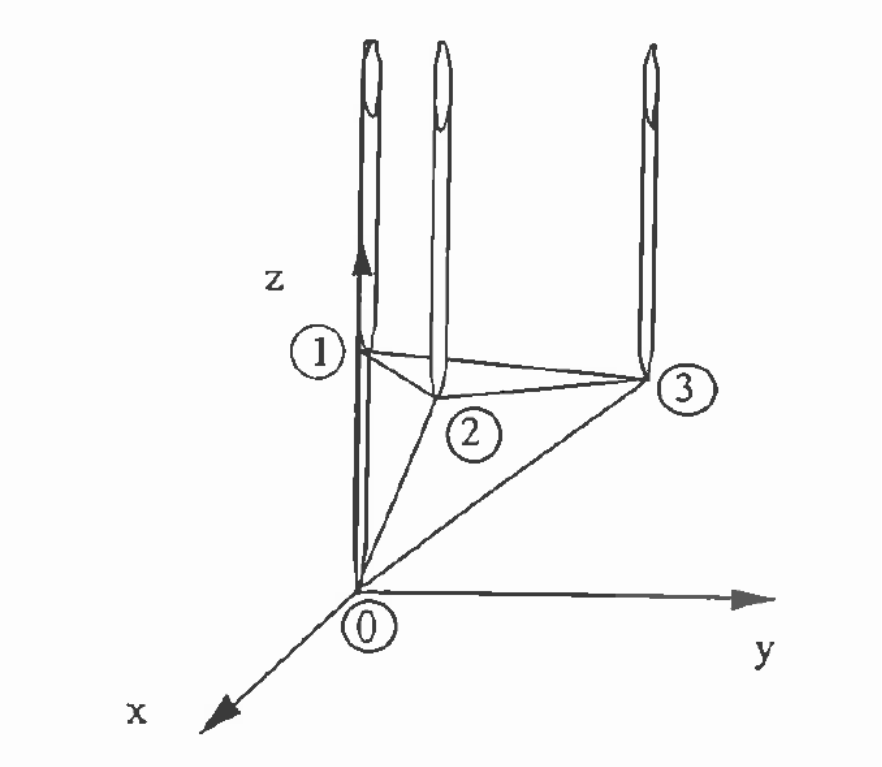

Figure 7: Schematic of an idealized arrangement for a four-sensor conductivity probe.

The important thing to notice about this Figure is that probe 0 is positioned downstream of the other three probes, which enables the average bubble velocity and time averaged interfacial area concentration to be determined. The arranged needles are then connected to 11 gauge stainless steel tubing using copper bond epoxy. Below in Figure 8 is a picture of a completed conductivity probe and in Figure 9 is a microscopic image of the four sensors.

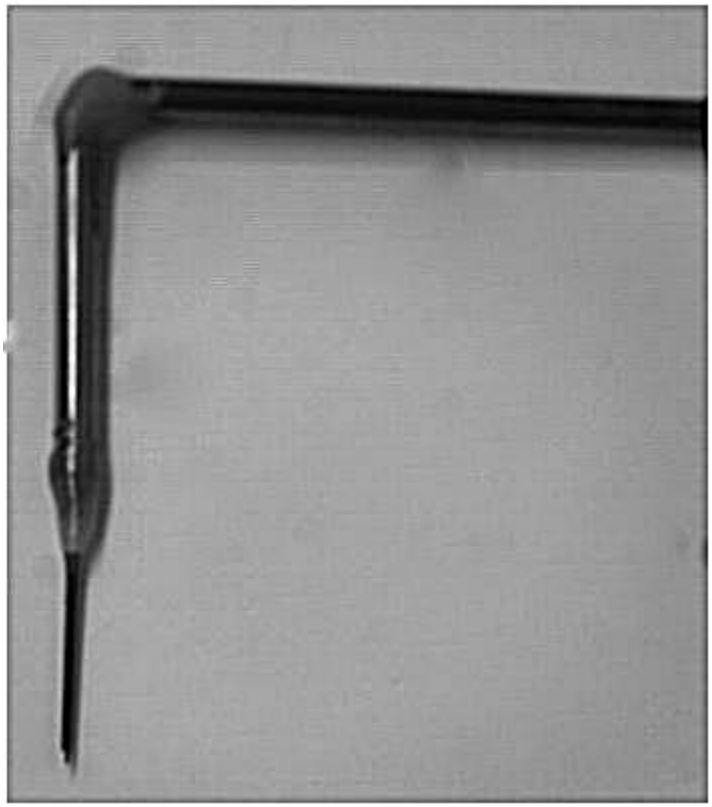

Figure 8: Photograph of a four-sensor conductivity probe.

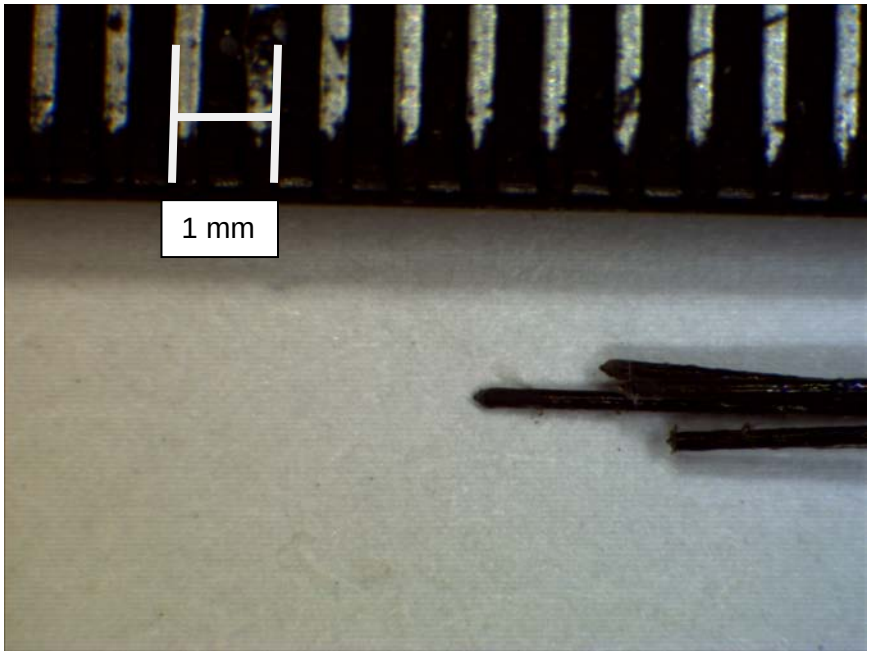

Figure 9: Microscopic image of arrangement of four-sensor probe.

The stainless steel tubing not only acts as the ground for all four needles but also acts as a mechanical support for the probe and houses the thermocouple wires that connect to the four-sensor probe.

To hold the four-sensor probe in place a probe support had to be manufactured. Below in Figure 10 is a drawing of the probe support.

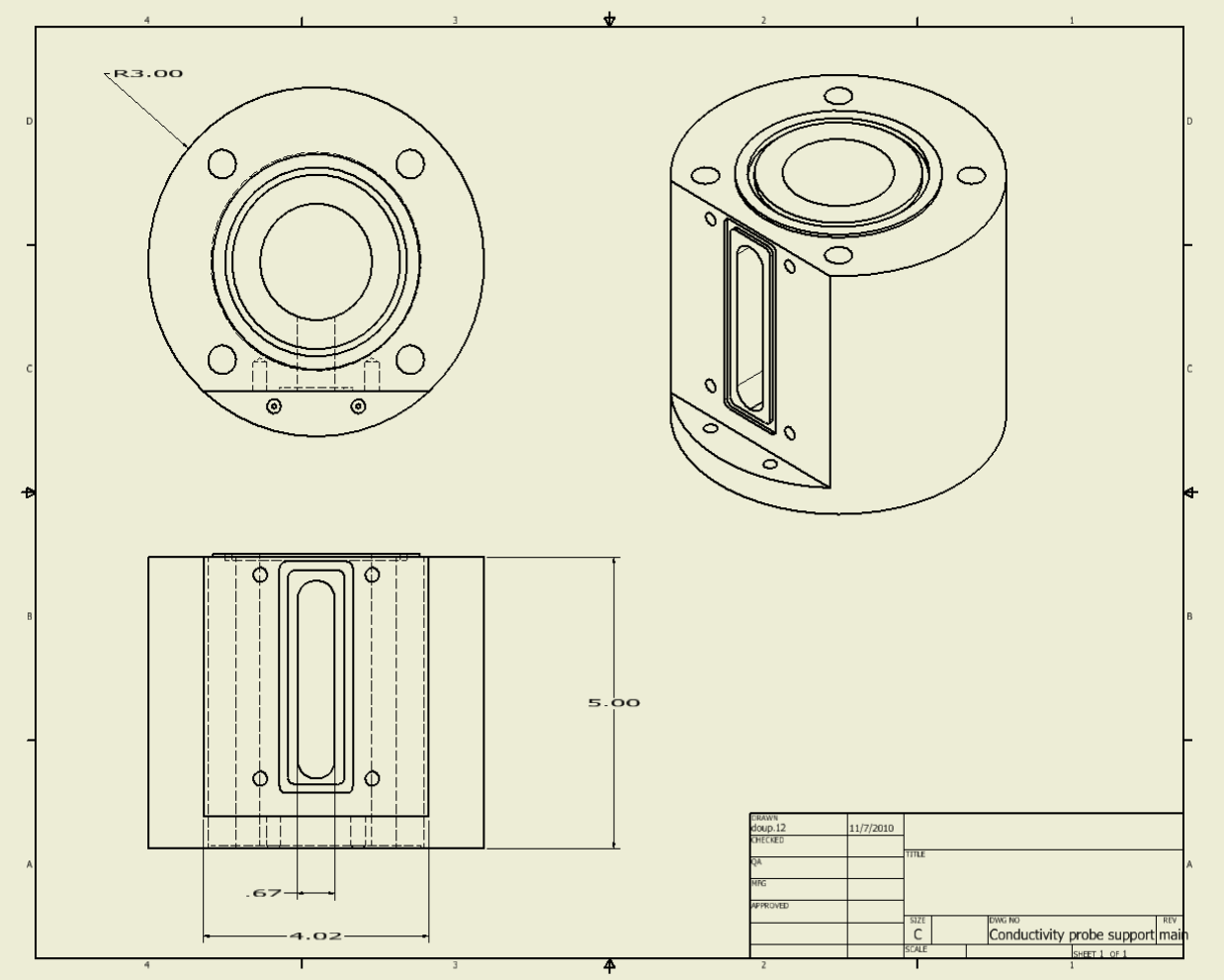

Figure 10: Drawing of conductivity probe support.

The important thing to notice about the drawing, is that on the side of the support there is a rectangular insert that allows for the probe to be moved in and out of the test

section. The probe is traversed radially along the tests section by a Deltron Precision micrometer positioning slide that has a range and uncertainty of 2” and ±0.005” respectively. Below in Figure 11 is a picture of the conductivity probe support.

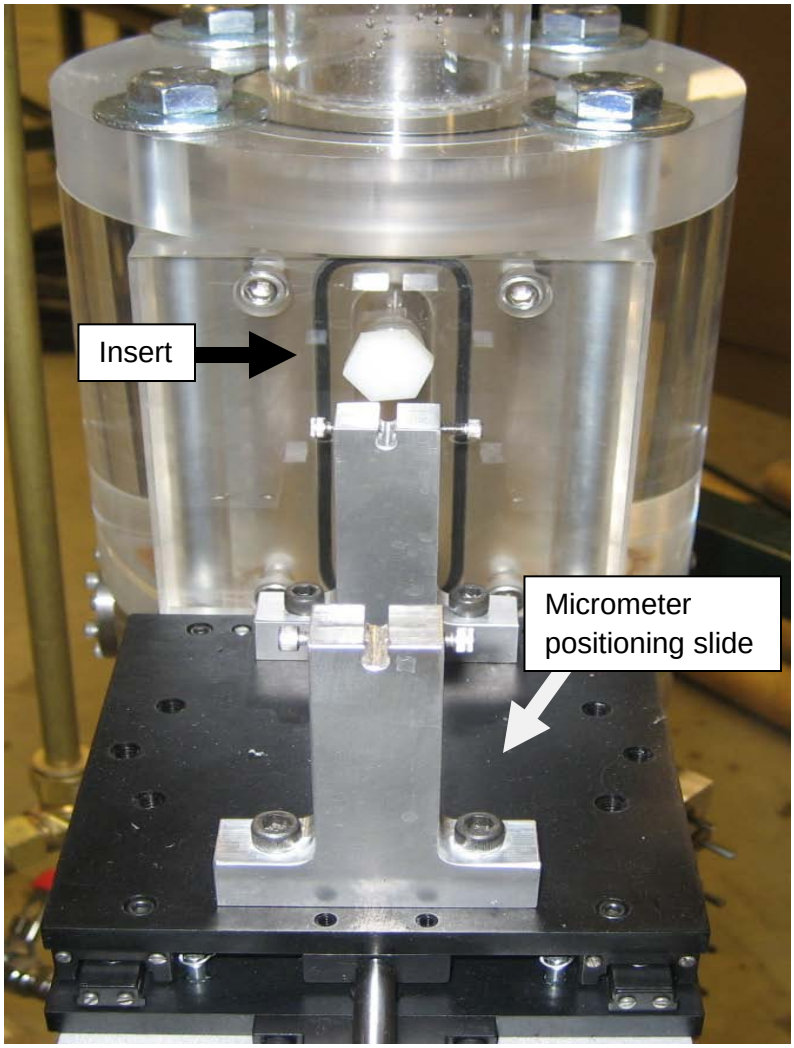

Figure 11: Picture of a conductivity probe support.

To acquire the signal from the four-sensor probe a DC circuit is used that measures the voltage difference across a series of resistors, and because the resistance in the circuit is constant the difference in voltage across the resistor is related to the changes in current flowing through the circuit and is governed Ohm’s law which is found below in

Equation 23. The changes in the flowing current are related to the changes in conductivity when the probe is in contact with air or water.

$$V = IR \qquad (23)$$

Where V is the difference in voltage, I is the current, and R is the resistance. The circuit that is used is found below in Figure 12.

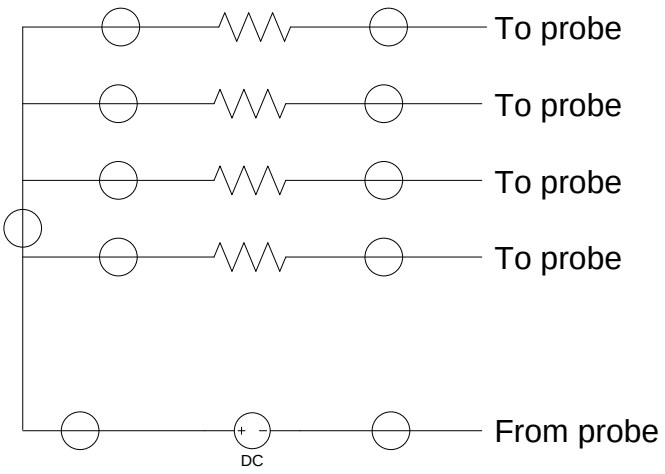

Figure 12: Four-sensor conductivity probe circuit.

The DC power source supplies a voltage difference of 5 volts and the maximum current is ±100 mA. This circuit allows each of the probes to be measured and recorded simultaneously by the data acquisition system.

2.3 Data Acquisition System

The data acquisition system that was used to measure the output of the instruments is a National Instruments PCIe-6353 which has a 32 single ended analog input channels or 16 differential analog input channels. The PCIe-6353 has a maximum sampling

frequency of 1.25 MS/s. The software that will be used to communicate with the PCIe board is LabVIEW Signal Express 2009.

Chapter 3: Experimental Data

3.1 Test Matrix

The methodology that was employed to determine the test matrix is that since flow regime maps has already been studied in previous research. A one at a time approach was employed to determine if the different flow regimes could be identified. A one at a time approach is when, one variable is held constant while another variable is changed. For this research the liquid superficial velocity was held constant and the gas superficial velocity was varied. The test matrix is below in Table 2.

Table 2: Test matrix.

Test	j_f (m/s)	j_g (m/s)	measurements taken
1	0.25	0.08	Impedance and differential pressure
2		0.15	
3		0.23	
4		0.47	
5		0.6	
6		0.76	
7	0.5	0.07	Impedance, conductivity, and differential pressure
8		0.15	
9		0.23	
10		0.47	
11		0.65	
12		0.75	
13	1	0.15	Impedance and differential pressure
14		0.22	
15		0.3	
16		0.37	
17		0.45	
18		0.63	

The reason for different distributions of j_g for the three different j_f's, is that data points were chosen from Figure 13, in an attempt to show a transition from bubble flow to slug flow and from slug flow to churn flow.

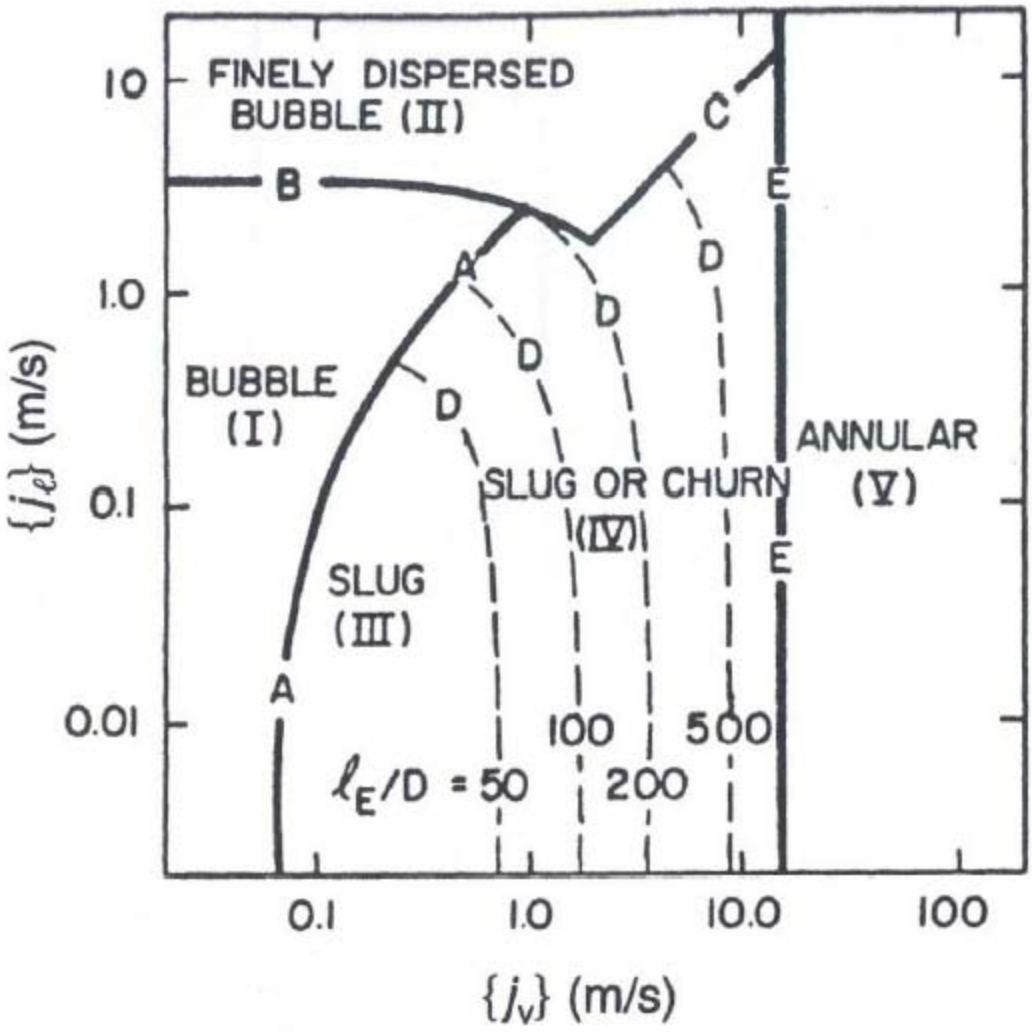

Figure 13: Flow regime map for air-water at 25°C, 1 atm, and for test section diameter = 50m.

For these tests, the measurements that were taken were: a visual representation of the inlet conditions were captured using a high-speed video camera, the differential pressure between the inlet and outlet of the test section was measured, an impedance

signal is taken at the inlet, middle, and outlet of the test section, and for tests 7-12 the conductivity probe data was recorded at 7 different radial locations. The reason that the conductivity probe was only used at one value of j_f is that due to time constraints it was not feasible to use the conductivity probe at the other values of j_f. The 7 different radial locations are spaced at an interval of 0.2 *r/R* between 0 and 0.6 *r/R*, and then at an interval of 0.1 *r/R* between 0.6 and 0.9 *r/R*. Ideally a maximum radial value of 1.0 *r/R* is preferable, however due to the design of and the imperfections in the conductivity probe, the maximum radial value that was obtained was 0.9 *r/R*. The reason that there are more data points for larger *r/R* is that it is assumed that the flow structure is radially uniform. For larger values of *r/R* the circumference is much larger than for smaller values of *r/R*, so for larger *r/R* values there is more area that the intervals between the test points represent, compared with smaller *r/R* values.

3.2 Raw Data

The differential pressure transducer data was recorded and the void fraction was found using Equation (14). In Figure 14 is a graph of the void fraction versus the air superficial velocity. For all three water superficial velocities as the air superficial velocity increases the void fraction increases. This is expected, because as the flow rate of air increases relative to the flow rate of water the area of air should increase relative the total flow area. When the water superficial velocity is increased relative to the air superficial velocity the void fraction decreases. This is expected, because as the flow rate of water increases relative the flow rate of air, the area of air relative to the total flow area should decrease.

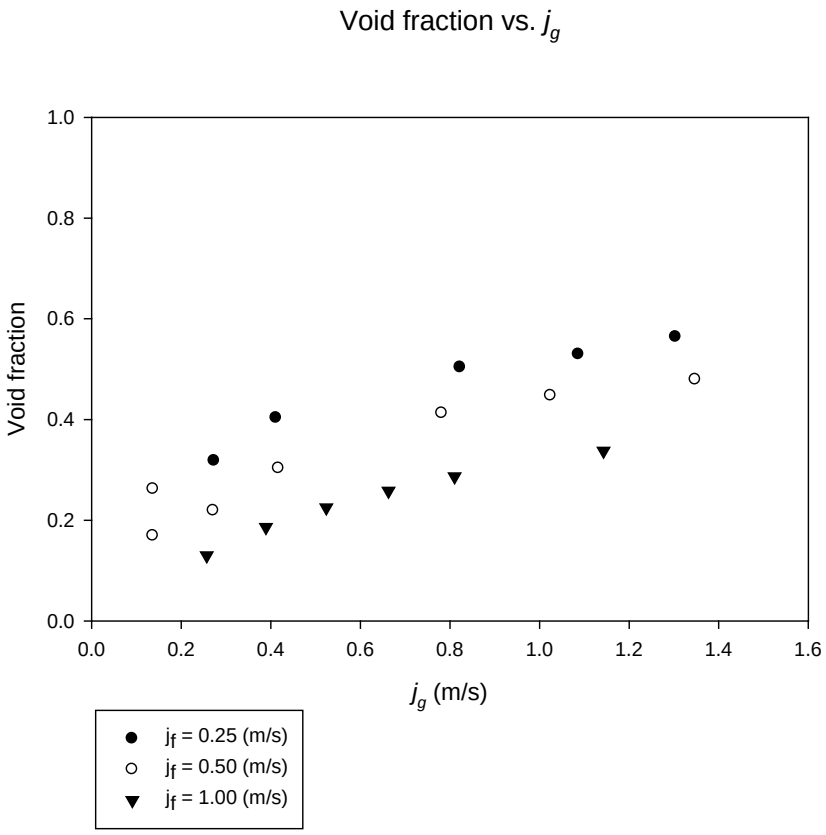

Figure 14: Void fraction vs. j_g.

The images taken with the high-speed video camera and the data recorded from the impedance probe will be analyzed for each different liquid superficial velocity. The four-sensor conductivity probe data will be analyzed for the test points when j_f = 0.5 m/s. The four-sensor conductivity probe at the inlet to the test section will be used to record this data. The reason that only one conductivity probe will be used, is due to time constraints only one working conductivity probe was made.

The first set of data that will be analyzed is when j_f = 0.25 m/s. The high-speed video images for the test are shown below in Figure 15. The j_g's defined for the images are the inlet air superficial velocities.

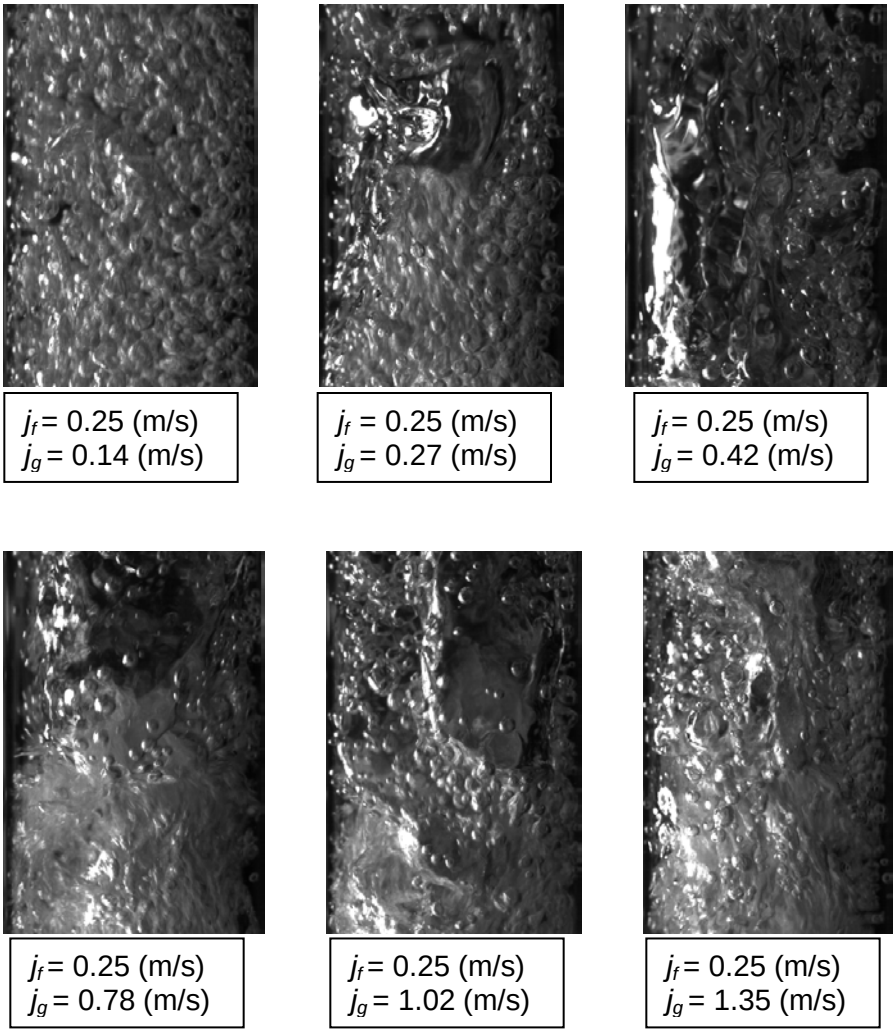

Figure 15: High-speed images of the inlet flow conditions for j_f = 0.25.

The images show that as the superficial air velocity increases the bubble size increases and the flow becomes more turbulent. This is expected because from Figure 13 as j_g increases while holding j_f constant the flow regime changes from bubbly to slug and then from slug to churn. From the images in Figure 15, it is determined that the high-speed video camera can observe the flow regime transitions.

To analyze the impedance void meter data, the average and standard deviation of the normalized impedance signals at *L/D* = 0, 25, and 49 are first examined in Figure 16.

The values of j_g are the local superficial air velocities that are calculated using Equation 8 for all of the impedance measurements. For all three axial positions the standard deviation at the point j_g = 0.14 m/s are considerably smaller than the standard deviations for larger values of j_g. This indicates that when j_g = 0.14 m/s the flow is in the bubbly flow regime, and for the other values of j_g the flow is either in the slug or churn flow regime. From Figure 16 there does not appear to be a distinguishing feature to differentiate between slug and churn flow. However, the normalized impedance signal will be examined closer in an attempt to determine if the difference between slug and churn flow regimes can be observed.

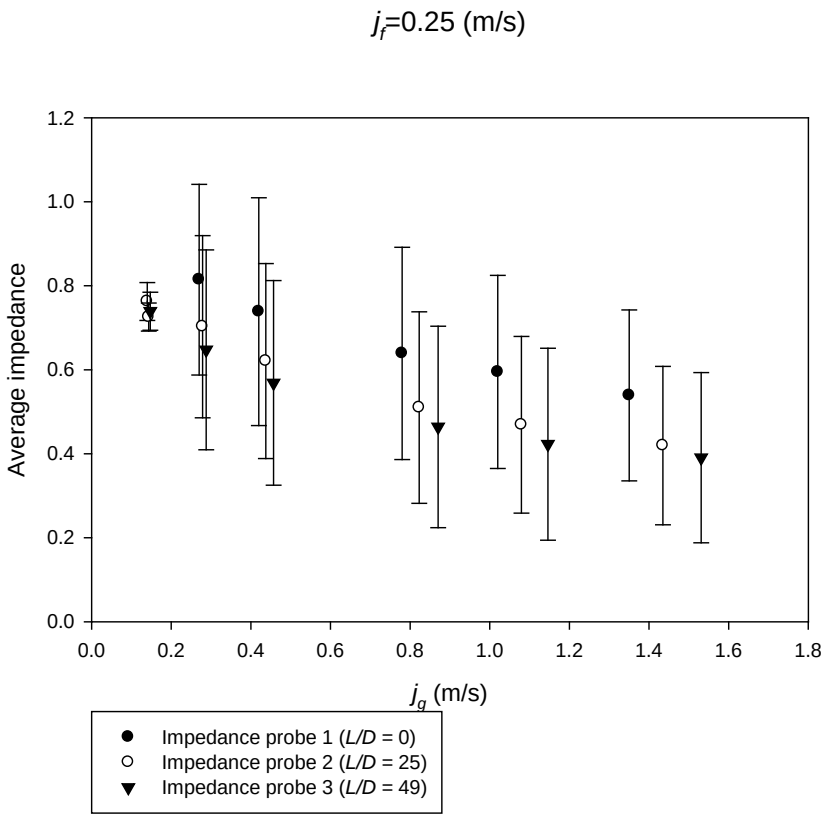

Figure 16: Average and standard deviation of the impedance signals when j_f = 0.25 m/s.

The average impedance values for each of test point when j_f = 0.25 m/s was used to calculate the void fraction using Equation 20. Equation 20 makes the assumption that the void fraction distribution is uniform, so the calculated values of the void fraction are approximate values.

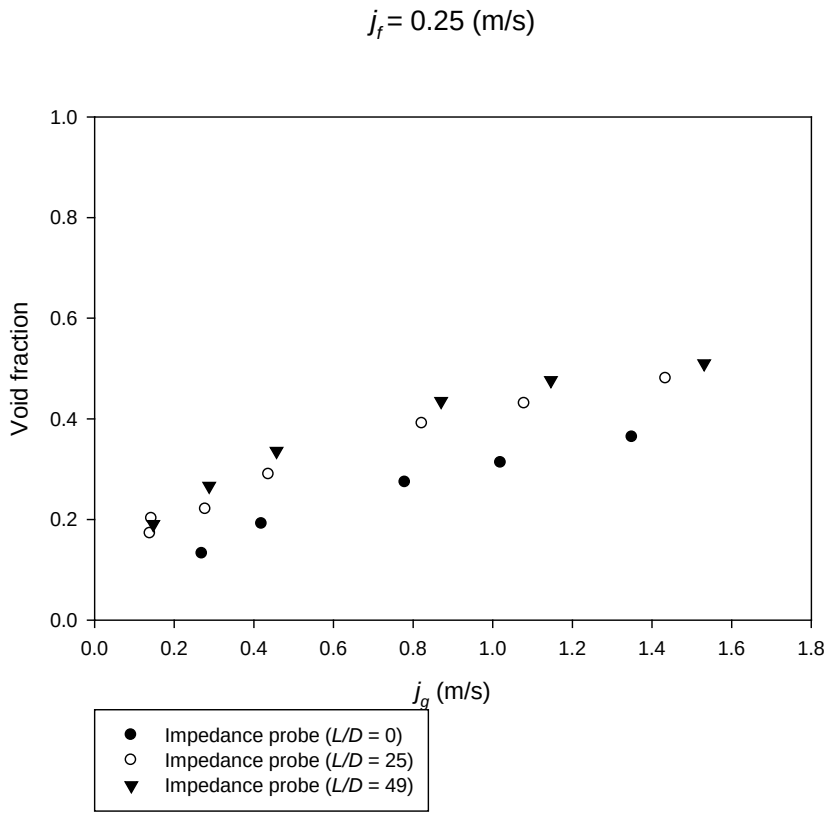

Figure 17: Void fraction vs. j_g when j_f = 0.25 m/s.

As is seen above in Figure 17 for the impedance probes at all three axial positions the void fraction increases as j_g increases. This is expected, because as j_g increase the area of the air would increase relative to the total area. As a general trend, when *L/D* increases the void fraction increases. The reason for this is that the pressure is smaller near the outlet of the test section so the air expands more at larger values of *L/D*.

To determine if the impedance probe could detect the difference in flow regimes normalized impedance signals were found that model the bubbly, slug, and churn flow regimes. An example of an impedance signal for the bubbly flow regime was found at a point of j_g = 0.14 m/s and j_f = 0.25 m/s. This point correlates to what is observed in the image of the inlet flow conditions and in the mean and standard deviation of the impedance signals. The normalized impedance signals for bubble flow are shown in Figures 18, 19, and 20 for impedance probe 1 (*L/D* = 0), impedance probe 2 (*L/D* = 25), and impedance probe 3 (*L/D* = 49) respectively. For all three impedance probes the mean signal is near an impedance value of 0.8 with small fluctuations around the mean. This is consistent with the definition of bubbly flow defined in Section 1.1, because of the continuous liquid and evenly dispersed bubbles.

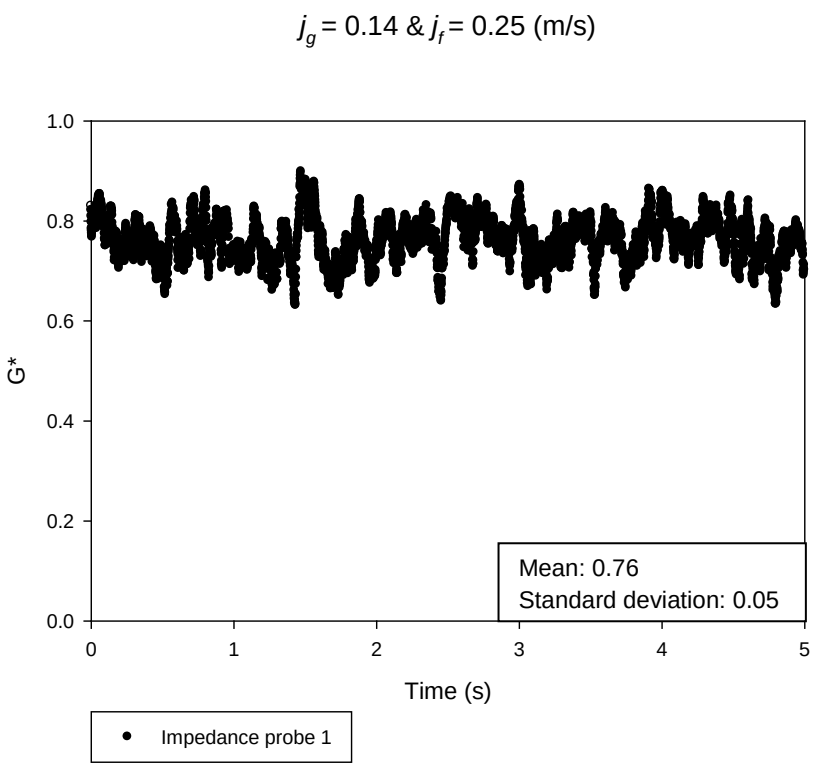

Figure 18: Example of the normalized impedance signal for bubbly flow at *L/D* = 0 and j_f = 0.25 m/s.

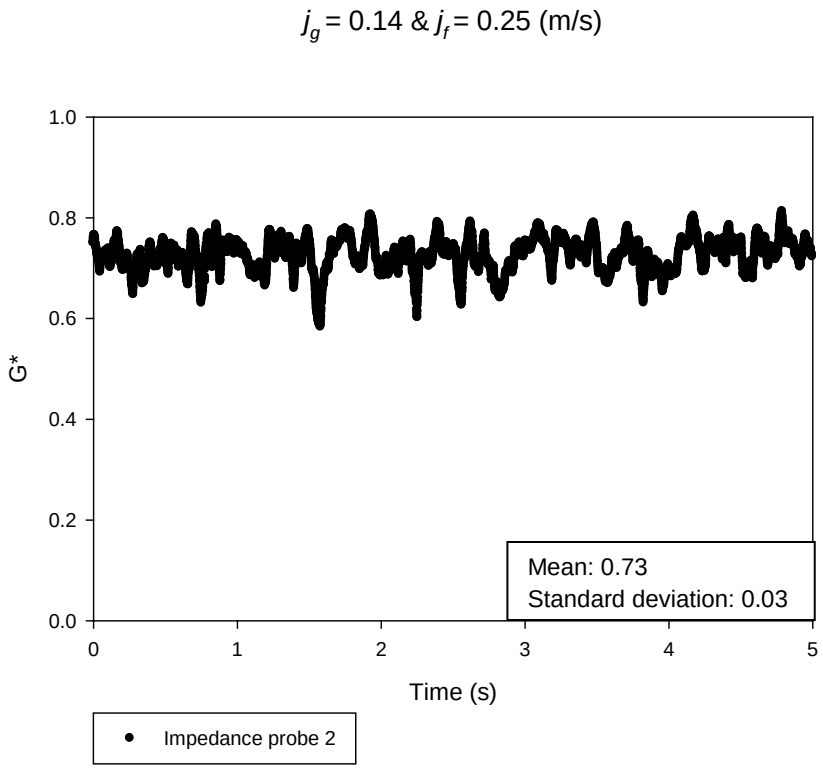

Figure 19: Example of the normalized impedance signal for bubbly flow at *L/D* = 25 and j_f = 0.25 m/s.

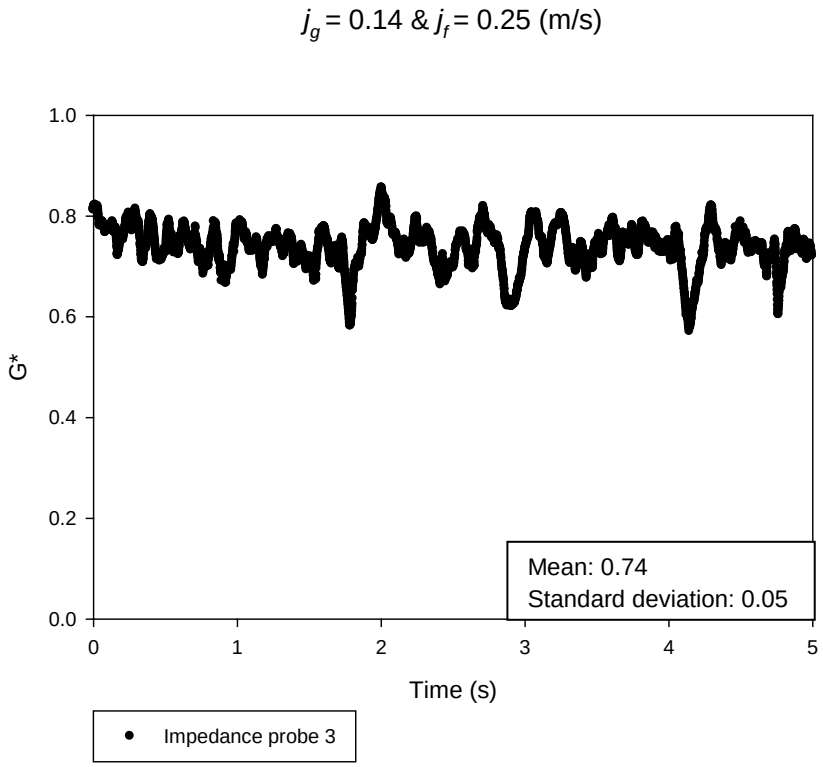

Figure 20: Example of the normalized impedance signal for bubbly flow at *L/D* = 49 and j_f = 0.25 m/s.

An example of an impedance signal for the slug flow regime was found at an inlet condition of j_g = 0.27 m/s and j_f = 0.25 m/s. This point correlates to what is observed in the image of the inlet flow conditions and in the mean and standard deviation of the impedance signals that the flow regime is either slug flow or churn flow. The normalized impedance signals for slug flow are shown in Figures 21, 22, and 23 for impedance probe 1 (*L/D* = 0), impedance probe 2 (*L/D* = 25), and impedance probe 3 (*L/D* = 49) respectively. For impedance probe 1, the signal has very large oscillations that correspond to large bubbles passing between the electrodes of the impedance void meter. An observation that is made for the signal from impedance probe 1 is that the normalized impedance is above 1 at different points, this should not be possible. A reason for this could be imperfections in the circuit of the impedance void meter. Impedance probe 2 has a more defined oscillation between the annular flow conditions and bubbly flow, which occurs because the some of the bubbles that were seen in the probe 1, have coalesced into larger/more defined slug bubbles. This pattern continues for impedance probe 3, as the time between the peaks and the peaks themselves become further apart. This indicates that the slug bubbles have further developed between probes 2 and 3. These well defined oscillations between bubble flow and annular are characteristic of the slug flow regime, for this reason it was determined that the impedance probes could detect slug flow.

j_g = 0.27 & j_f = 0.25 (m/s)

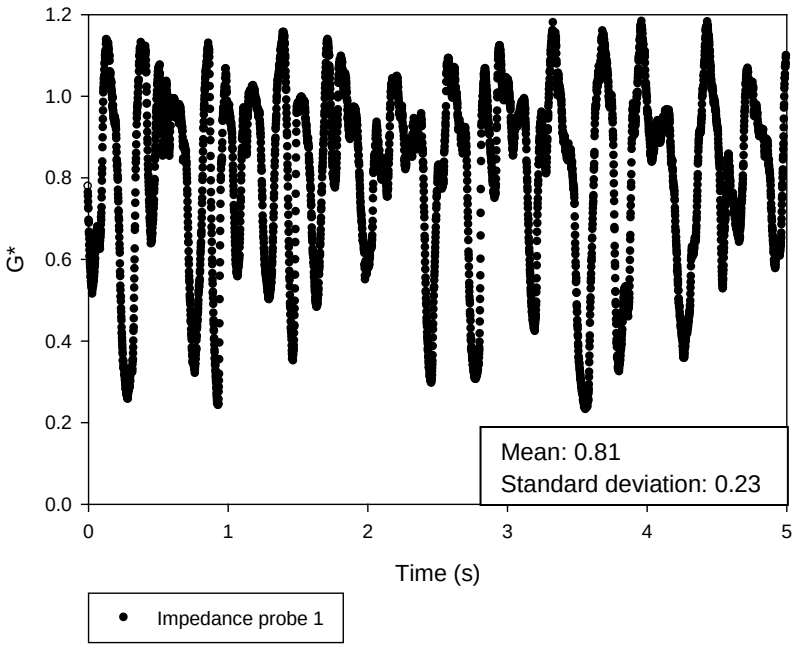

Figure 21: Example of the normalized impedance signal for slug flow at *L/D* = 0 and j_f = 0.25 m/s.

j_g = 0.28 & j_f = 0.25 (m/s)

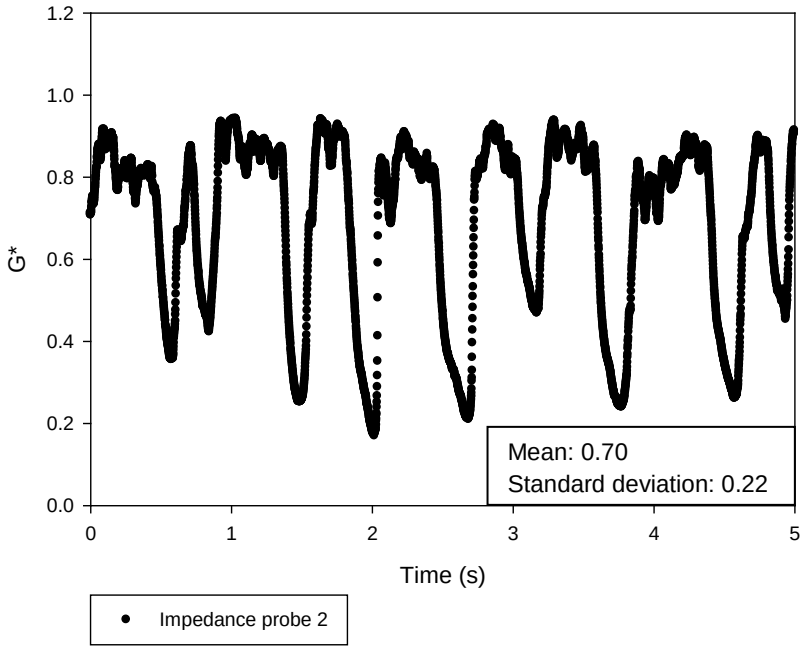

Figure 22: Example of the normalized impedance signal for slug flow at *L/D* = 25 and j_f = 0.25 m/s.

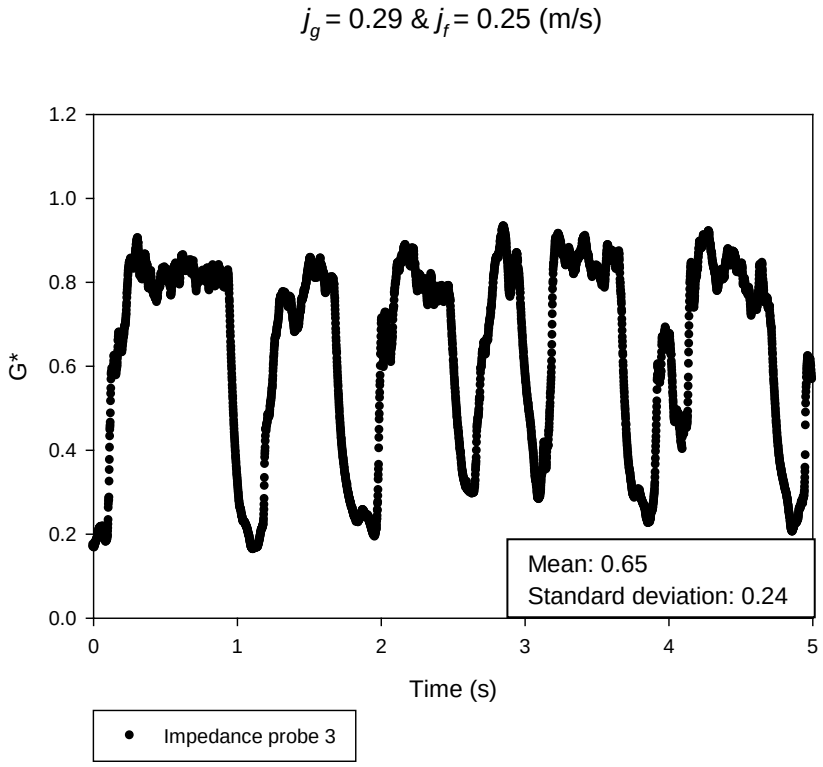

Figure 23: Example of the normalized impedance signal for slug flow at *L/D* = 49 and j_f = 0.25 m/s.

An example of an impedance signal for the churn flow regime was found at an inlet condition of j_g = 1.35 m/s and j_f = 0.25 m/s. This point correlates to what is observed in the image of the inlet flow conditions and in the mean and standard deviation of the impedance signals that the flow regime is either slug flow or churn flow. The normalized impedance signals for churn flow are shown in Figures 24, 25, and 26 for impedance probe 1 (*L/D* = 0), impedance probe 2 (*L/D* = 25), and impedance probe 3 (*L/D* = 49) respectively. Impedance probe 1 is similar to what was observed in the slug flow case so the differentiating factor between the previous slug flow case and this test point is found by looking at impedance probes 2 and 3. For both probes the oscillations between high and low impedance is not as well defined for this test point as it was for

the previous point. Meaning that discrete large slug bubbles are not observed as they were when j_g = 0.27 m/s. For this test point it was determined that the flow was in the churn flow regime, because churn flow is much more turbulent than slug flow and the observations for this test point were less defined than the slug flow example.

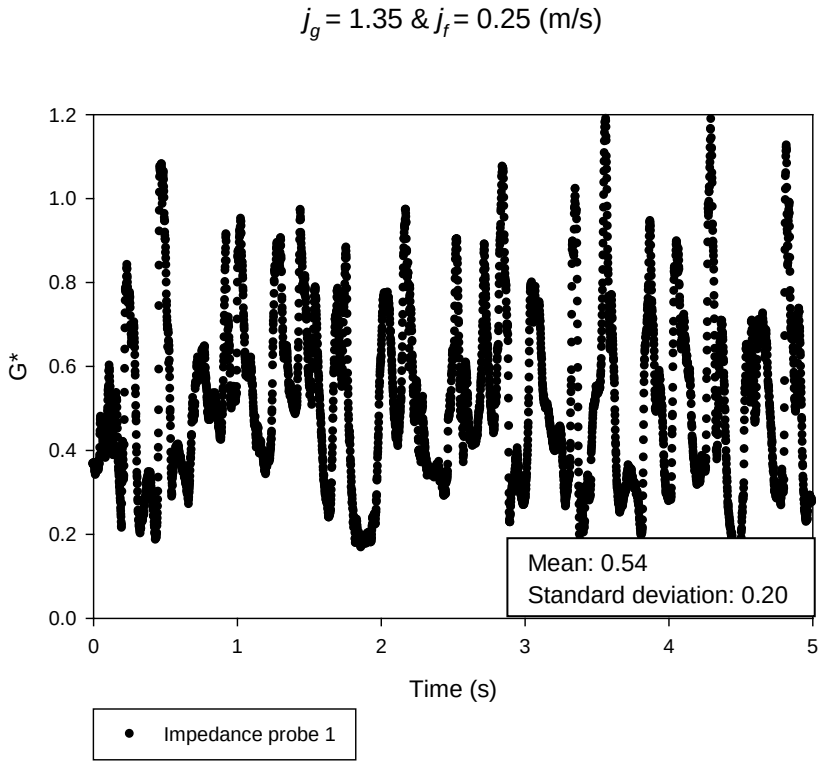

Figure 24: Example of the normalized impedance signal for churn flow at *L/D* = 0 and j_f = 0.25 m/s.

j_g = 1.43 & j_f = 0.25 (m/s)

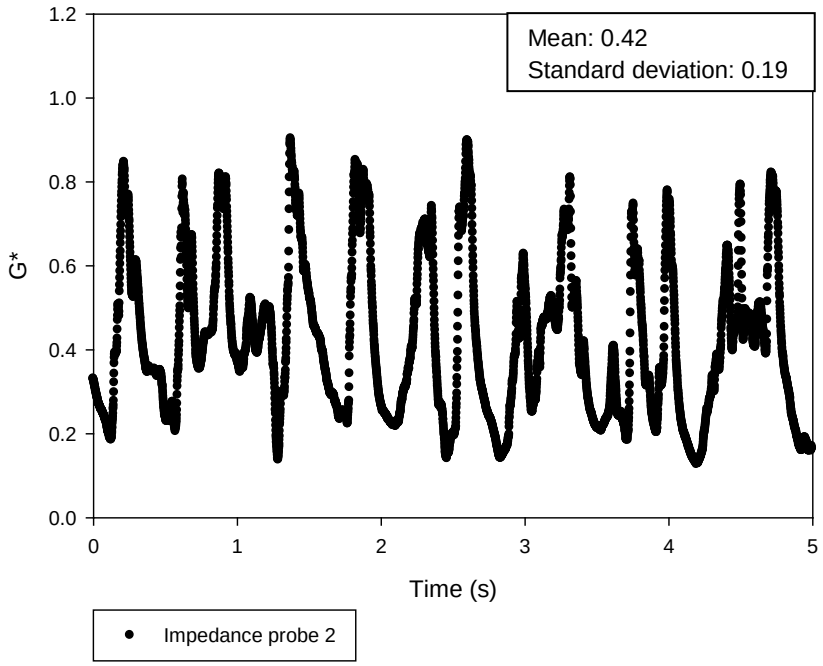

Figure 25: Example of the normalized impedance signal for churn flow at *L/D* = 25 and j_f = 0.25 m/s.

j_g = 1.53 & j_f = 0.25 (m/s)

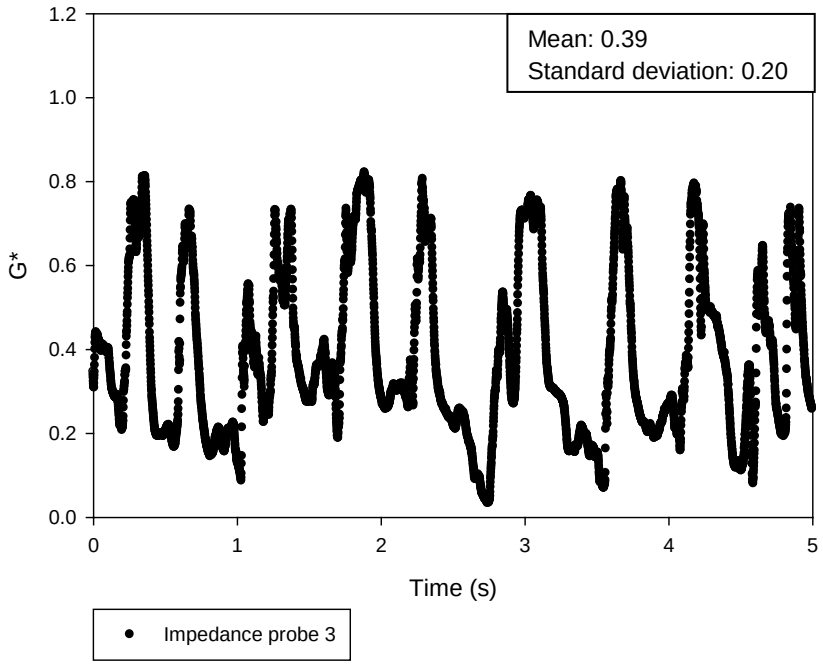

Figure 26: Example of the normalized impedance signal for churn flow at *L/D* = 49 and j_f = 0.25 m/s.

For the test points when j_f = 0.25 m/s bubbly flow, slug flow, and churn flow were observed at inlet j_g's = 0.14, 0.27, and 1.35 m/s respectively. At inlet j_g = 0.14 m/s, bubbly flow was observed, because the standard deviation of the normalized impedance signal was considerably smaller than for the other values of j_g tested and the normalized impedance signal was near 0.8 which indicates that a large amount of water exists relative to water. At inlet j_g = 0.27 m/s, slug flow was observed because the normalized impedance signal showed a steady oscillation between a low impedance signal (i.e. a large amount of air) and a high impedance signal (i.e. a small amount of air). This correlates to the oscillations between annular flow and bubbly flow and these oscillations are characteristics of slug flow. At inlet j_g = 1.30 m/s, churn flow was observed because similar to the slug flow case there were oscillations between high and low impedance signals. However, for this test point the oscillations were not as steady as the slug flow case which correlates to the more turbulent case of churn flow.

The second set of data that will be analyzed is when j_f = 0.50 m/s. The high-speed video images for the test are shown below in Figure 27. The j_g's defined for the images are the inlet air superficial velocities.

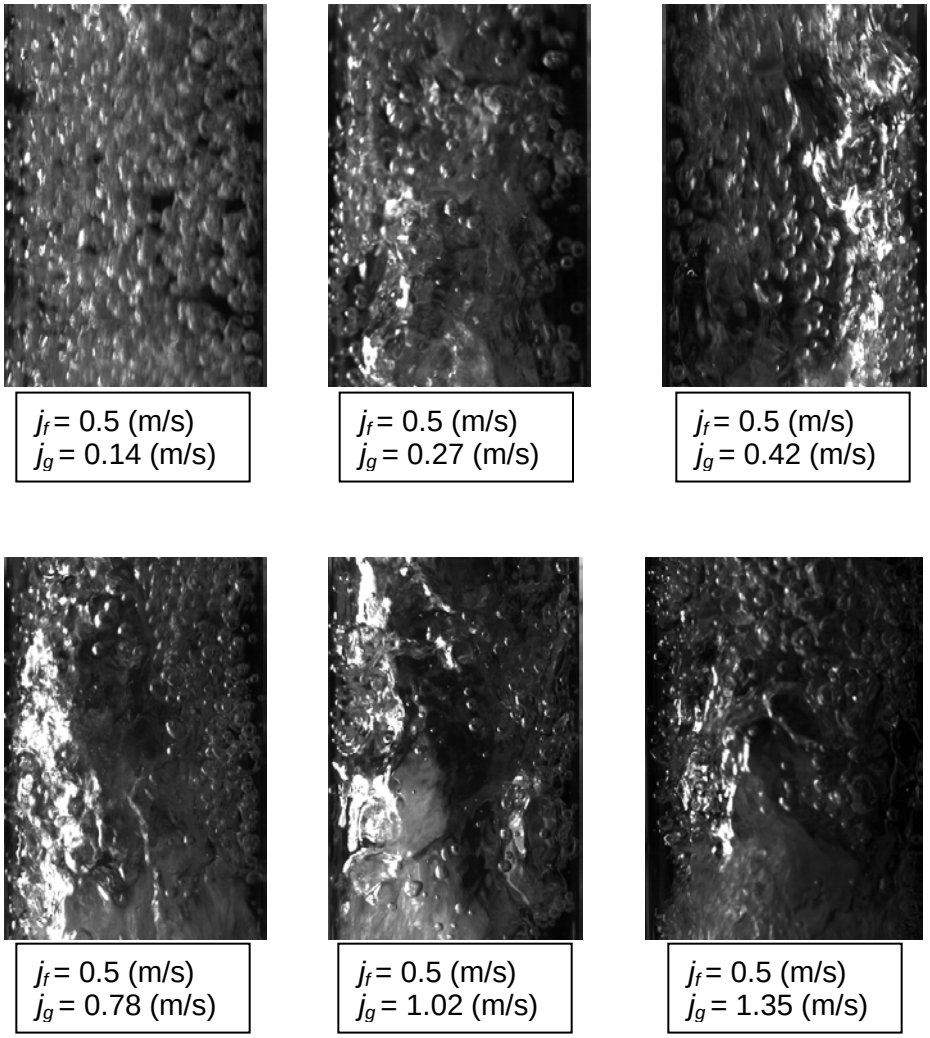

Figure 27: High-speed images of the inlet flow conditions for j_f = 0.5 m/s.

The images show that as the superficial gas velocity increases the bubble size increases and the flow becomes more turbulent. This is expected because from Figure 13 as j_g increases while holding j_f constant the flow regime changes from bubbly to slug and then from slug to churn.

For the impedance probe data, the average and standard deviation were again plotted as a function of j_g. As before the values of j_g are the local superficial air velocities that are calculated using Equation 8 for all of the impedance measurements. For all three

axial positions the standard deviation at the inlet point j_g = 0.14 m/s are considerably smaller than the standard deviations for larger values of j_g. This indicates that when the inlet j_g = 0.14 m/s the flow is in the bubbly flow regime, and for the other values of j_g the flow is either in the slug or churn flow regime. From Figure 28 there does not appear to be a distinguishing feature to differentiate between slug and churn flow. However, the normalized impedance signal in an attempt to determine if the difference between slug and churn flow regimes can be observed for j_f = 0.5 m/s.

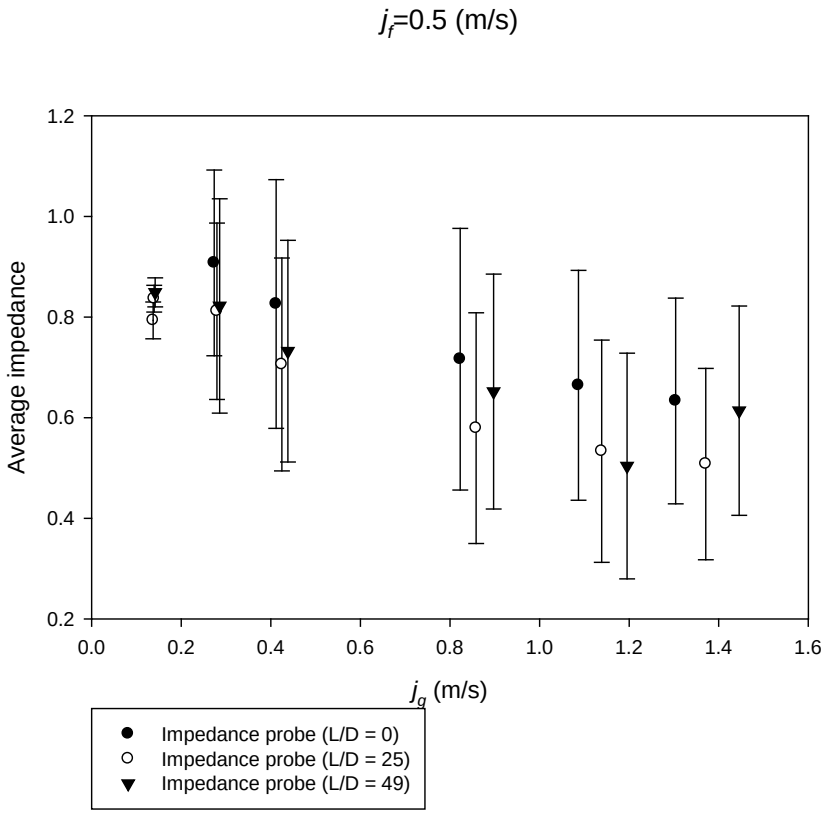

Figure 28: Average and standard deviation of the impedance signals when j_f = 0.5 m/s.

The average impedance values for each of test points when j_f = 0.5 m/s, were used to calculate the void fraction using Equation 20. Equation 20 makes the assumption that

the void fraction distribution is uniform, so the calculated values of the void fraction are approximate values.

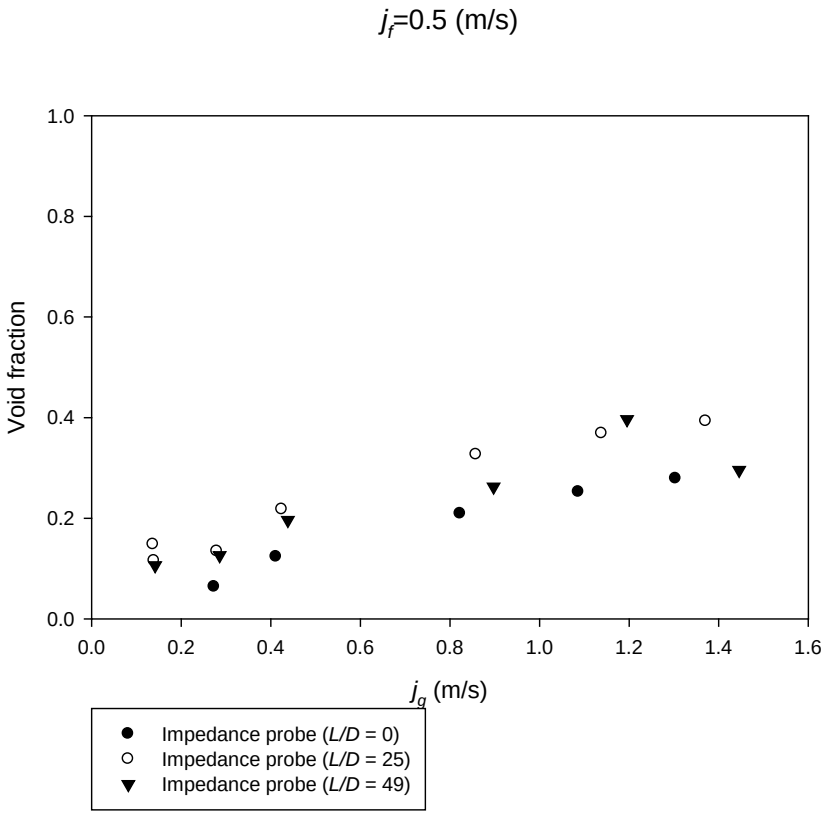

Figure 29: Void fraction vs. j_g when j_f = 0.5 m/s.

The void fraction increases with increasing j_g , which is expected because as the air flow rate increases the area occupied by air should increase relative to the total area. However the general trend that as *L/D* increases the void fraction increases is not visible for these tests points where j_f = 0.5 m/s as it was when j_f = 0.25 m/s. A possible reason for this is that the electrical circuit could have some imperfections that give an inaccurate measurement.

Normalized signals were found when j_f = 0.5 m/s that model the bubbly, slug, and churn flow regimes. An example of an impedance signal for the bubbly flow regime was found

at an inlet point of j_g = 0.14 m/s. This point correlates to what is observed in the image of the inlet flow conditions and in the mean and standard deviation of the impedance signals. The normalized impedance signals for bubble flow are shown in Figures 30, 31, and 32 for impedance probe 1 (*L/D* = 0), impedance probe 2 (*L/D* = 25), and impedance probe 3 (*L/D* = 49) respectively. For all three impedance probes the average signal is near an impedance value of 0.8 with small fluctuations around the mean. This is an example of bubbly flow, because the relatively high average signal correlates to water being in contact with the probes and the small fluctuations correlate to small bubbles being between the probes. This is consistent with the description of bubbly flow in Section 1.1.

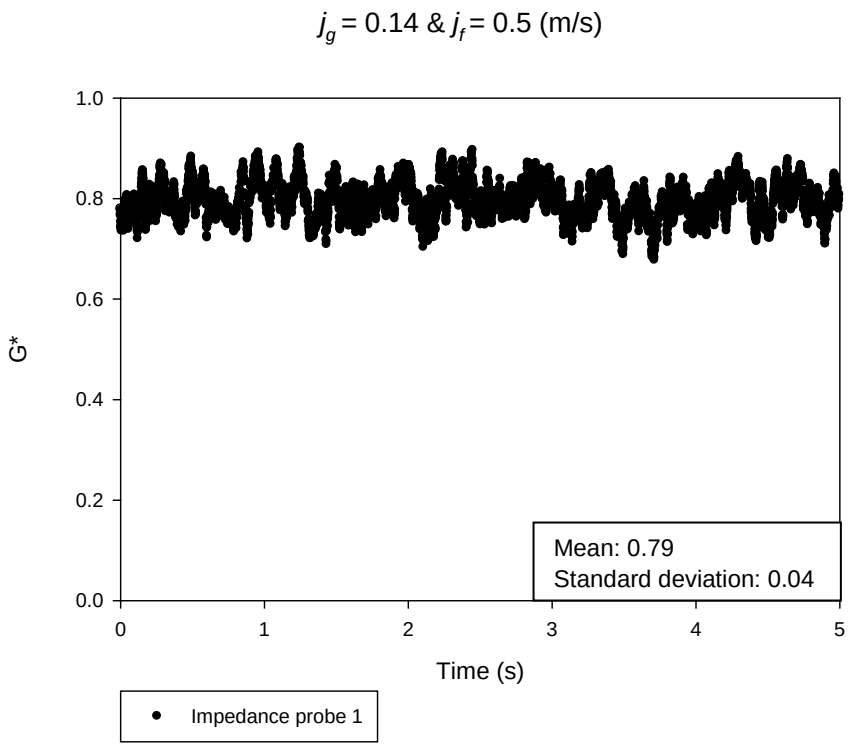

Figure 30: Example of the normalized impedance signal for bubbly flow at *L/D* = 0 and j_f = 0.5 m/s.

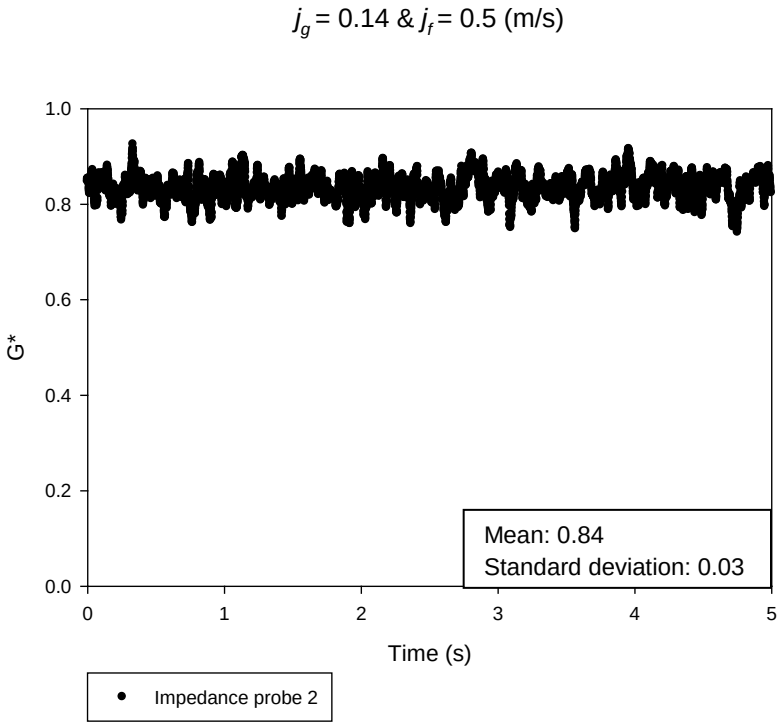

Figure 31: Example of the normalized impedance signal for bubbly flow at *L/D* = 25 and j_f = 0.5 m/s.

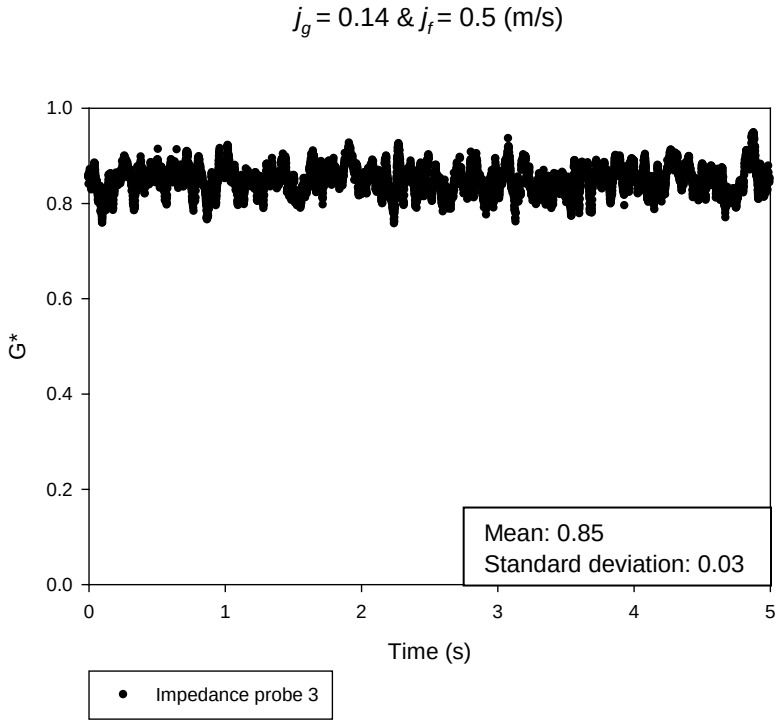

Figure 32: Example of the normalized impedance signal for bubbly flow at *L/D* = 49 and j_f = 0.5 m/s.

Data from the four-sensor conductivity probe was also recorded for the test points when j_f = 0.5 m/s. In the Figures 33, 34, and 35 below the void fraction, average bubble velocity, and Sauter mean bubble diameter are shown as a function of radial position. The void fraction is approximately constant as the radial position changes. The fact that the void fraction is low and it is approximately constant leads to the conclusion that this test point is in the bubble flow regime. This is the same conclusion that was reached when the signals from the impedance probes were examined. The average bubble velocity decreases as the radial position increases, the reason for this is that near the wall friction forces exist to restrict the flow, thereby decreasing the velocity. The Sauter mean bubble diameter for group I bubbles remains approximately constant across the radius examined, and this is consistent with the literature findings (Kim et al., 2000). For the investigated flow conditions group II bubbles did not exist, which also lead to the conclusion that this test point resides in the bubbly flow regime.

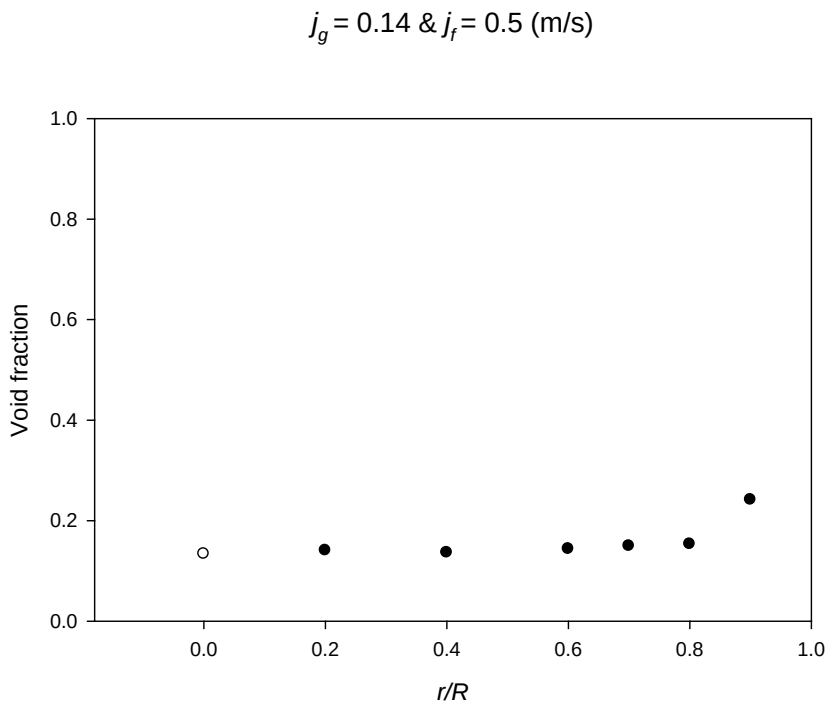

Figure 33: Radial void fraction distribution for j_g = 0.14 m/s & j_f = 0.5 m/s.

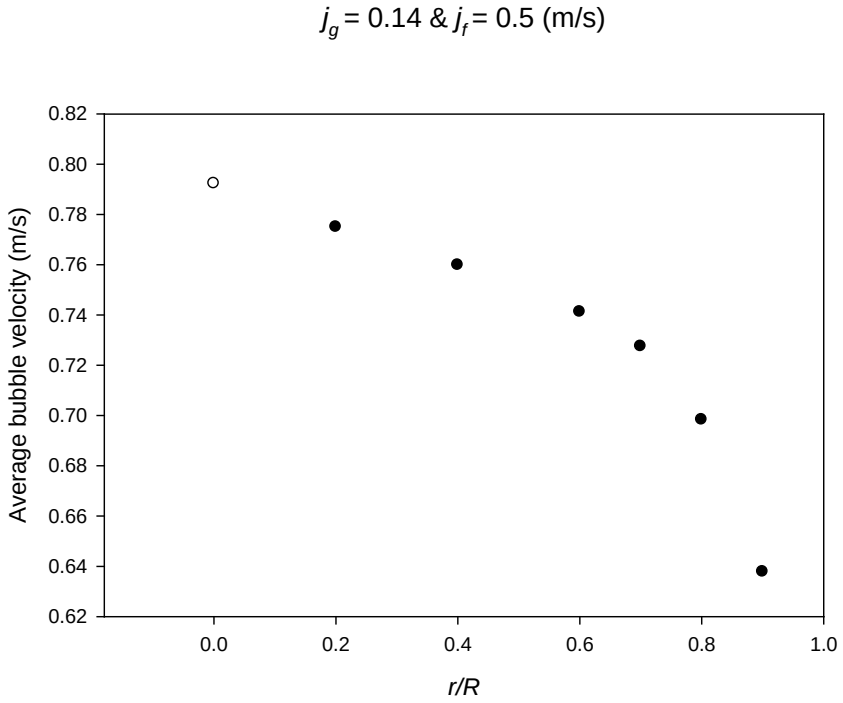

Figure 34: Radial average bubble velocity distribution for j_g = 0.14 m/s & j_f = 0.5 m/s.

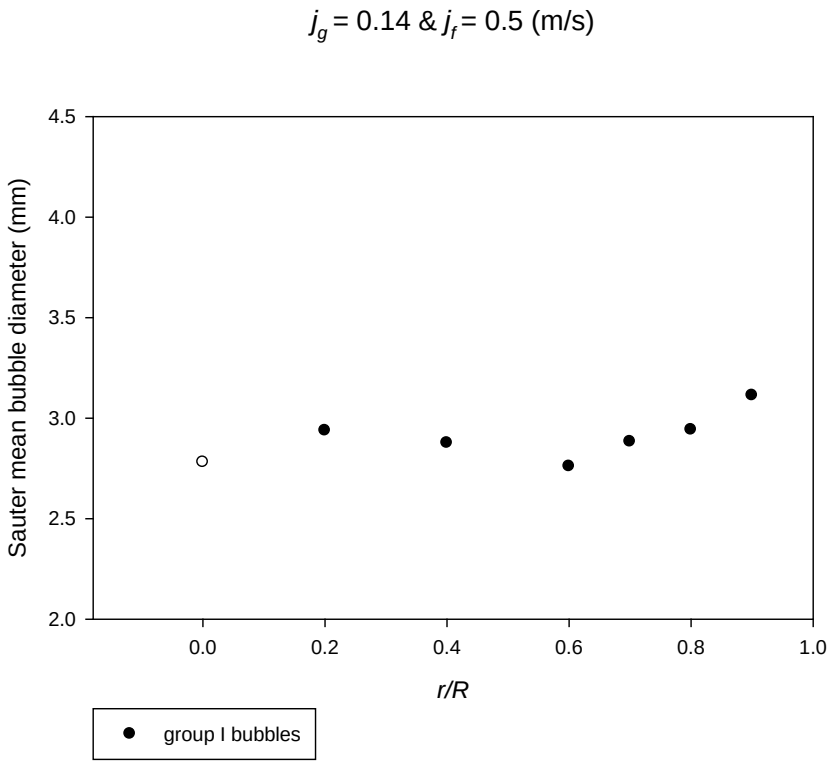

Figure 35: Radial Sauter mean bubble diameter distribution for group I bubbles at j_g = 0.14 m/s & j_f = 0.5 m/s.

An example of an impedance signal for the slug flow regime was found at an inlet condition of j_g = 0.27 m/s. This point correlates to what is observed in the image of the inlet flow conditions and in the mean and standard deviation of the impedance signals that the flow regime is either slug flow or churn flow. The normalized impedance signals for slug flow are shown in Figures 36, 37, and 38 for impedance probe 1 (*L/D* = 0), impedance probe 2 (*L/D* = 25), and impedance probe 3 (*L/D* = 49) respectively. For impedance probe 1, the signal has very large oscillations that correspond to large bubbles passing between the electrodes of the impedance void meter. Impedance probe 2 still has large fluctuations, but is more organized than the impedance signal observed from probe 1. Impedance probe 3 has maintained the large fluctuations and has better defined oscillations between bubbly and annular flow regimes. This indicates

that the slug bubbles have further developed between probes 2 and 3. These well defined oscillations between bubbly flow and annular flow are characteristics of the slug flow regime. This led to the conclusion that this test point is in the slug flow regime.

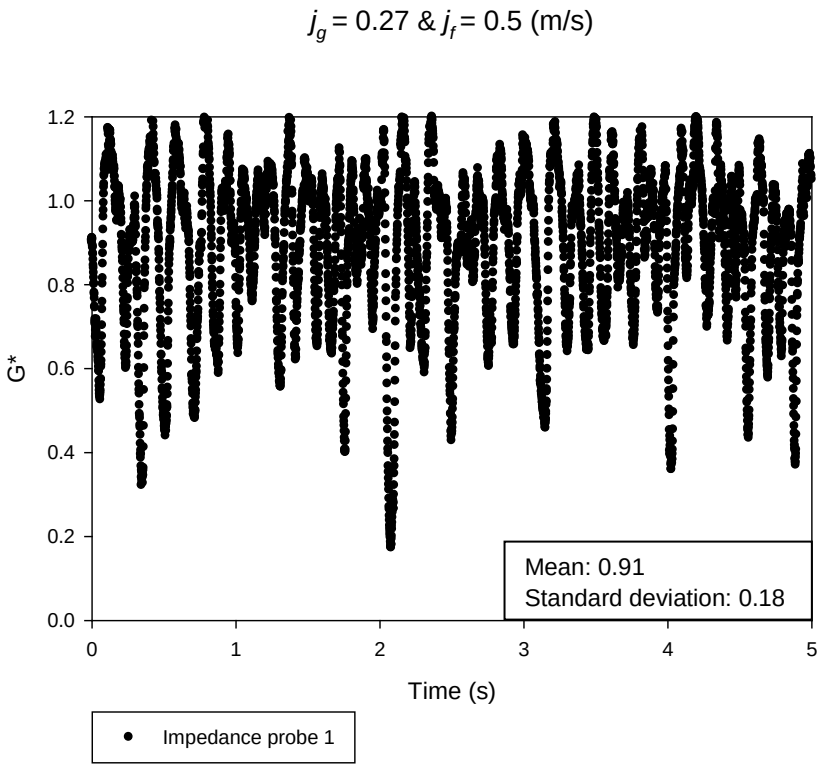

Figure 36: Example of the normalized impedance signal for slug flow at *L/D* = 0 and j_f = 0.5 m/s.

j_g = 0.28 & j_f = 0.5 (m/s)

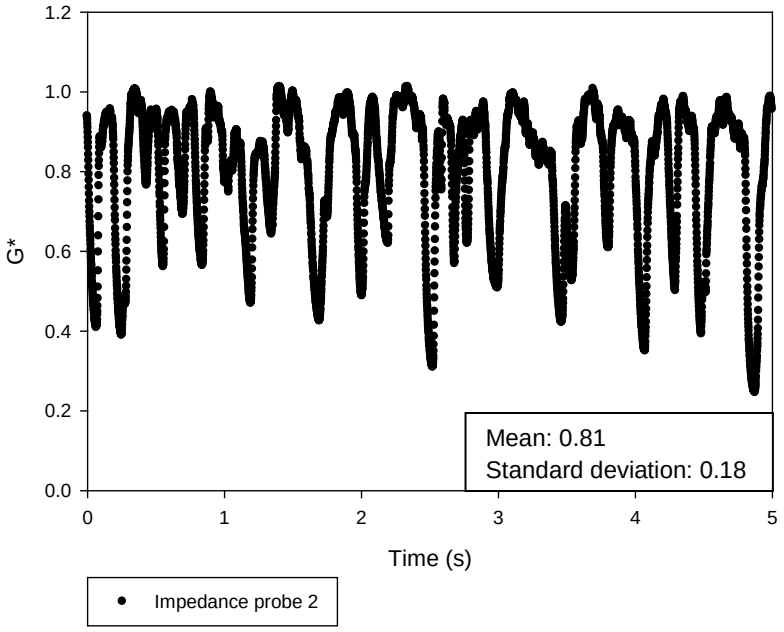

Figure 37: Example of the normalized impedance signal for slug flow at *L/D* = 25 and j_f = 0.5 m/s.

j_g = 0.29 & j_f = 0.5 (m/s)

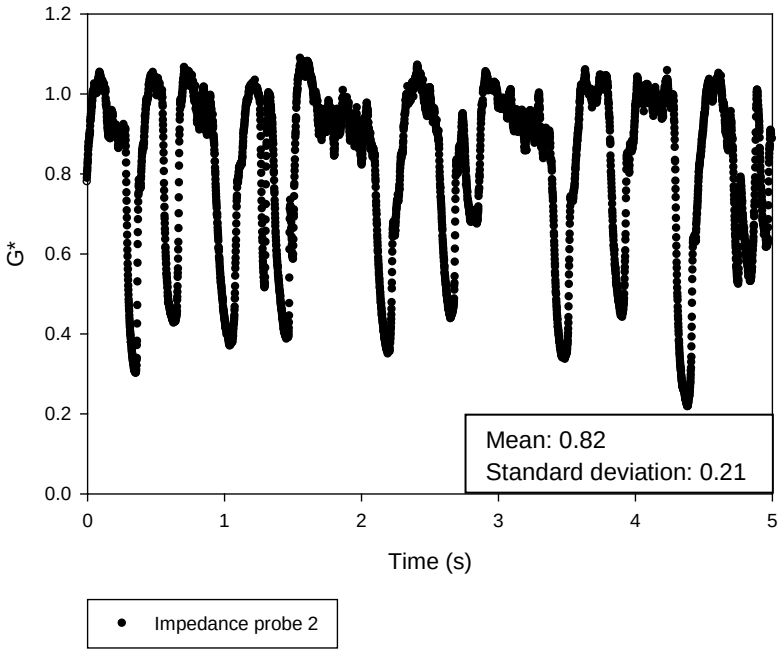

Figure 38: Example of the normalized impedance signal for slug flow at *L/D* = 49 and j_f = 0.5 m/s.

In the Figures 39, 40, 41, and 42 the void fraction, average bubble velocity, and Sauter mean bubble diameter for group I and II bubbles are shown as functions of radial position. The void fraction decreases as the radial position increases. The reason for this is group II bubbles exist in this test point. Group II bubbles are generally more heavily concentrated near the center of the pipe and these bubbles have large areas so when they are present the void fraction will be considerable higher than when only group I bubbles are present. This is what occurs as the wall is approached, fewer group II bubbles are present so the void fraction is dominated by the smaller group I bubbles which causes the void fraction to decrease. The presence of these group II bubbles leads to the conclusion that this test point is either slug flow or churn flow. It is not possible at this time to tell the difference between slug and churn flow with the four-sensor conductivity probe, because the oscillations look similar for both test points. The average bubble velocity decreases as the radial position increases, the reason for this is that near the wall friction forces exist to restrict the flow, thereby decreasing the velocity. The Sauter mean bubble diameter for group I bubbles increases slightly as the radius increases. This is inconsistent with the literature (Kim et al., 2000), the reason for this is that the void fraction of the group I bubbles increase relative to the interfacial area concentration as the radius increases. The Sauter mean bubble diameter for group II bubbles decreases as the radius increases, which is expected because group II bubbles are more concentrated near the center of the pipe.

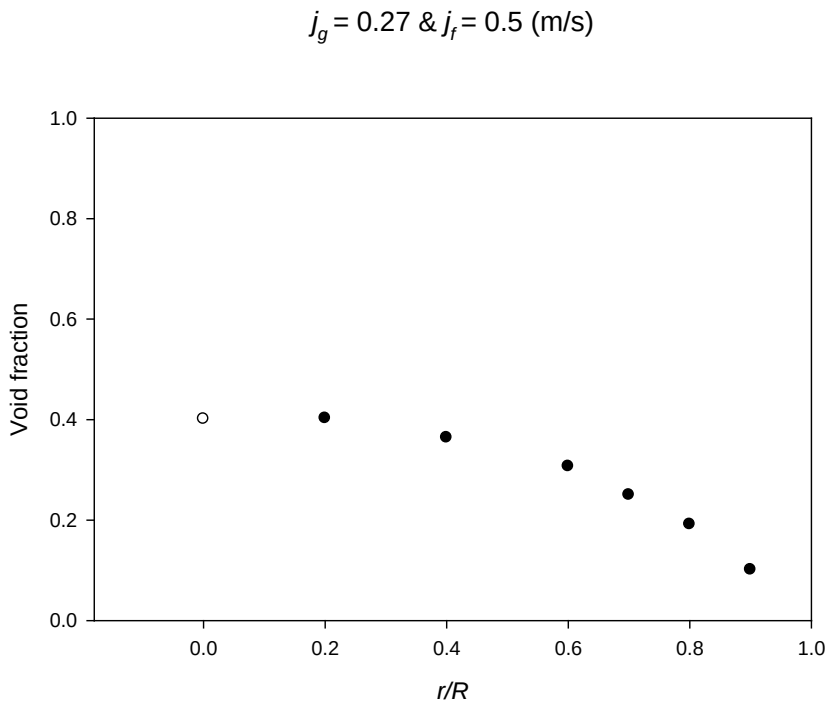

Figure 39: Radial void fraction distribution for j_g = 0.27 m/s & j_f = 0.5 m/s.

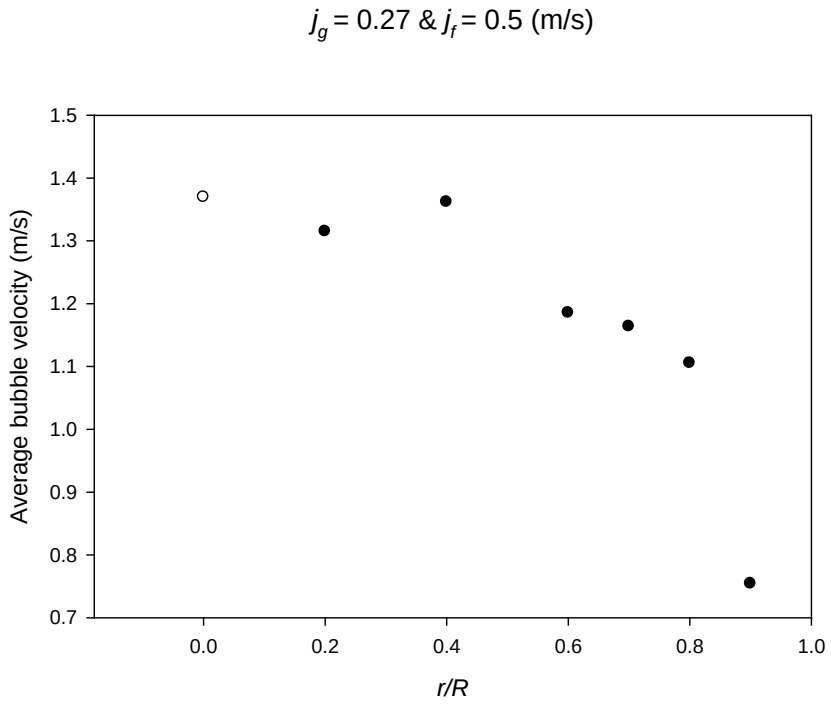

Figure 40: Radial average bubble velocity distribution for j_g = 0.27 m/s & j_f = 0.5 m/s.

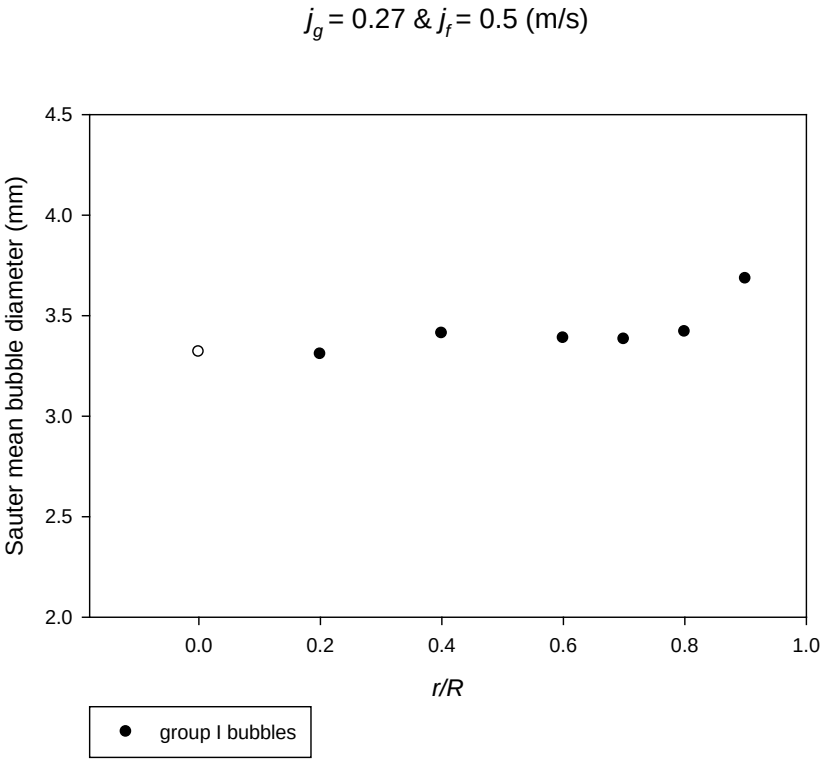

Figure 41: Radial Sauter mean bubble diameter distribution for group I bubbles at j_g = 0.27 m/s & j_f = 0.5 m/s.

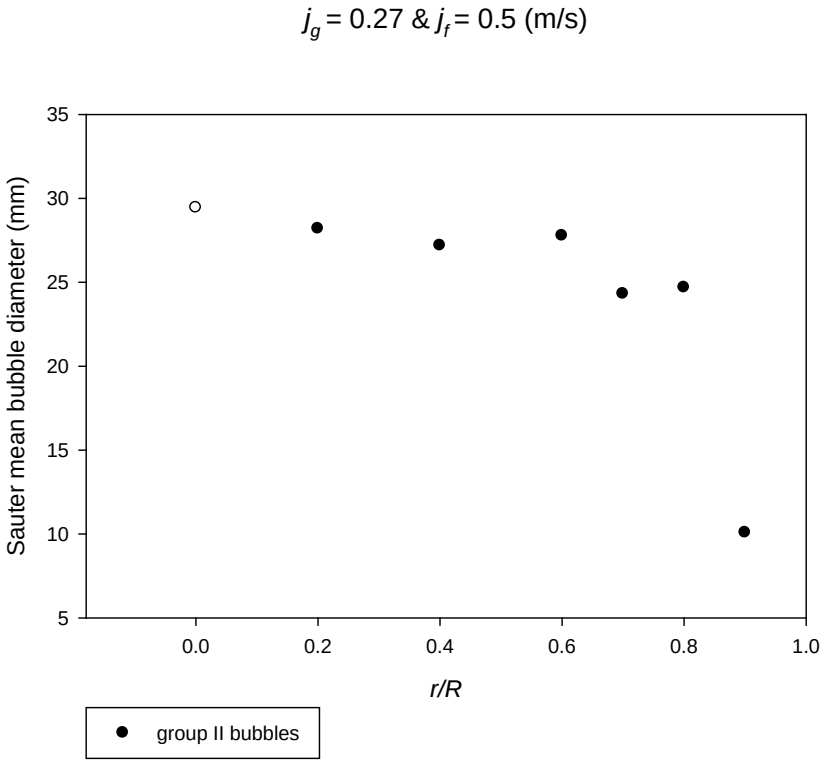

Figure 42: Radial Sauter mean bubble diameter distribution for group II bubbles at j_g = 0.27 m/s & j_f = 0.5 m/s.

An example of an impedance signal for the churn flow regime was found at an inlet condition of j_g = 1.35 m/s and j_f = 0.25 m/s. This point correlates to what is observed in the image of the inlet flow conditions and in the mean and standard deviation of the impedance signals that the flow regime is either slug flow or churn flow. The normalized impedance signals for churn flow are shown in Figures 43, 44, and 45 for impedance probe 1 (*L/D* = 0), impedance probe 2 (*L/D* = 25), and impedance probe 3 (*L/D* = 49) respectively. Impedance probe 1 is similar to what was observed in the slug flow case so the differentiating factor between the previous slug flow case and this test point is found by looking at impedance probes 2 and 3. For both probes the oscillations between high and low impedance is not as defined for this test point as it was for the previous point. It was determined that since churn flow is much more turbulent than slug flow, that this test point is an example of churn flow.

j_g = 1.30 & j_f = 0.5 (m/s)

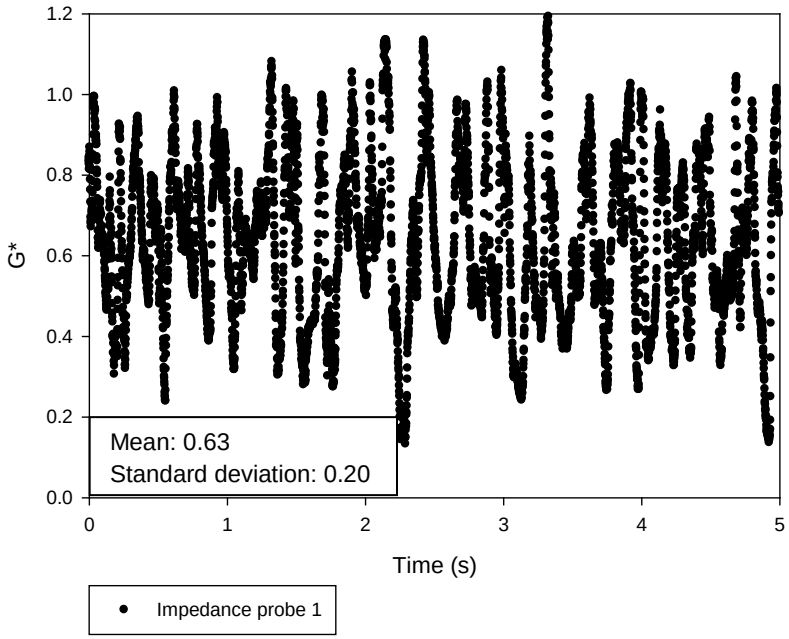

Figure 43: Example of the normalized impedance signal for churn flow at *L/D* = 0 and j_f = 0.5 m/s.

j_g = 1.37 & j_f = 0.5 (m/s)

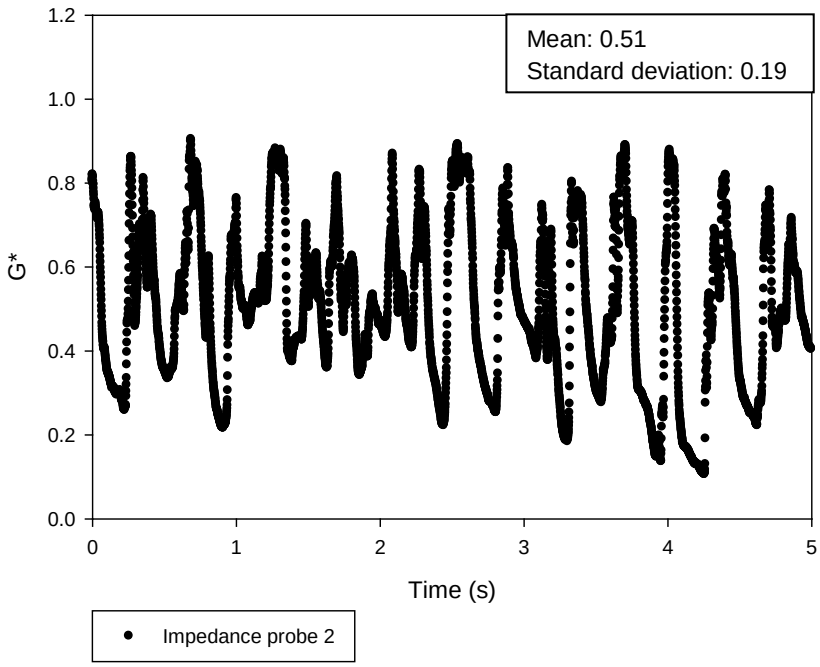

Figure 44: Example of the normalized impedance signal for churn flow at *L/D* = 0 and j_f = 0.5 m/s.

j_g = 1.44 & j_f = 0.5 (m/s)

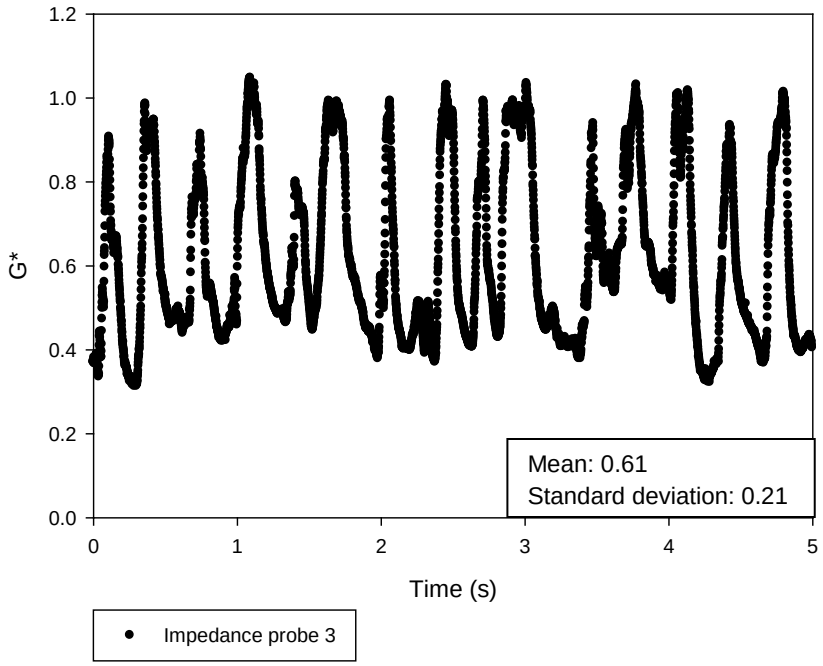

Figure 45: Example of the normalized impedance signal for churn flow at *L/D* = 0 and j_f = 0.5 m/s.

In the Figures 46, 47, 48, and 49 the void fraction, average bubble velocity, and Sauter mean bubble diameter for group I and II bubbles are shown as functions of radial position. The void fraction and average bubble velocity profiles are very similar to what they were for the previous test point. The only difference being in the magnitude of the void fraction and average bubble velocity for this reason it is determined that the four-sensor conductivity probe is not able to differentiate between slug and churn flows. The Sauter mean bubble diameter for group I bubbles remains approximately constant as the radius increases, which is consistent with the literature (Kim et al., 2000). The Sauter mean bubble diameter for group II bubbles decreases as the radius increases, which is expected because group II bubbles are more concentrated near the center of the pipe.

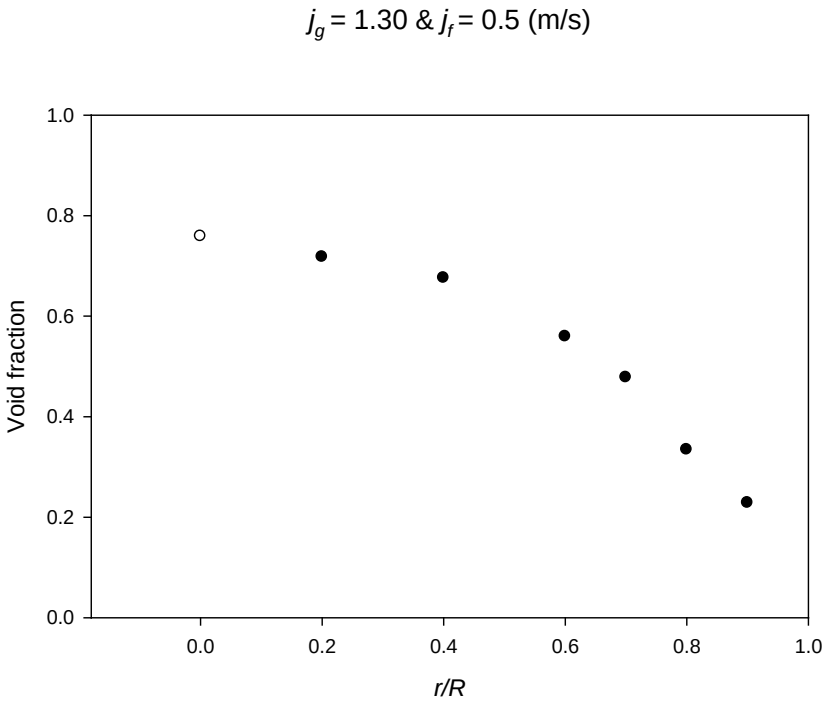

Figure 46: Radial void fraction distribution for j_g = 1.30 m/s & j_f = 0.5 m/s.

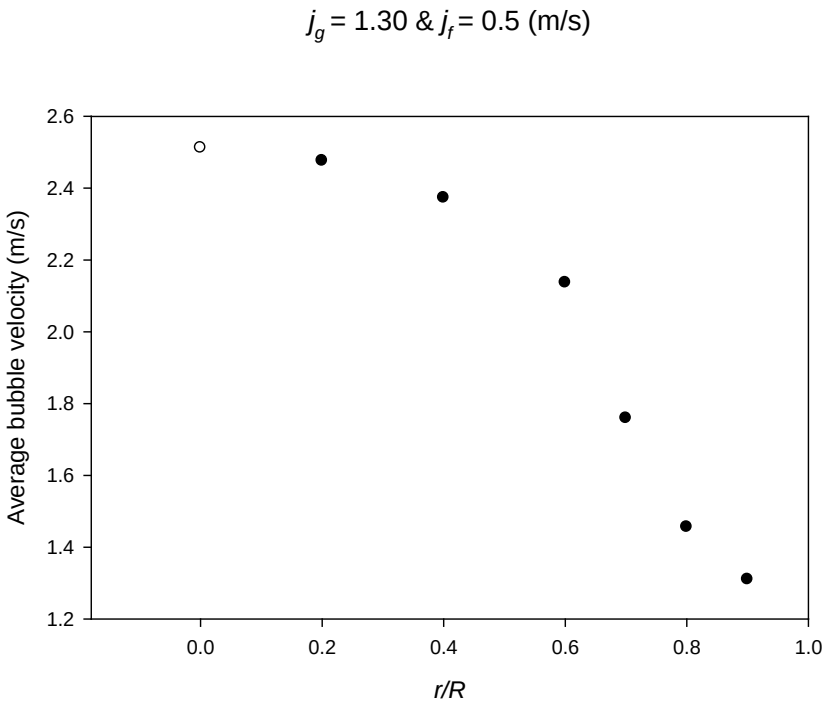

Figure 47: Radial average bubble velocity distribution for j_g = 1.30 m/s & j_f = 0.5 m/s.

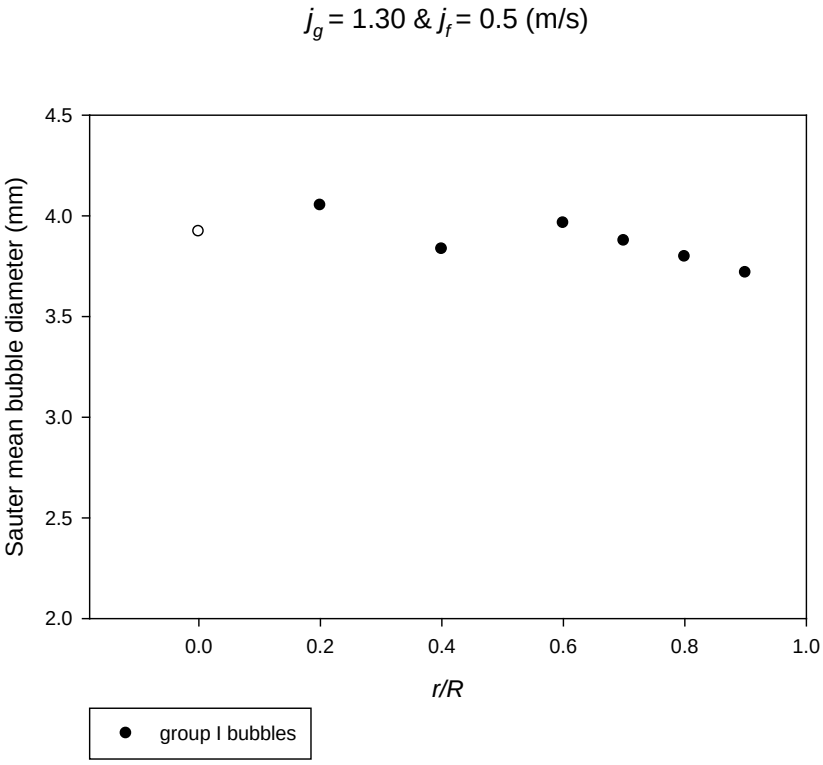

Figure 48: Radial Sauter mean bubble diameter distribution for group I bubbles at j_g = 1.30 m/s & j_f = 0.5 m/s.

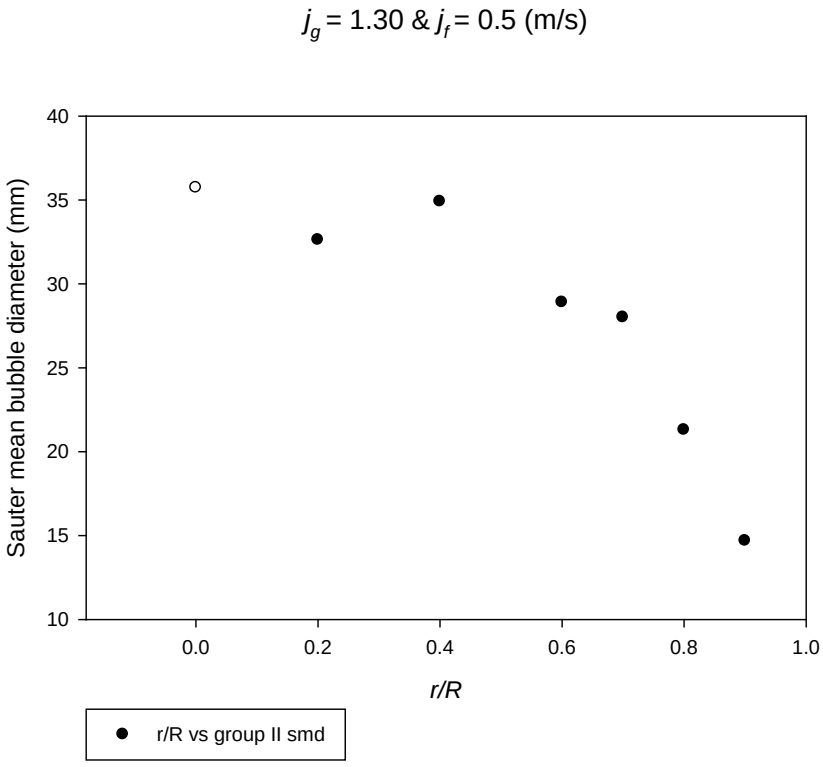

Figure 49: Radial Sauter mean bubble diameter distribution for group II bubbles at j_g = 1.30 m/s & j_f = 0.5 m/s.

For the test points when j_f = 0.5 m/s bubbly flow, slug flow, and churn flow were observed at inlet j_g's = 0.14, 0.27, and 1.30 m/s respectively. At inlet j_g = 0.14 m/s, bubbly flow was observed, because the standard deviation of the normalized impedance signal was considerably smaller than for the other values of j_g tested and the normalized impedance signal was near 0.8 which indicates that a large amount of water exists relative to water. Also the four-sensor conductivity probe did not detect any group II bubbles for this test point and the void fraction was approximately constant across the test section. At an inlet j_g = 0.27 m/s, slug flow was observed because the normalized impedance signal showed a steady oscillation between a low impedance signal (i.e. a large amount of air) and a high impedance signal (i.e. a small amount of air). This correlates to the oscillations between annular flow and bubbly flow, and these oscillations are characteristics of slug flow. It is important to note that the four-sensor conductivity probe could detect the difference between the bubbly flow regime and the slug/churn flow regimes, but could not detect a difference between the slug flow regime and churn flow regime. At inlet j_g = 1.30 m/s, churn flow was observed because similar to the slug flow case there were oscillations between high and low impedance signals. However, for this test point the oscillations were not as steady as the slug flow case which correlates to the more turbulent case of churn flow.

The third set of data that will be analyzed is when j_f = 1.0 m/s. The high-speed video images for the test are shown below in Figure 50. The j_g's defined for the images are the inlet air superficial velocities.

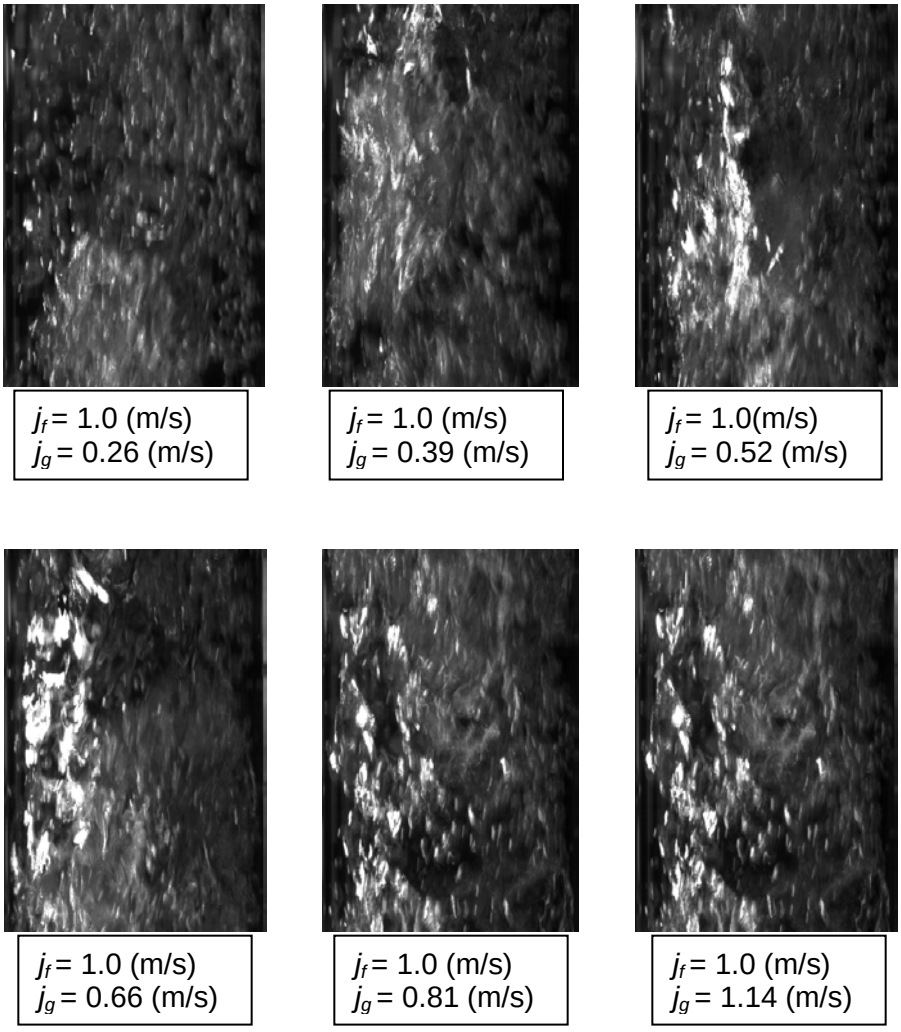

Figure 50: High-speed images of the inlet flow conditions for j_f = 1.0 m/s.

The images show that as the air superficial velocity increases the bubble size increases and the flow becomes more turbulent. This is expected because from Figure 13 as j_g increases while holding j_f constant the flow regime changes from bubbly to slug and then from slug to churn.

For the impedance probe data, the average and standard deviation were plotted as a function of j_g. As before the values of j_g are the local superficial air velocities that are calculated using Equation 8 for all of the impedance measurements. At all three axial

positions the standard deviation at the inlet point j_g = 0.26 m/s are slightly smaller than the standard deviations for larger values of j_g. This standard deviation is larger than what was found for the bubbly flow when j_f = 0.25 and 0.50 m/s. this indicates that for this test point it is in a transition region between bubbly flow and slug flow. From Figure 51 there does not appear to be a distinguishing feature to differentiate between slug and churn flow. However, the normalized impedance signal in an attempt to determine if the difference between slug and churn flow regimes can be observed for j_f = 1.0 m/s.

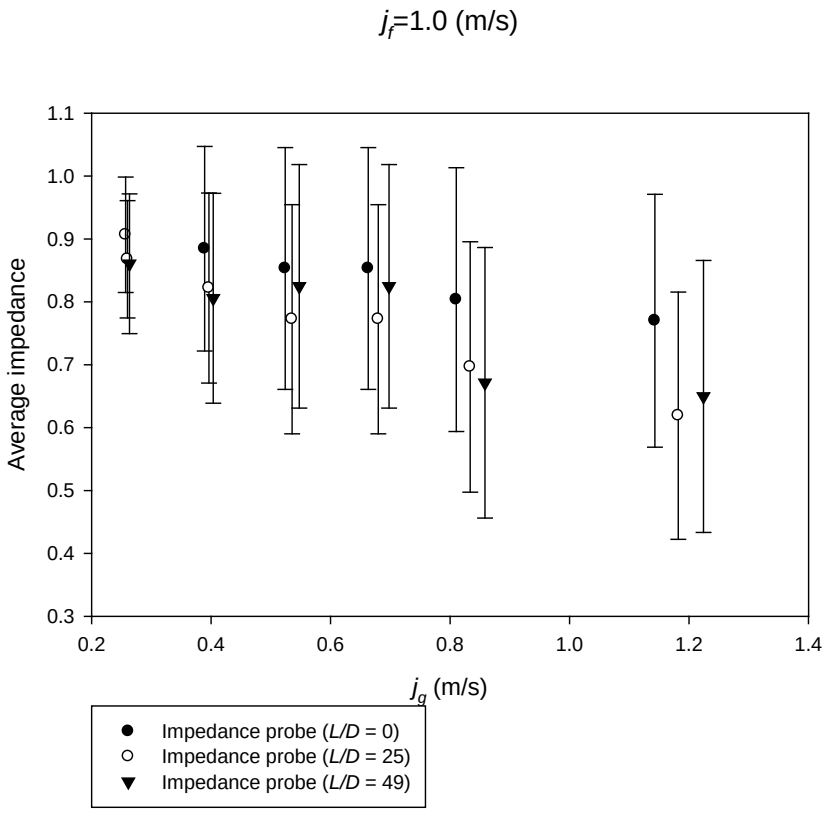

Figure 51: Average and standard deviation of the impedance signals when j_f = 1.0 m/s.

The average impedance values for each of test point when j_f = 1.0 m/s were used to calculate the void fraction using Equation 20. Equation 20 makes the assumption that

the void fraction distribution is uniform, so the calculated values of the void fraction are approximate values.

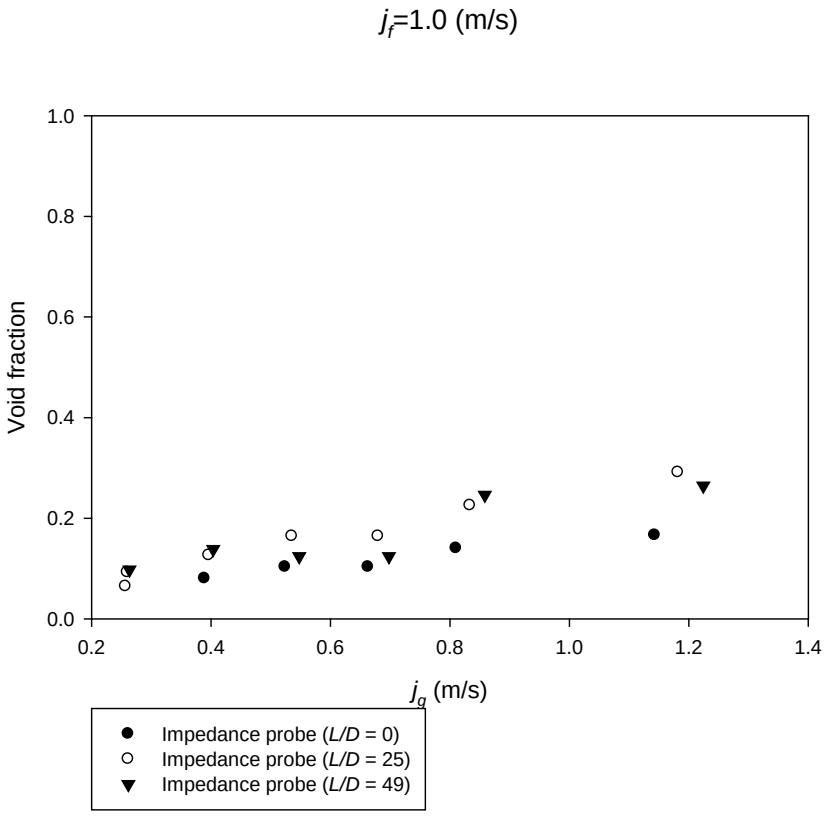

Figure 52: Void fraction vs. j_g when j_f = 1.0 m/s.

As is seen above in Figure 52 for the impedance probes at all three axial positions the void fraction increases as j_g increases. This is expected, because as the flow rate of air increases the area occupied by the air should increase relative to the total flow area. As seen with the test points when j_f = 0.5 m/s a trend is not observed when *L/D* increases as was observed for j_f = 0.25 m/s. A possible reason for this is that the electrical circuit could have some imperfections that give an inaccurate measurement.

Normalized signals were difficult to found for a j_f = 1.0 m/s, that model the bubbly, slug, and churn flow regimes. So test points were chosen nearest to the desired flow regimes

as possible. The test points that were chosen are inlet j_g's = 0.26, 0.52, and 1.14 m/s. The normalized impedance signals for j_g = 0.26 m/s are shown in Figures 53, 54, and 55 for impedance probe 1 (*L/D* = 0), impedance probe 2 (*L/D* = 25), and impedance probe 3 (*L/D* = 49) respectively. For all three impedance probes the average signal is near an impedance value of 0.9 with fluctuations reaching to around an impedance value of 0.6. It was determined that this test point is neither bubbly flow or churn flow, because there are fairly large fluctuations in the signal but these fluctuations are large enough or defined well enough to be slug bubbles. This is an example of the transition region between bubbly flow and slug flow because from Figure 51the standard deviation is not as small as it had been for the previous examples of bubbly flow and the normalized impedance signal is neither similar to the previous bubbly flow or slug flow cases.

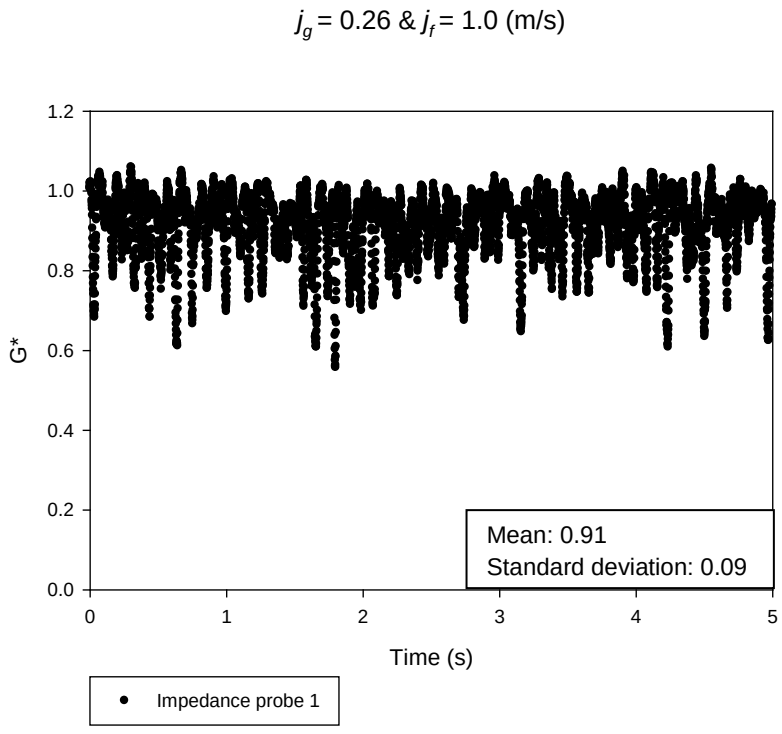

Figure 53: Example of the normalized impedance signal for the transition between bubbly flow and slug flow at *L/D* = 0 and j_f = 1.0 m/s.

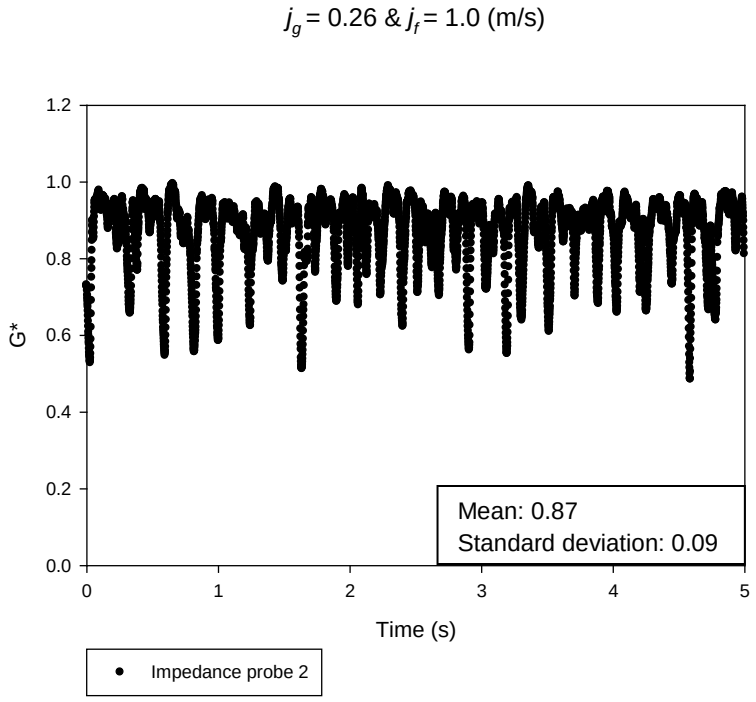

Figure 54: Example of the normalized impedance signal for the transition between bubbly flow and slug flow at *L/D* = 25 and j_f = 1.0 m/s.

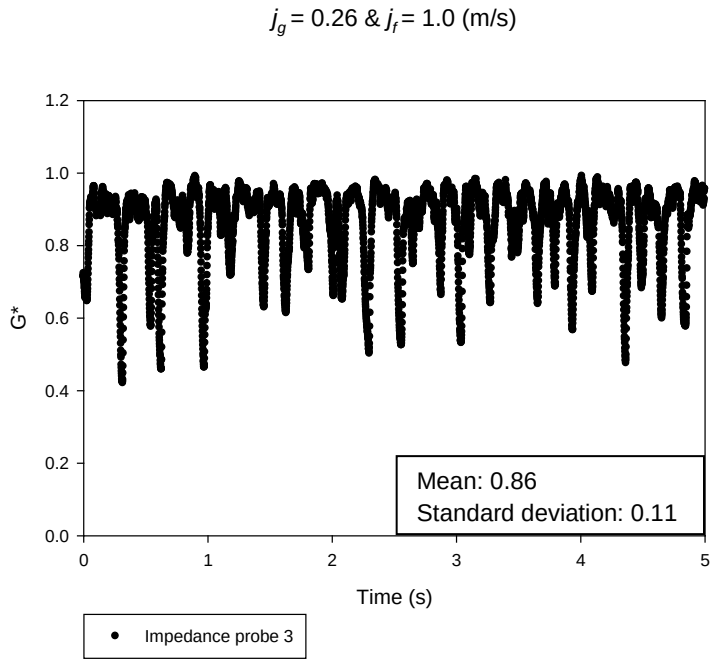

Figure 55: Example of the normalized impedance signal for the transition between bubbly flow and slug flow at *L/D* = 49 and j_f = 1.0 m/s.

The transition between slug and churn flow for j_f = 1.0 m/s is not well defined. The normalized impedance signals are found in Figures 56, 57, 58, 59, 60, and 61 for inlet j_g's = 0.52 and 1.14 m/s. The two test points that were chosen that do show some differences in their normalized impedance signals. These differences are not obvious so definite conclusions about the flow regime could not be reached. For the test points when j_g = 0.52 m/s and j_g = 1.14 m/s the normalized impedance signal has very large fluctuations that oscillate rapidly. This gives information that the flow is either in the churn or slug flow regimes but doesn't really distinguish between the two. The only difference is that for j_g = 1.14 m/s the oscillations seem to be a little more disorganized, but only slightly.

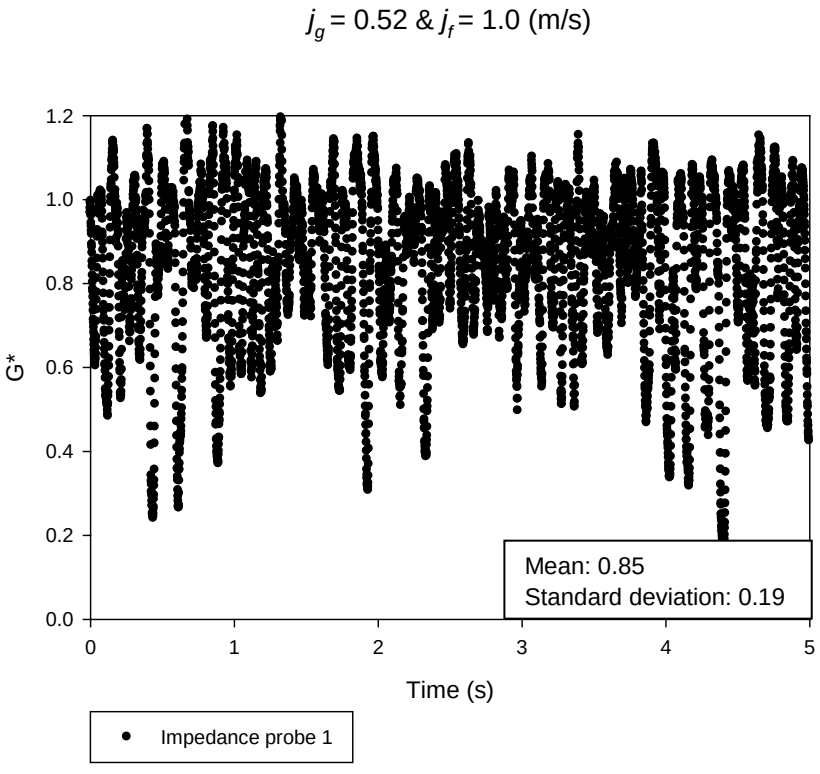

Figure 56: Example of a normalized impedance signal for slug or churn flow at *L/D* = 0 and j_f = 1.0 m/s.

j_g = 0.54 & j_f = 1.0 (m/s)

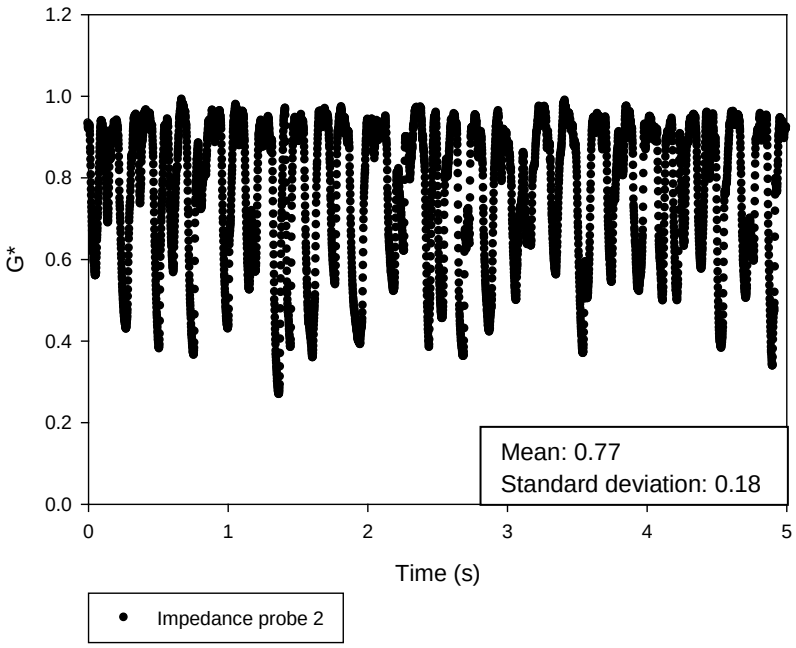

Figure 57: Example of a normalized impedance signal for slug or churn flow at *L/D* = 25 and j_f = 1.0 m/s.

j_g = 0.55 & j_f = 1.0 (m/s)

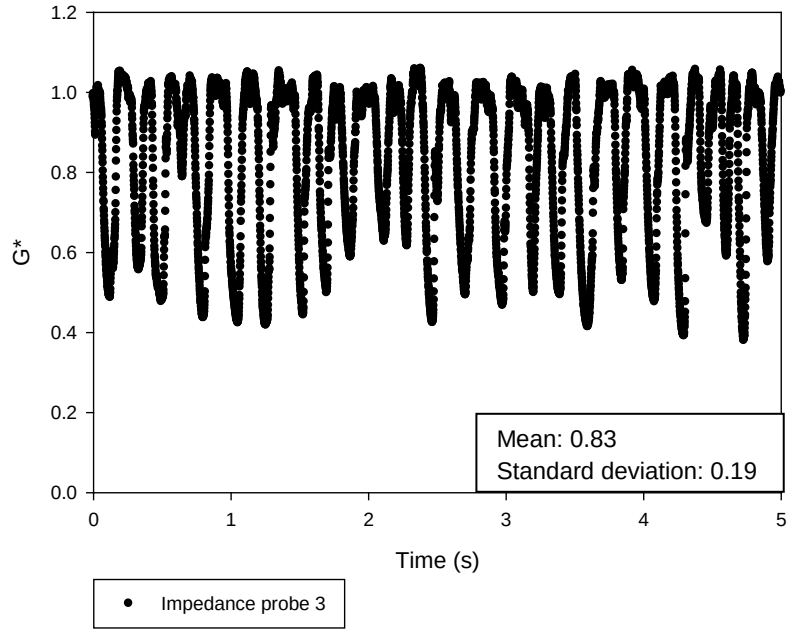

Figure 58: Example of a normalized impedance signal for slug or churn flow at *L/D* = 49 and j_f = 1.0 m/s.

j_g = 1.14 & j_f = 1.0 (m/s)

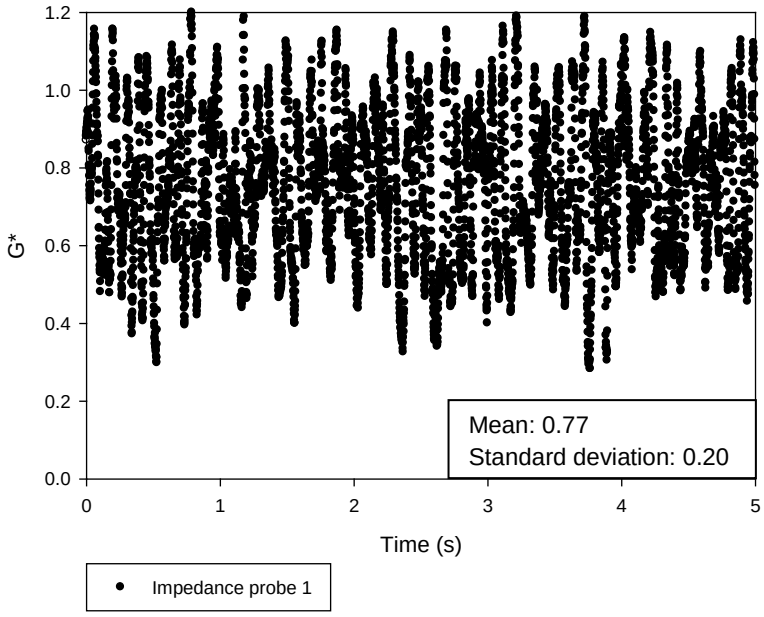

Figure 59: Example of a normalized impedance signal for churn flow at *L/D* = 0 and j_f = 1.0 m/s.

j_g = 1.18 & j_f = 1.0 (m/s)

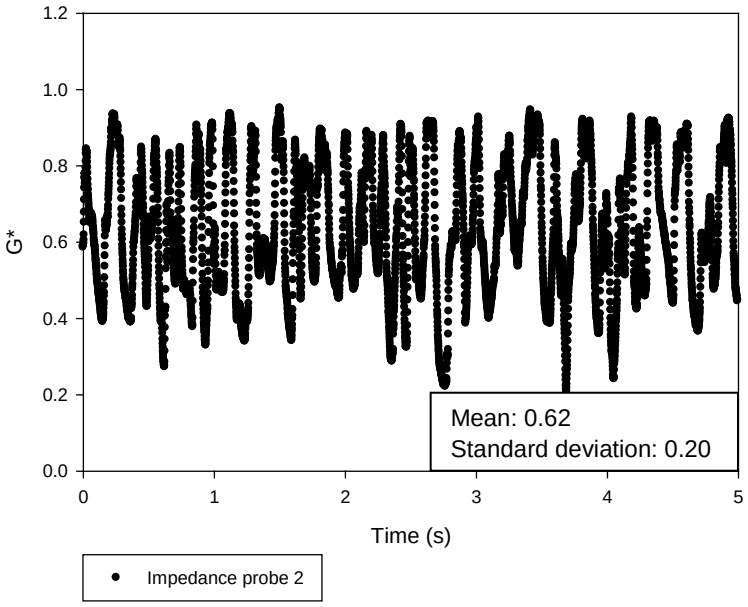

Figure 60: Example of a normalized impedance signal for churn flow at *L/D* = 25 and j_f = 1.0 m/s.

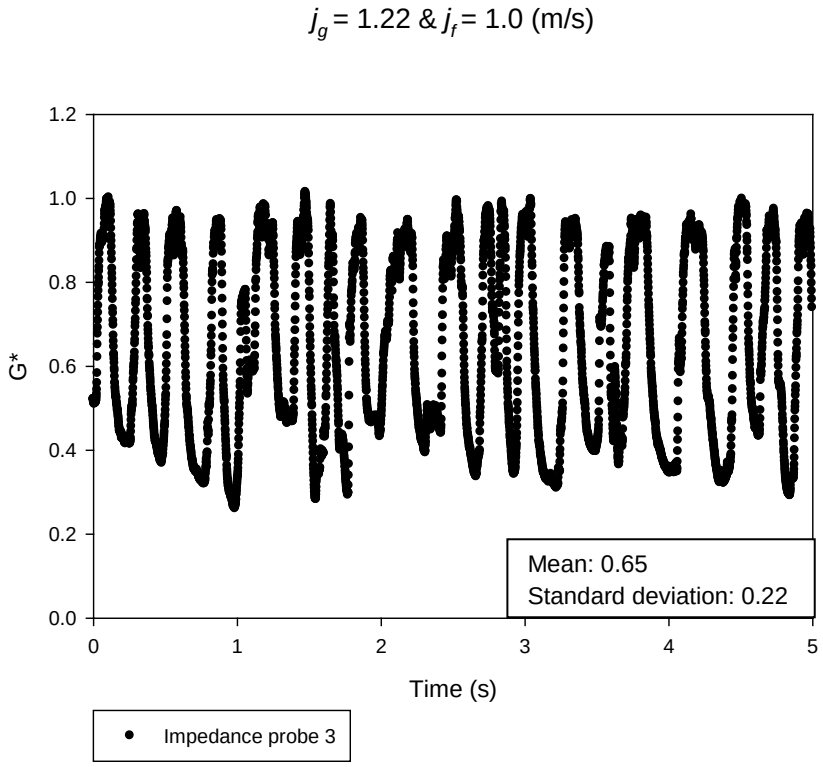

Figure 61: Example of a normalized impedance signal for churn flow at *L/D* = 49 and j_f = 1.0 m/s.

For the test points when j_f = 1.0 m/s bubbly and slug flow regimes were not observed. At the lowest j_g a transition between bubbly and slug flow was observed. When j_g = 0.52 m/s slug flow could not be differentiated from the example of churn flow. The reason for this is that for this test point the oscillations did seem to be more organized than the churn flow examples found for all three j_f 's tested, but the oscillations were not as well defined as the slug flow cases for j_f = 0.25 and 0.5 m/s. Churn flow was determined to exists at the inlet j_g = 1.14 m/s, because large and rapid oscillations existed and were not well organized as the slug flow cases for j_f = 0.25 and 0.5 m/s.

Chapter 4: Future Work and Conclusion

The modifications performed on the test facility were a new air-water separator was installed and the inlet water lines to the bubble injector changed to allow for the independent control and monitoring of the auxiliary water flow into the bubble injector. The important instrumentation that was built and install were the impedance void meters and the four-sensor conductivity probe. This instrumentation was test and it was found that for tests the difference between bubbly flow, slug flow and churn flow could be determined when j_f = 0.25 and 0.5 m/s. For j_f = 0.5 m/s it was found that the four-sensor conductivity probe could differentiate between the bubbly flow regime and slug flow regime, but the conductivity probe could not differentiate between the slug flow regime and the churn flow regime. For j_f = 1.0 m/s churn flow could be differentiate from the transition between bubbly flow and slug flow, however slug flow could not be determined from the current set of tests. The future work for this research will be to construct a neural network to help objectively identify the correlation between impedance fluctuations and flow regimes. A new sparger with a larger average pore size needs to be installed and preliminary tests need to be performed to determine the range of inlet bubble sizes that can be produced. The test matrix for determining the tests that need to be performed to identify the correlation between inlet bubble sizes to the downstream flow regime transitions. The test identified in the test matrix need to be performed.

References

Fu, X. Y., & Ishii, M. (1999). *User's guide for 4pt100 advanced four-point probe signal processor.* Purdue University.

Ishii, M. (1977). *One-dimensional drift-flux model and constitutive equations for relative motion between phases in various two-phase flow regimes.* Argonne National Laboratory.

Ishii, M., & Zuber, Z. (1979). Drag coefficient and relative velocity in bubbly, droplet or particulate flows. *AICHE Journal* , 843.

Kim, S., Fu, X., Wang, X., & Ishii, M. (2000). Development of the miniaturized four-sensor conductivity probe and the signal processing scheme. *International Journal of Heat and Mass Transfer* , 4101-4118.

Mi, Y. (1999). *Two-phase flow characterization based on advanced instrumentation, neural networks, and mathematical modeling.* Ann Arbor: UMI.

Mi, Y., Ishii, M., & Tsoukalas, L. (2001). Flow regime identification methodology with neural networks and two-phase flow models. *Nuclear Engineering and Design* , 87-100.

Mishima, K., & Ishii, M. (1983). Flow Regime Transition Criteria for Upward Two-Phase Flow in Vertical Tubes. *International Journal of Heat and Mass Transfer* , 723-737.

Sun, X. (2010). Lecture notes. *NE 737.*

Taitel, T., Bornea, D., & Dukler, A. E. (1980). Modeling Flow Pattern Transitions for Steady Upward Gas-Liquid Flow in Vertical Tubes,. *AICHE Journal* , 345-354.

Todreas, N. E., & Kazimi, M. S. (1993). *Nuclear Systems I Thermal Hydraulics Fundamentals.* Taylor & Francis .

Appendix

This appendix gives that normalized impedance signals and four-sensor conductivity probe data for the other test points that were not presented in the data section.

j_g=0.42 (m/s) & j_f=0.26 (m/s)

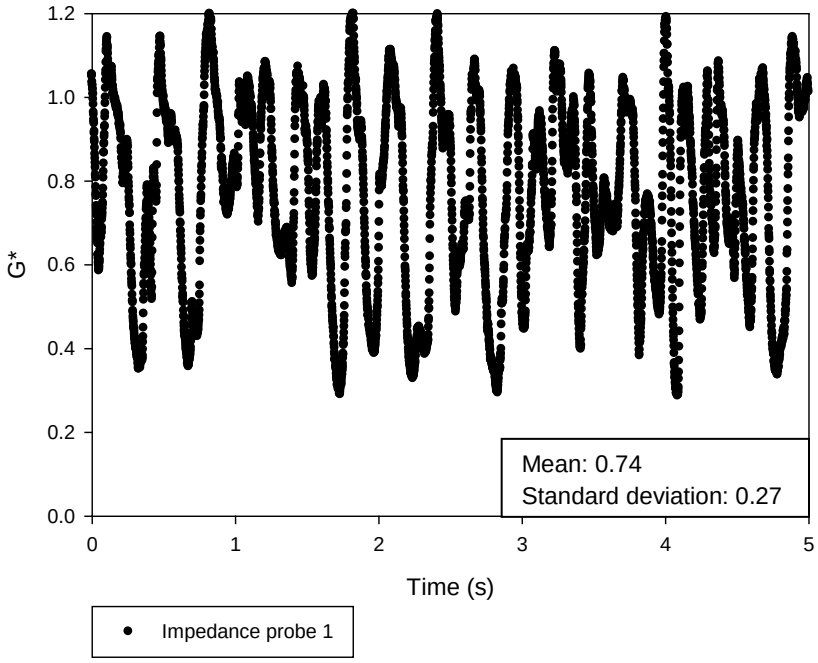

j_g=0.43 (m/s) & j_f=0.26 (m/s)

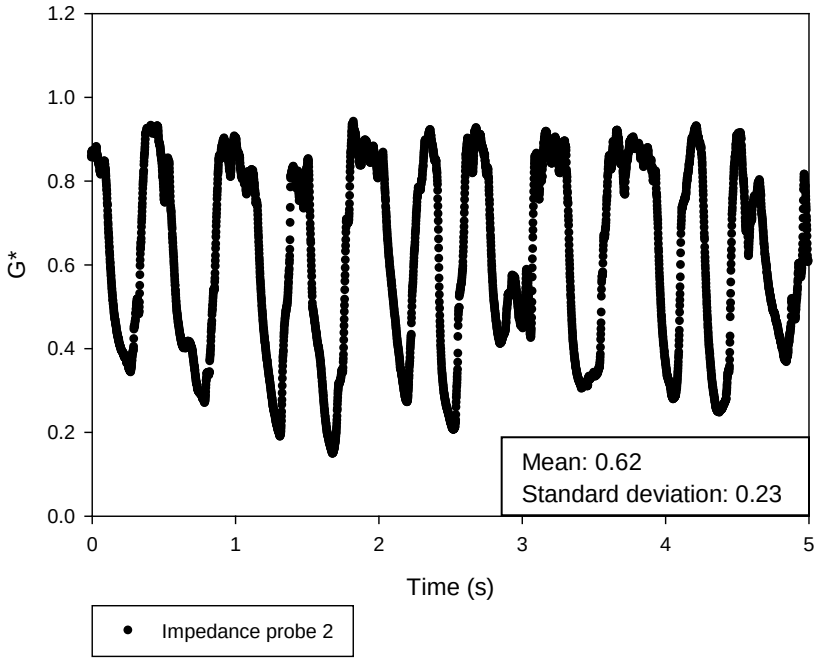

j_g=0.45 (m/s) & j_f=0.26 (m/s)

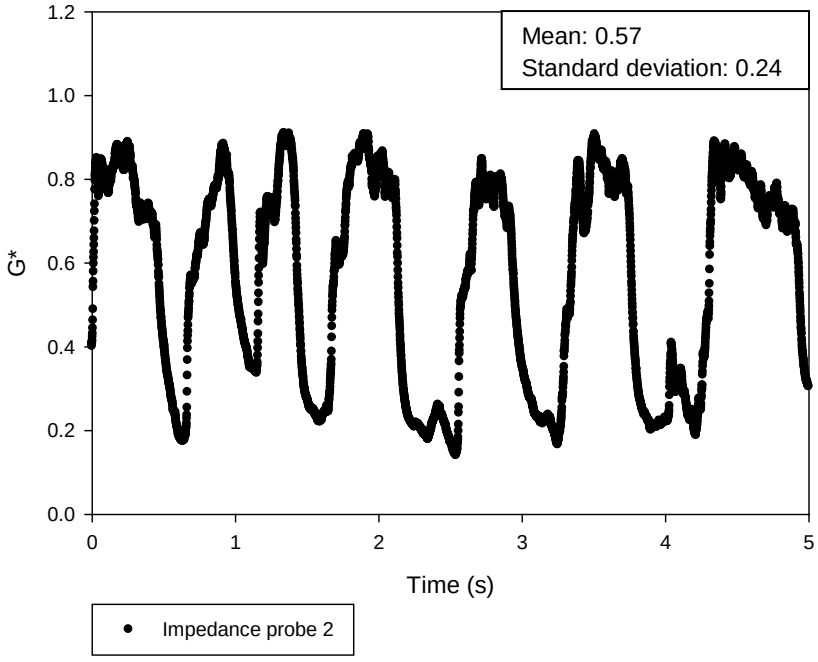

j_g=0.78 (m/s) & j_f=0.25 (m/s)

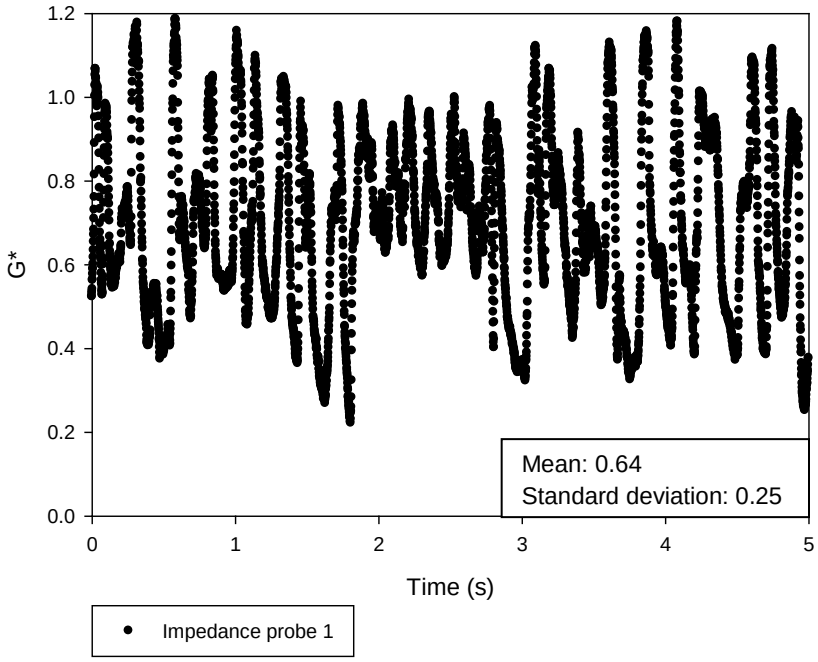

j_g=0.82 (m/s) & j_f=0.25 (m/s)

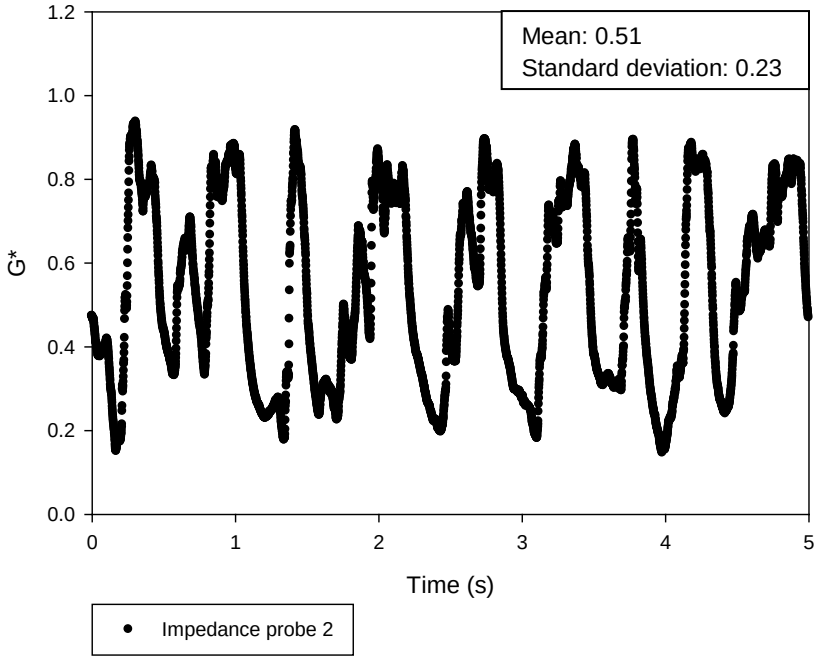

j_g=0.87 (m/s) & j_f=0.25 (m/s)

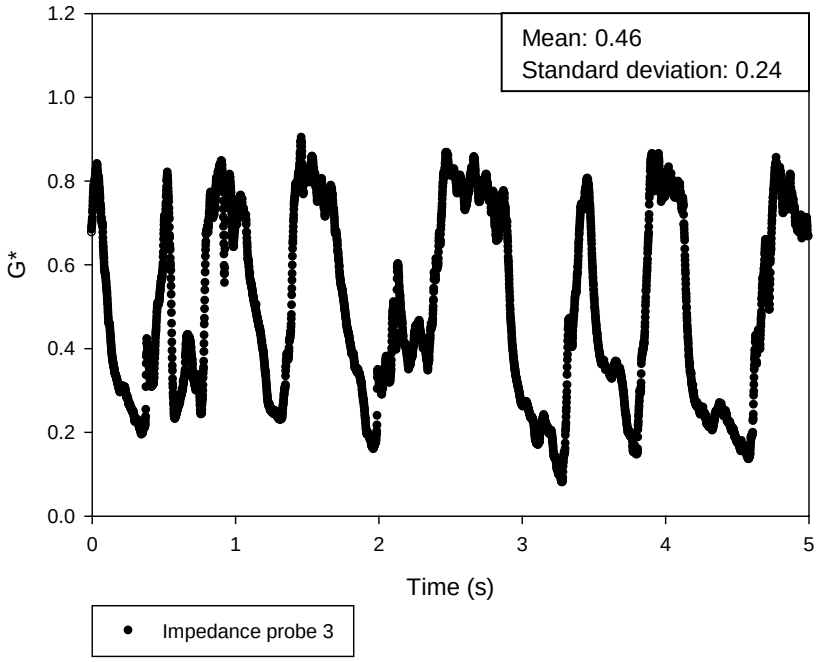

j_g=1.02 (m/s) & j_f=0.25 (m/s)

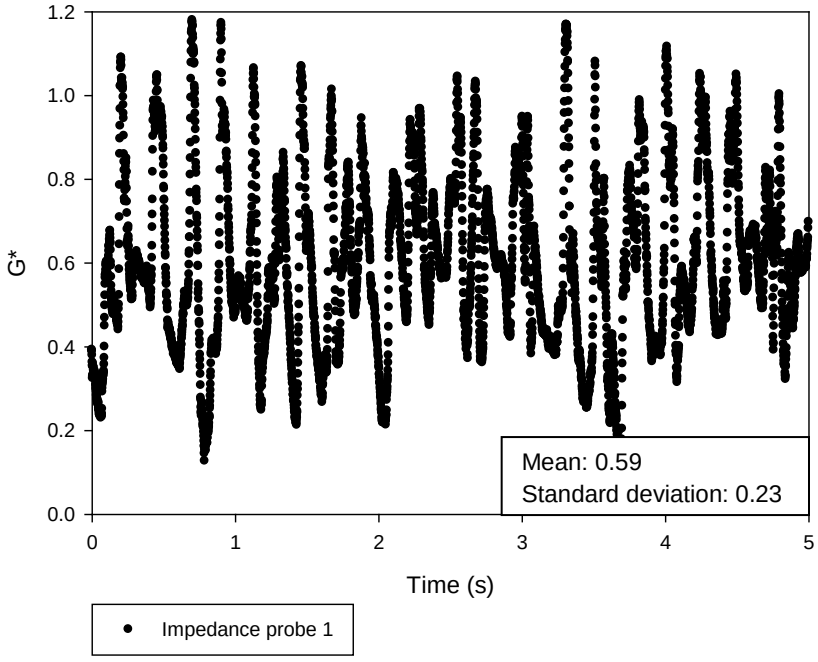

j_g=1.08 (m/s) & j_f=0.25 (m/s)

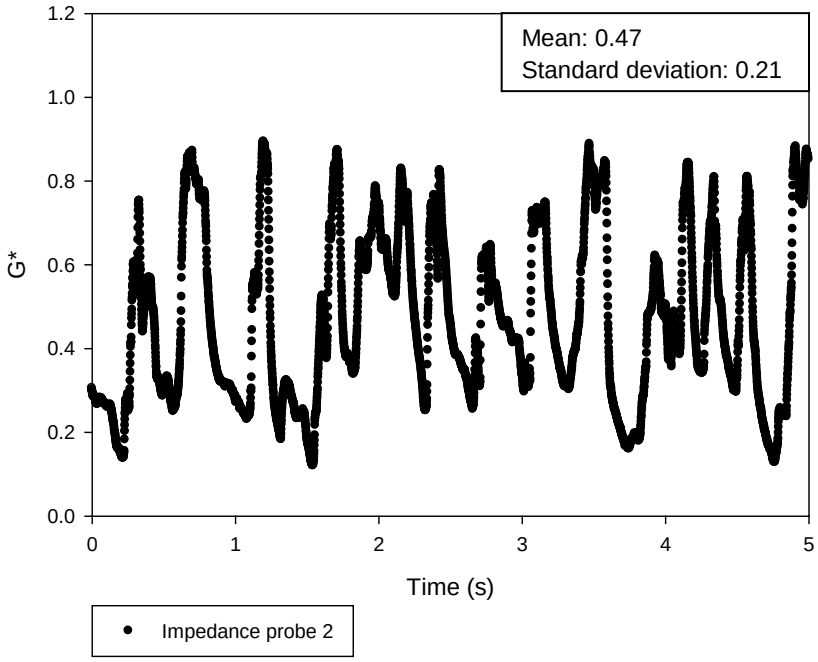

j_g=1.15 (m/s) & j_f=0.25 (m/s)

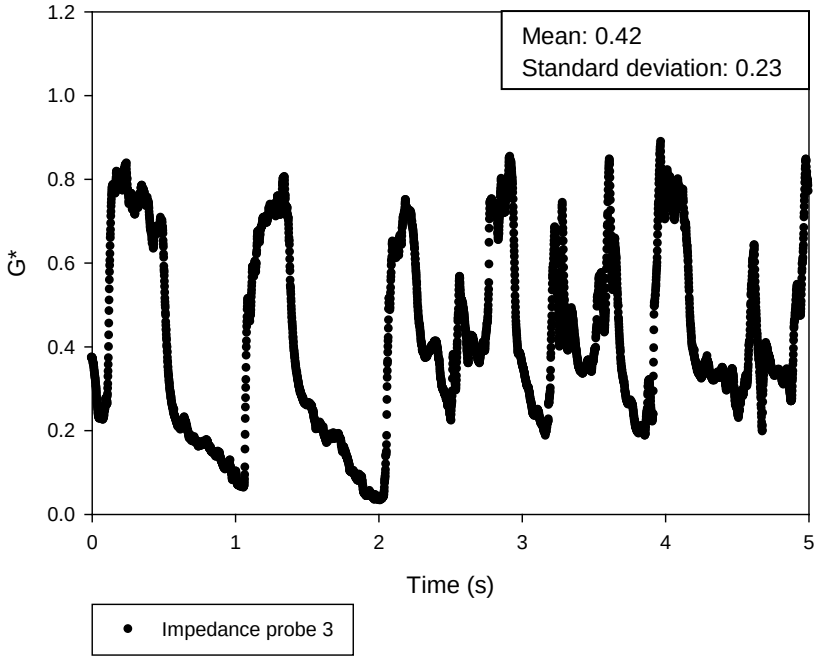

j_g=0.41 (m/s) & j_f=0.5 (m/s)

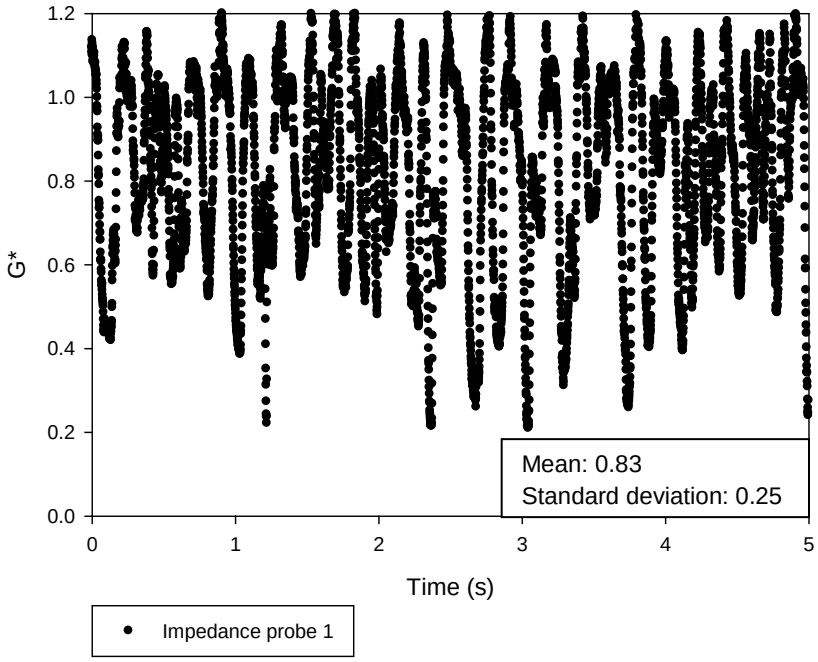

j_g=0.42 (m/s) & j_f=0.5 (m/s)

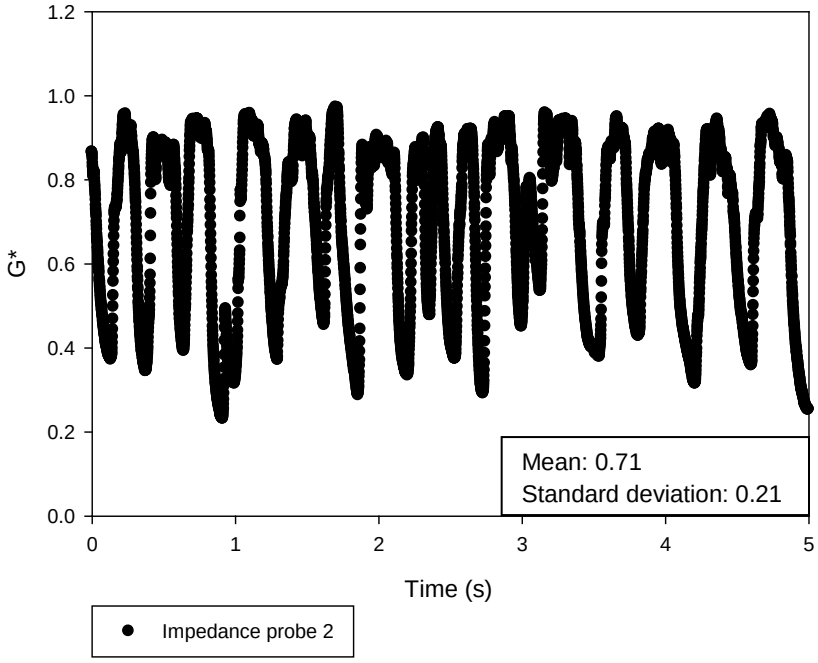

j_g=0.44 (m/s) & j_f=0.5 (m/s)

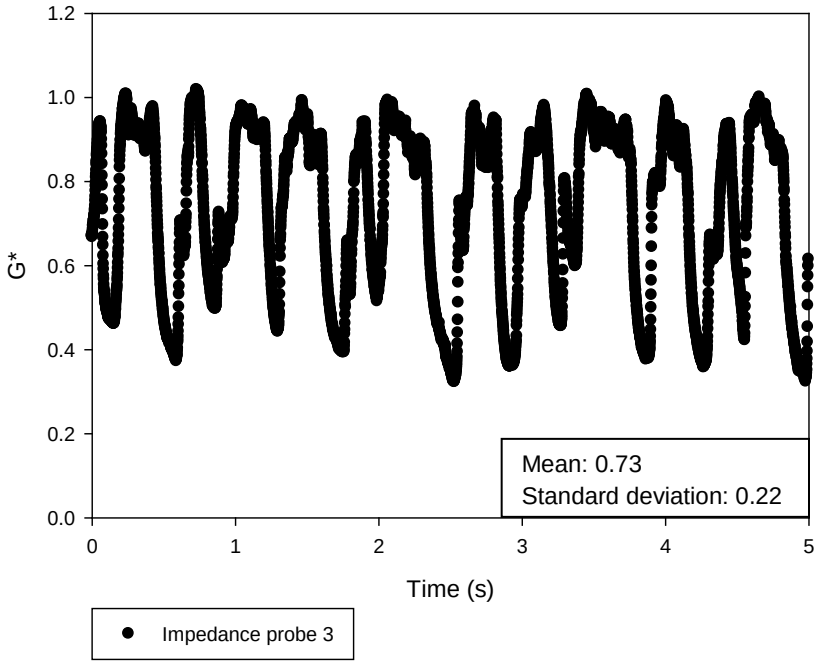

j_g=0.41 (m/s) & j_f=0.5 (m/s)

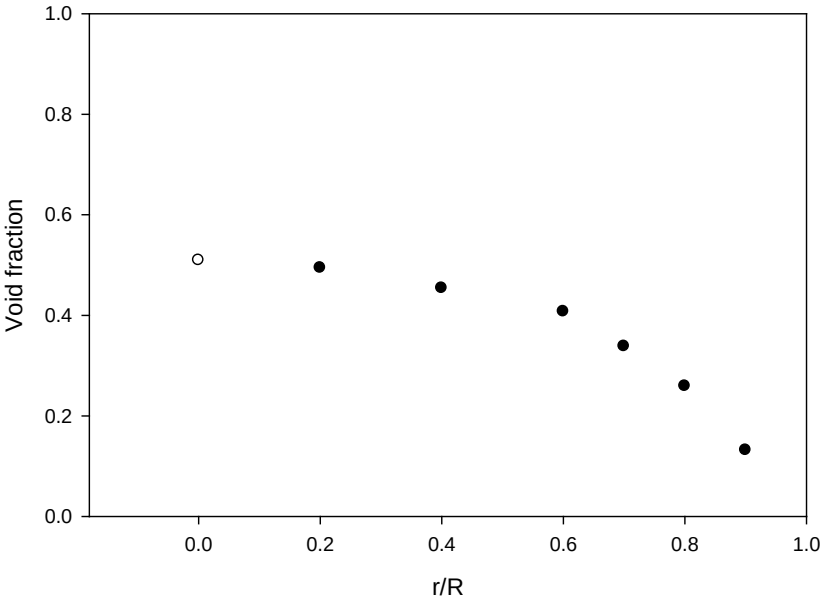

j_g=0.41 (m/s) & j_f=0.5 (m/s)

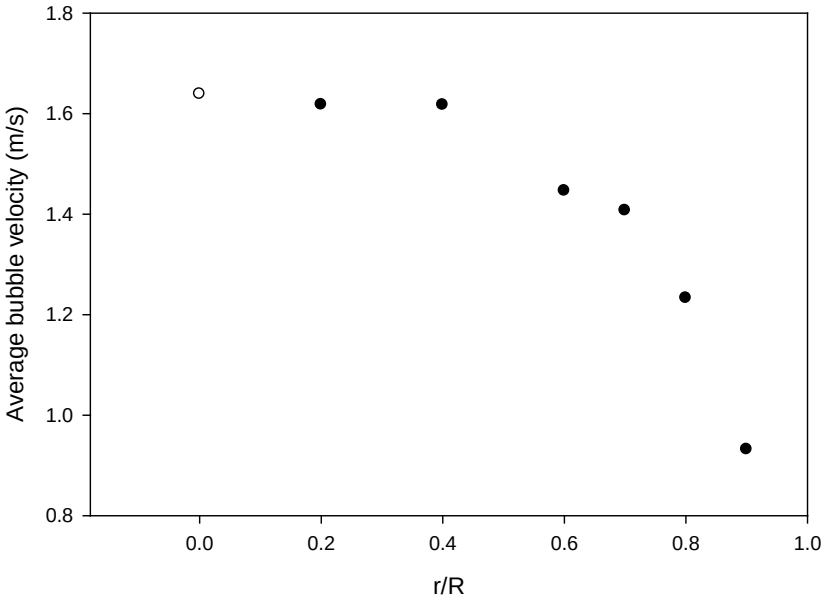

j_g=0.41 (m/s) & j_f=0.5 (m/s)

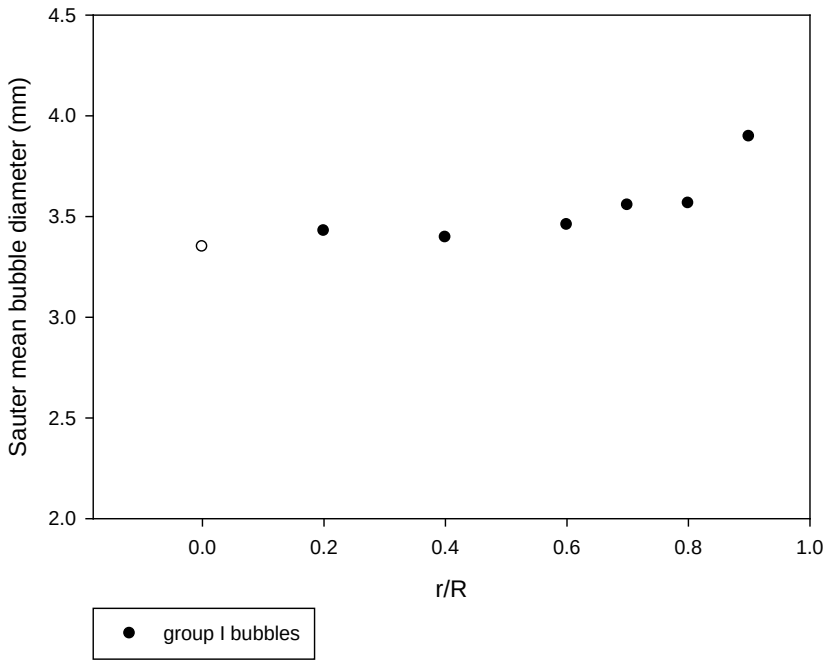

j_g=0.41 (m/s) 7 j_f=0.5 (m/s)

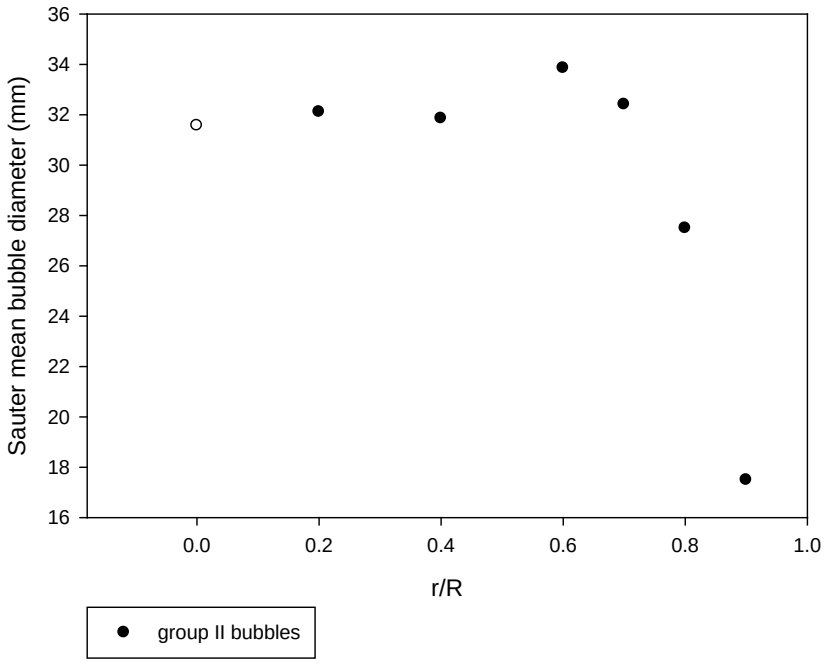

j_g=0.82 (m/s) & j_f=0.5 (m/s)

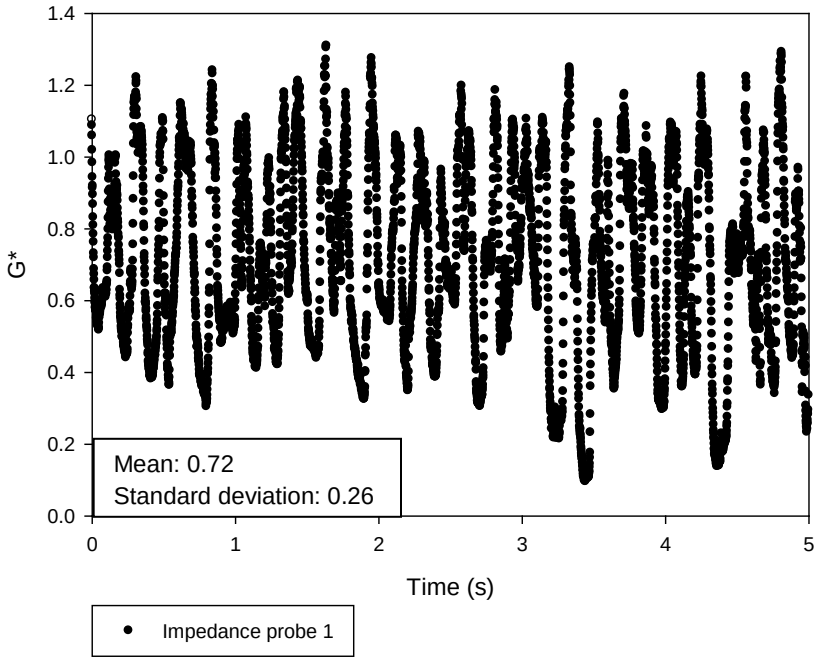

j_g=0.86 (m/s) & j_f=0.5 (m/s)

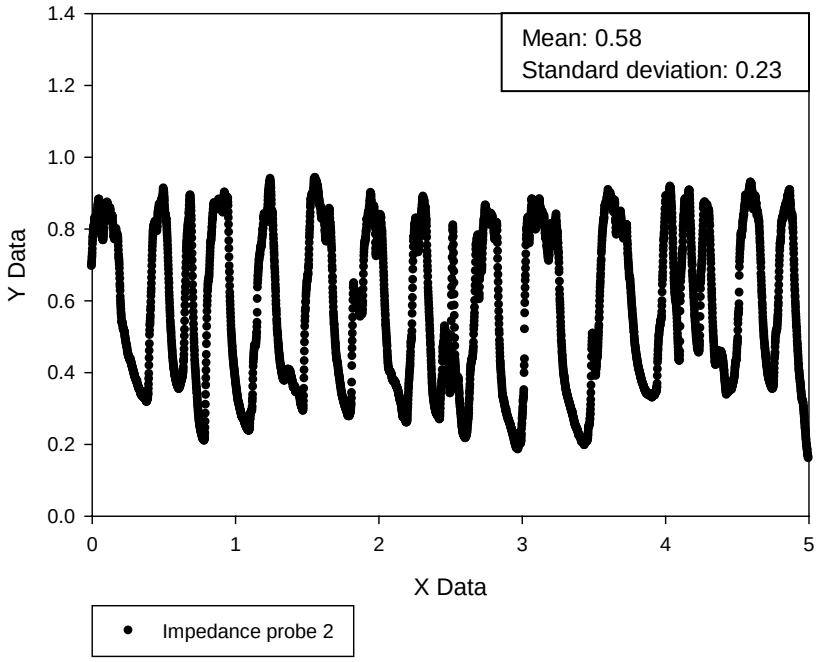

j_g=0.90 (m/s) & j_f=0.5 (m/s)

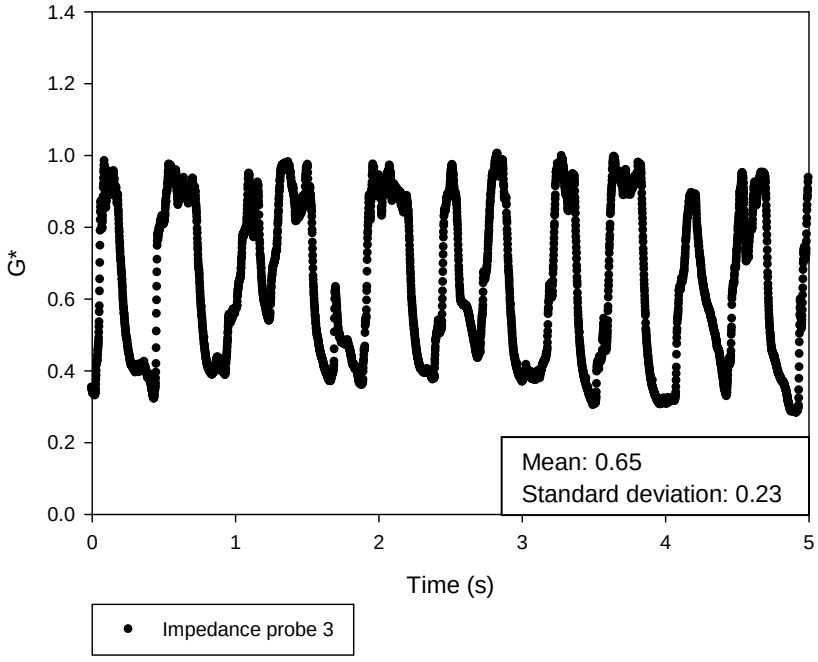

j_g=0.82 (m/s) & j_f=0.5 (m/s)

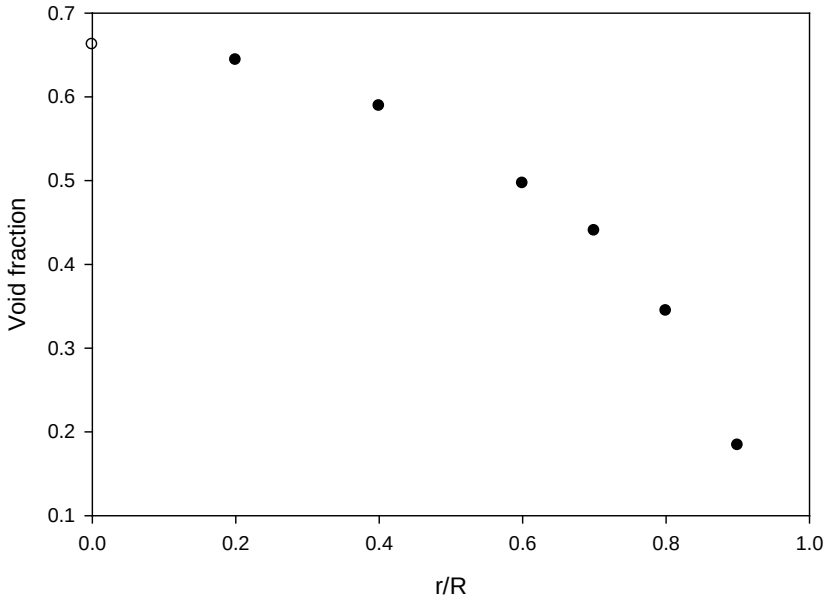

j_g=0.82 (m/s) & j_f=0.5 (m/s)

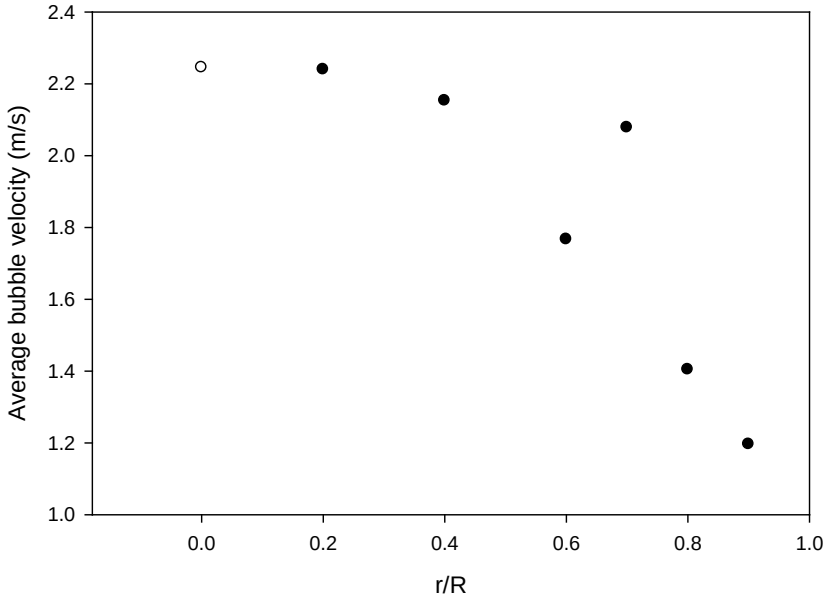

j_g=0.82 (m/s) & j_f=0.5 (m/s)

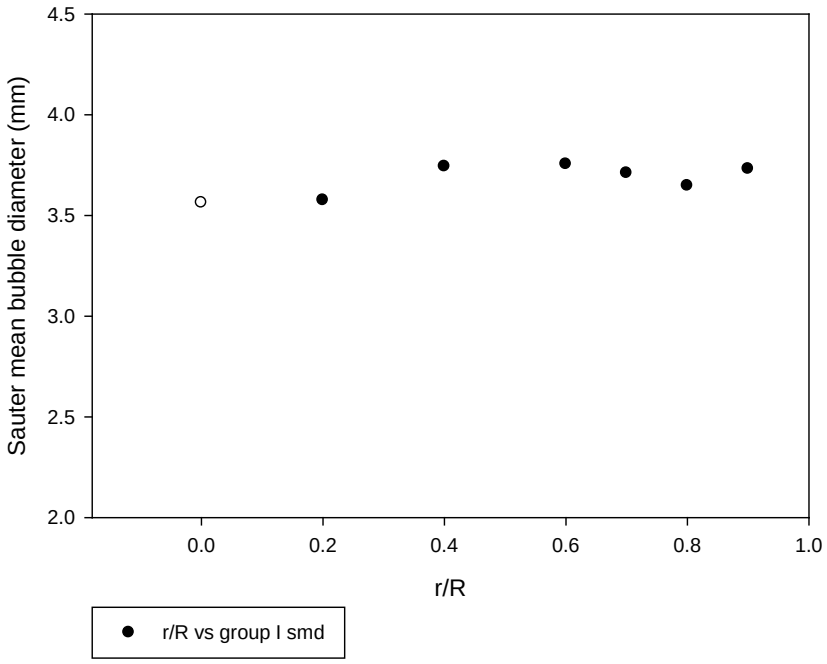

j_g=0.82 (m/s) & j_f=0.5 (m/s)

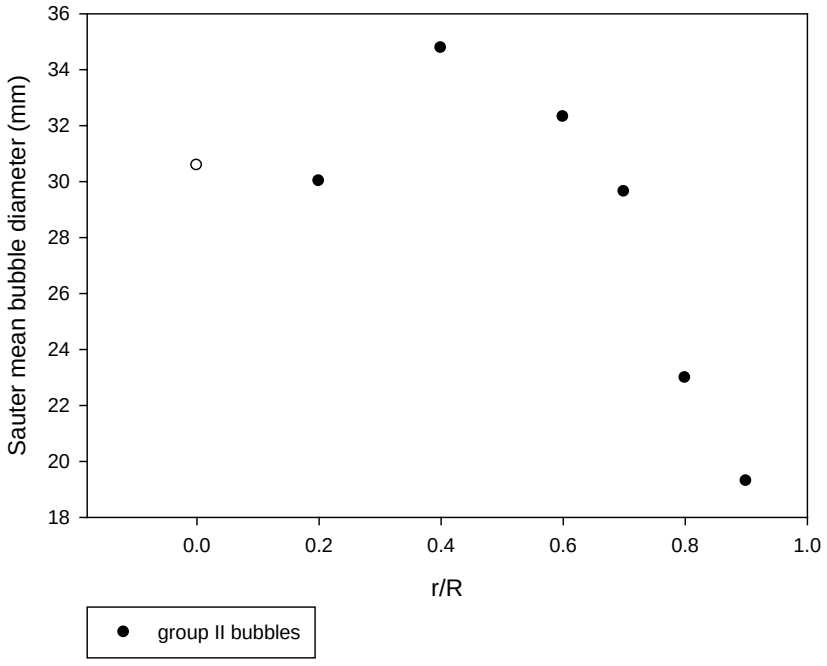

j_g=1.09 (m/s) & j_f=0.5 (m/s)

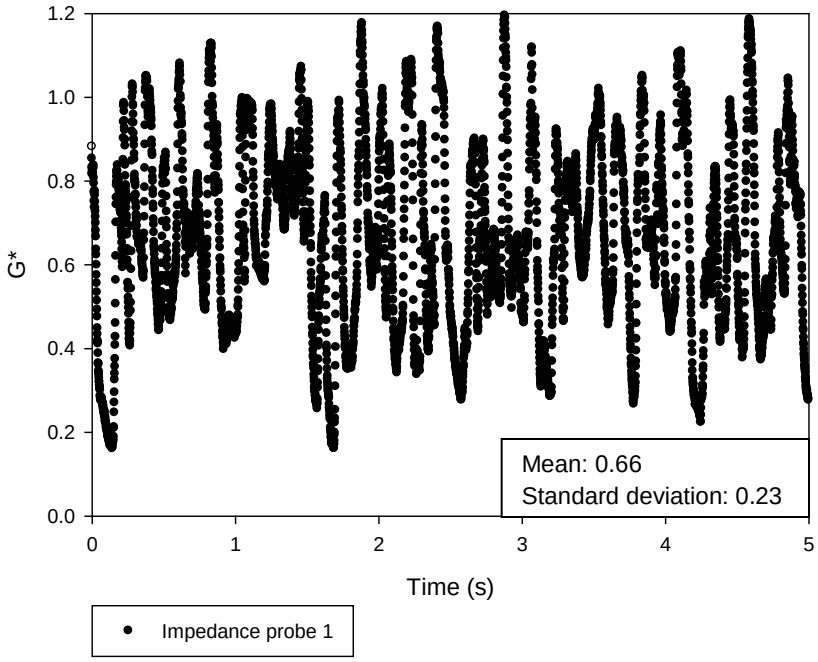

j_g=1.14 (m/s) & j_f=0.5 (m/s)

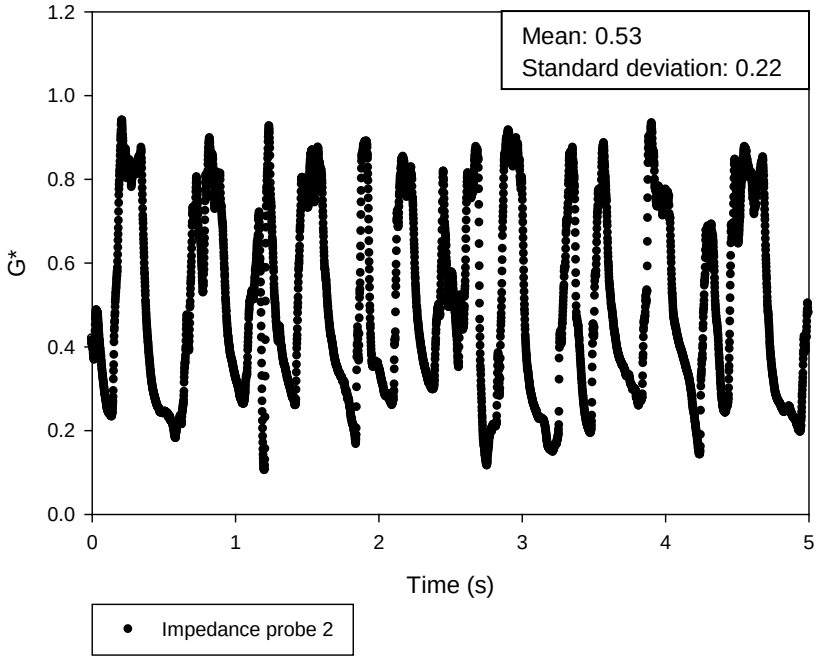

j_g=1.20 (m/s) & j_f=0.5 (m/s)

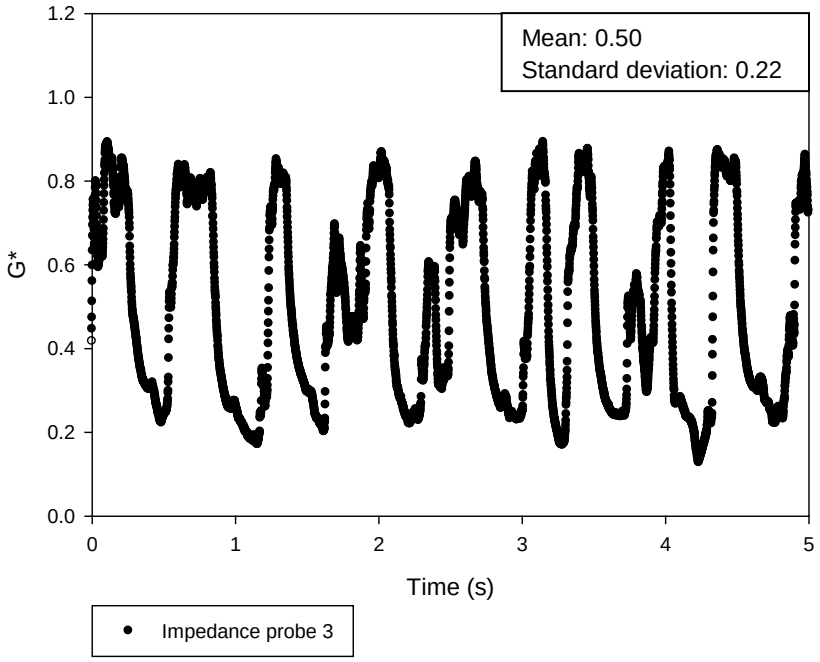

j_g=1.09 (m/s) & j_f=0.5 (m/s)

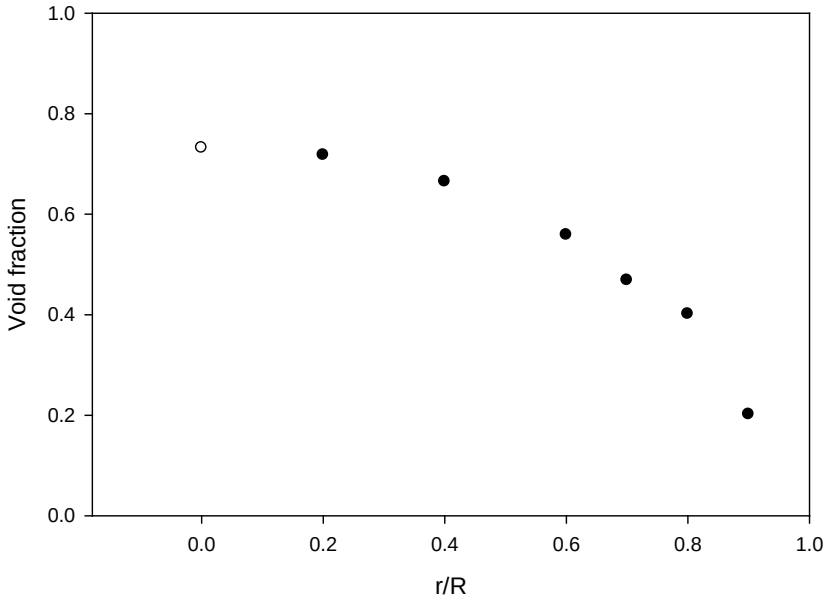

j_g=1.09 (m/s) & j_f=0.5 (m/s)

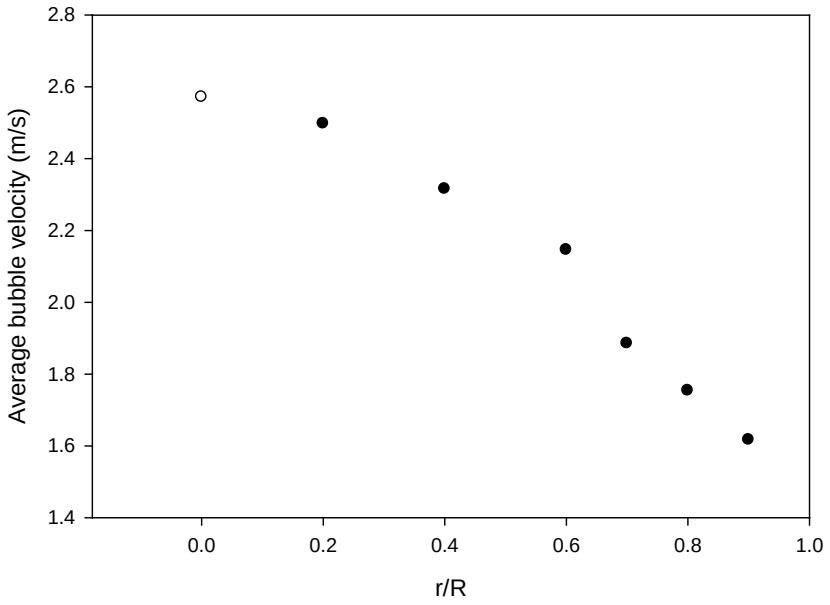

j_g=1.09 (m/s) & j_f=0.5 (m/s)

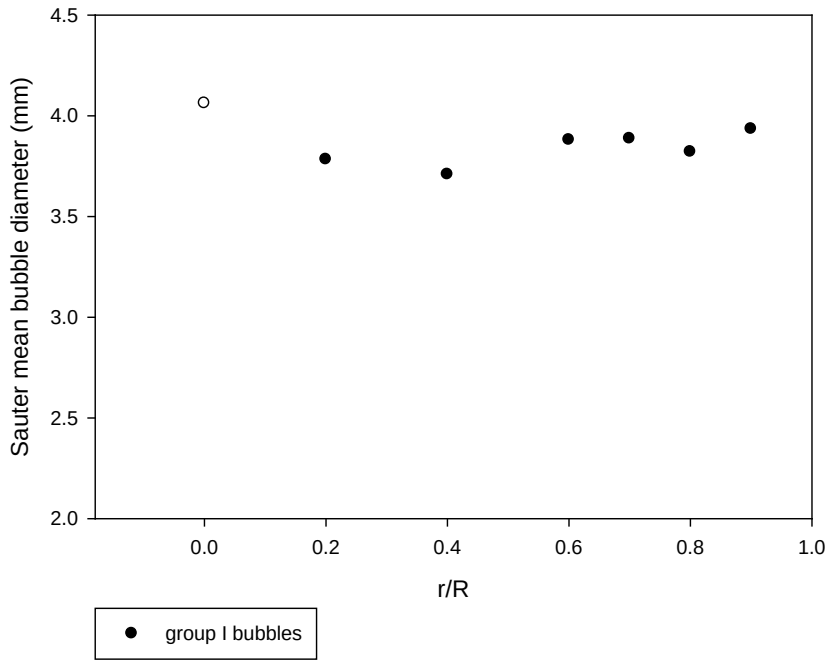

j_g=1.09 (m/s) & j_f=0.5 (m/s)

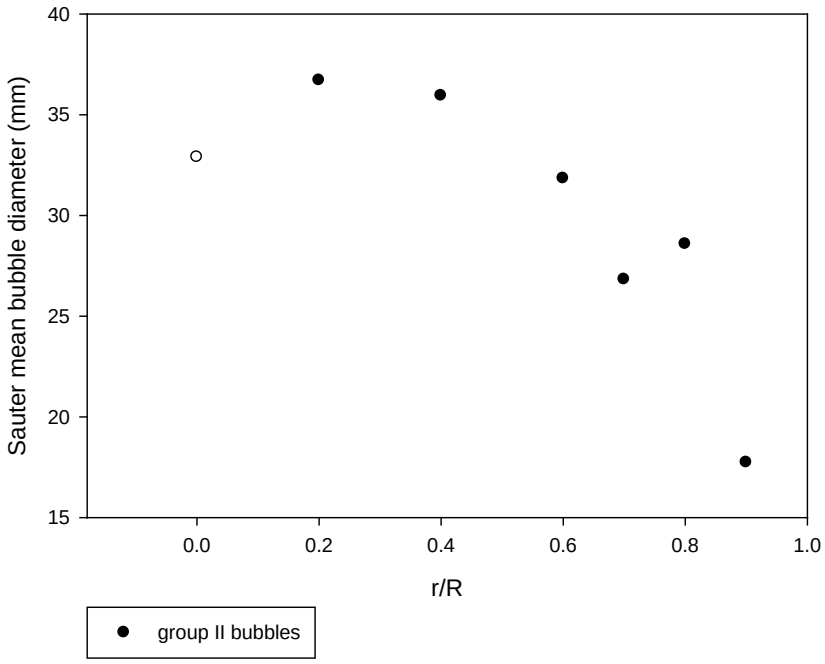

j_g=0.39 (m/s) & j_f=1.0 (m/s)

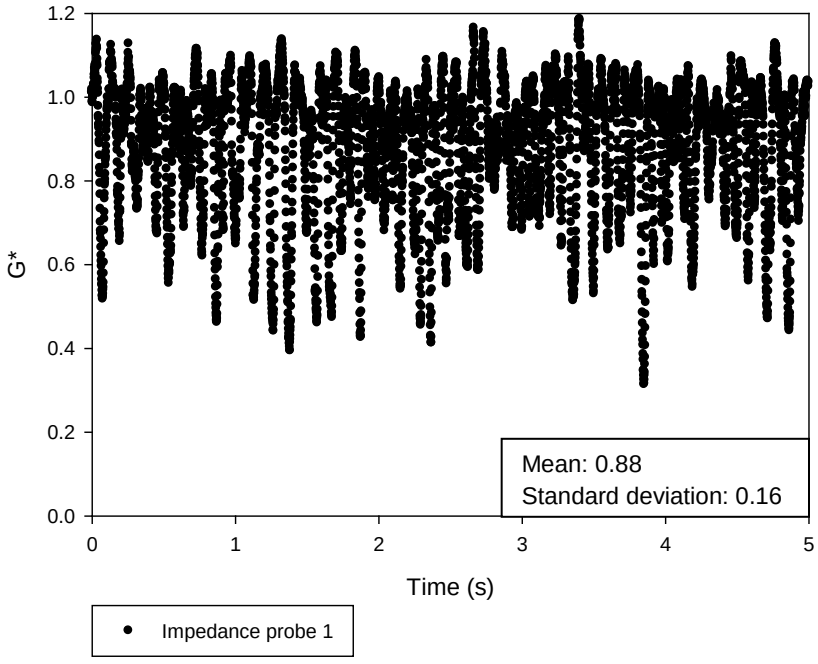

j_g=0.40 (m/s) & j_f=1.0 (m/s)

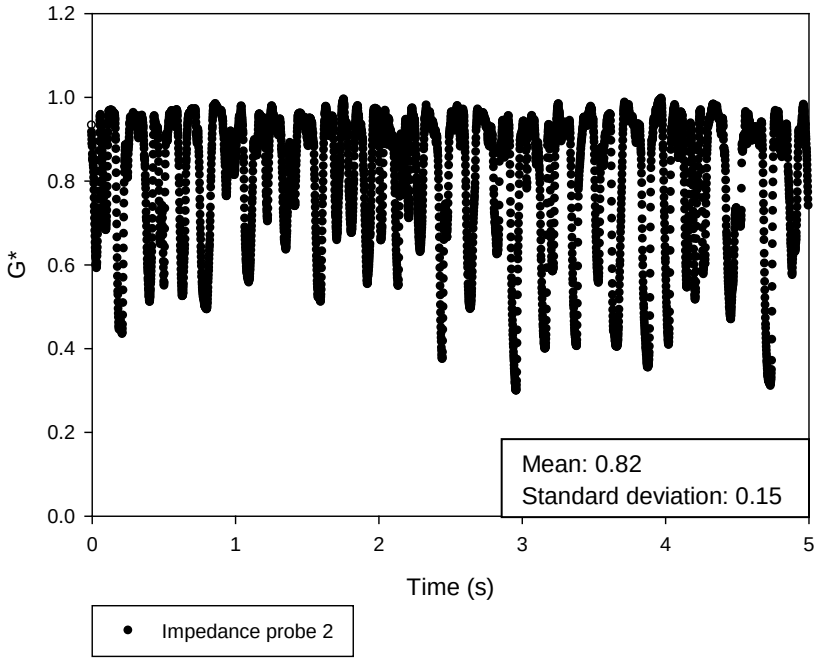

j_g=0.40 (m/s) & j_f=1.0 (m/s)

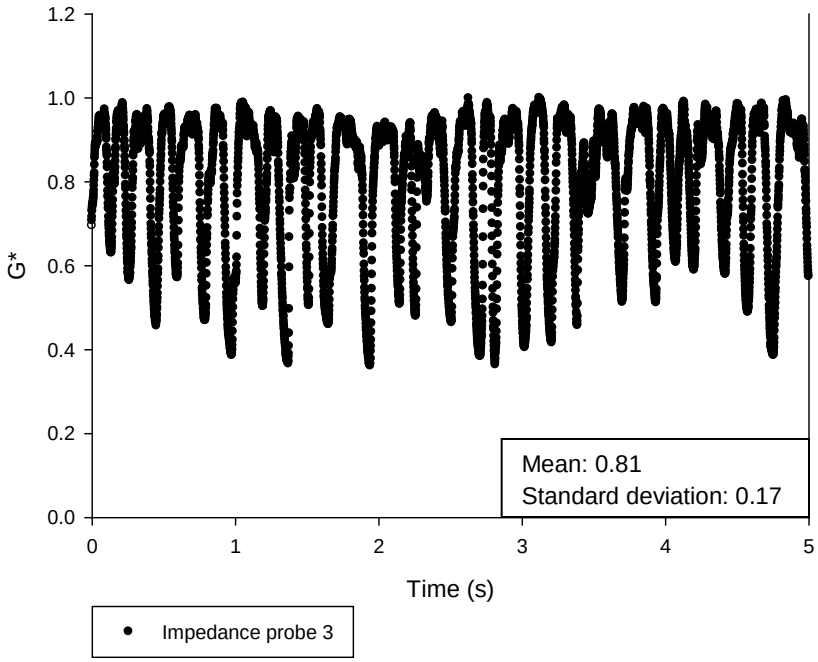

j_g=0.66 (m/s) & j_f=1.0 (m/s)

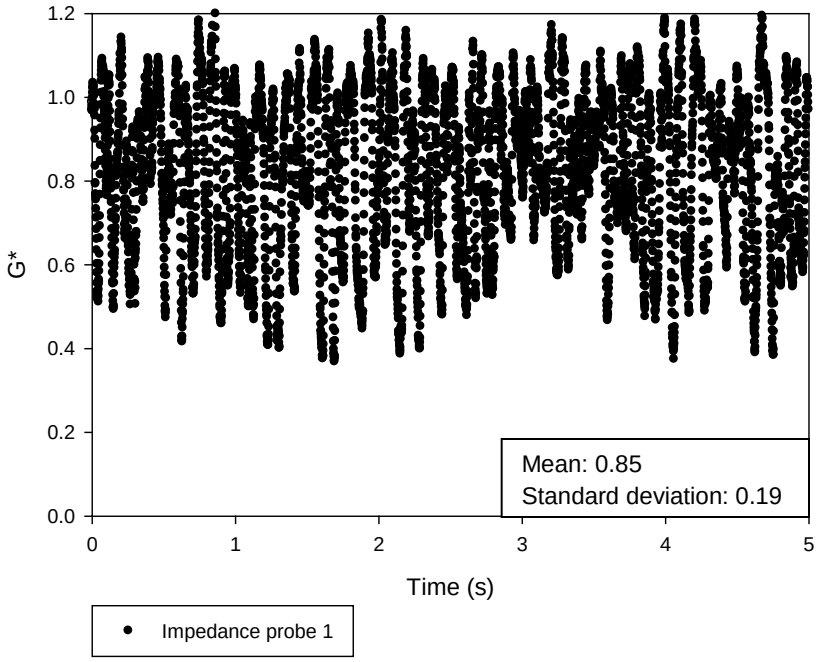

j_g=0.68 (m/s) & j_f=1.0 (m/s)

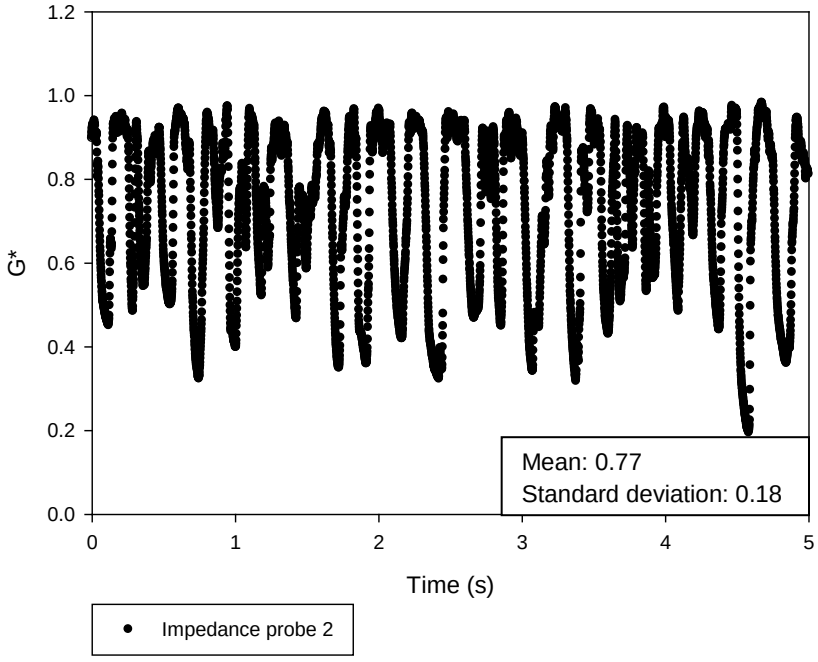

j_g=0.70 (m/s) & j_f=1.0 (m/s)

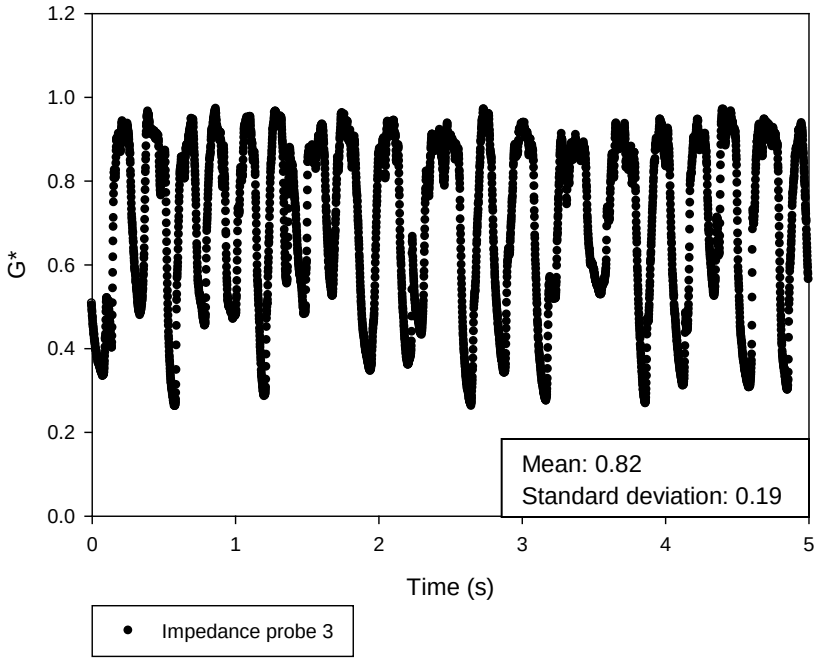

j_g=0.81 (m/s) & j_f=1.0 (m/s)

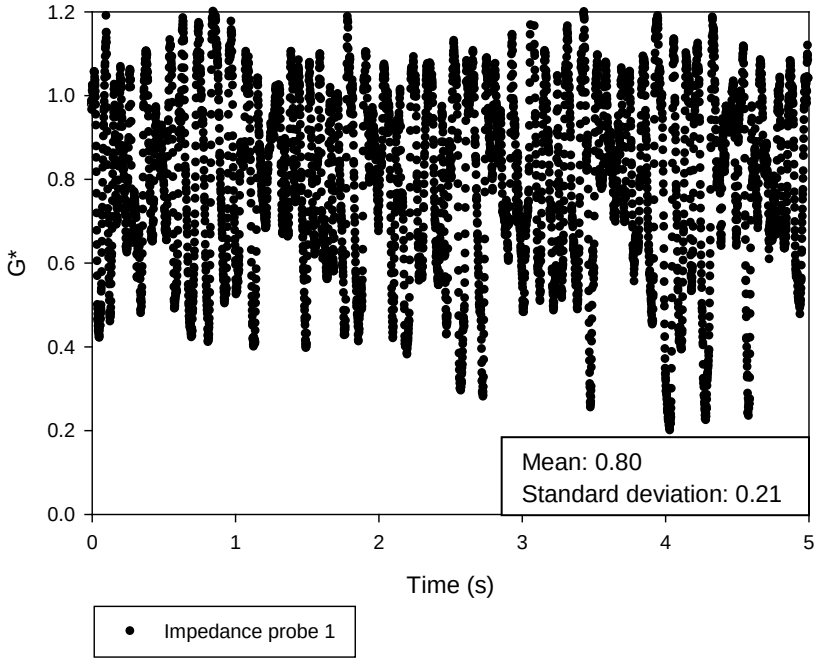

j_g=0.83 (m/s) & j_f=1.0 (m/s)

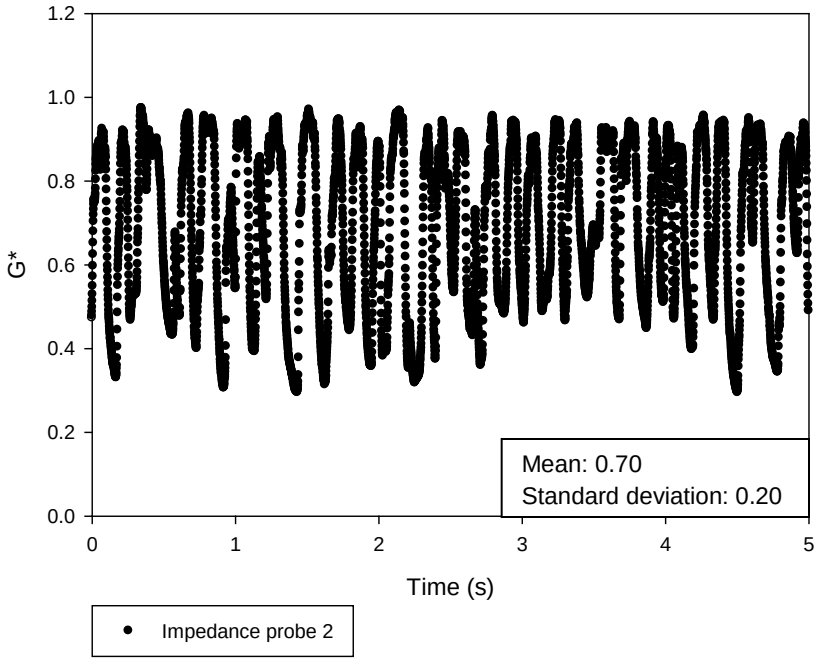

j_g=0.86 (m/s) & j_f=1.0 (m/s)